FEASIBILITY STUDY OF A FIBER BRAGG GRATING BASED ACCELEROMETER

FINAL REPORT

DREV TASK NO:
16/3-1993 (PRRN:33518)

PROJECT OFFICER:
Dr. Gédéon Drouin, DREV

TASK SCIENTIST:
Dr. K.O. Hill, CRC

February 28, 1999

105-01821/

FEASIBILITY STUDY OF A FIBER BRAGG GRATING BASED ACCELEROMETER

FINAL REPORT

BY

K. O. Hill, F. Bilodeau, S. Thériault,
J. Albert, B. Malo and D. C. Johnson

DREV TASK NO:
16/3-1993 (PRRN: 33518)

PROJECT OFFICERS:
Dr. Alain Béliveau, DREV
Dr. Gédéon Drouin, DREV

TASK SCIENTIST:
Dr. K. O. Hill, CRC

February 28, 1999

Defence Research and Development Canada
Recherche et développement pour la défense Canada
Canada

Français Contact Us Help Search Canada Site
Home Defence R&D Canada Defence Site

Browse Indexes
Titles
Authors
Descriptors
Corporate Authors
Corporate Acronyms
Report Numbers

Search Database
Summary

It is recommended you search "Authors" and "Corporate Authors" on their respective "Browse" pages.

Click here if you are having problems displaying text (ie. text is too big, or too small) or page appears to be jumbled.

Prior Top **Document:** 1 of 1 Bottom Next Order Click here to Order Click here to Download

TITLE:(U) FEASIBILITY STUDY OF A FIBER BRAGG GRATING BASED ACCELEROMETER
PERSONAL AUTHOR: Hill, K.O.; Bilodeau, F.; Theriault, S.; Albert, J.; Malo, B.; Johnson, D.C.
CORPORATE AUTHOR: Defence Research Establishment Valcartier, Valcartier QUE (CAN);Communications Research Centre, Ottawa ONT (CAN)

ABSTRACT: (U) This report describes the feasibility study of a Fiber Bragg Grating (FBG) based accelerometer. FBGs are periodic modulation of the refractive index of the core in an optical fiber. This periodic modulation creates an optical narrowband reflection filter which can be used in a variety of applications in telecommunications and in sensing. The first FBG was observed at the Communications Research Centre (CRC) by K.O. Hill in 1978. FBGs became a hot research topic in 1989 when side writing through the cladding was first demonstrated at United Technologies Corporation. What mae FBGs practical devices was the phase mask writing technique developed at CRC in 1992. Now FBGs are manufactured in large quantities throughout the world. This project is the first study of FBGs as accelerometers. FBGs have been studied for strain, temperature and hydrostatic pressure sensing because they have unique advantages over classical electrical systems. These advantages are electromagnetic interference immunity, light weight and small size, high temperature and radiation tolerance, flexibility, stability and durability against harsh environments. Also they have the advantage of being absolute, linear in response and of very low insertion loss so that they can be multiplexes in series for distributed sensing along a single monomode fiber. TRUNCATED
DESCRIPTORS: (U) Accelerometers;Fiber optics;Optical equipment;Detectors;Measuring instruments;Strain measuring instruments;Bragg cells;Optical processing

REPORT NUMBER: DREV-CR-1999-047; Contract Report
REPORT DATE: 28 Feb 1999
NUMBER OF PAGES : 148
DRDKIM N°: 99-00862
CANDIS N°: 510731
Format(s): Hardcopy;Document Image stored on Optical Disk

Contents

Contents i

List of Figures iv

List of Tables viii

Introduction 1

1 Design and modeling 3

- 1.1 Evaluation of potential sensor accelerometer designs 3
- 1.2 Modeling of sensor design to shock loading 5
  - 1.2.1 Methodology 5
  - 1.2.2 Results 5
    - 1.2.2.1 Single fiber sensor 5
    - 1.2.2.2 Mass-loaded fiber 6
    - 1.2.2.3 Cross-axial sensitivity 6
    - 1.2.2.4 Linearity of sensor's response 7
  - 1.2.3 Discussion 7
- 1.3 Bragg grating response to shock loading 7
  - 1.3.1 LED measurement technique 10
  - 1.3.2 Laser diode measurement technique 14
  - 1.3.3 Discussion 14
- 1.4 Analysis 14

2 Development of the sensor 18

- 2.1 Sensor design and measurement technique 18
  - 2.1.1 A reminder 18
  - 2.1.2 Sensor configuration selected 20
  - 2.1.3 The accelerometer 21
  - 2.1.4 Evaluation of the sensor dynamic range 22
- 2.2 Experimental configuration 28

2.2.1 Sensor mount 28
2.2.2 Signal generation and recovery 28
2.3 Results 32
2.3.1 Cantilever measurements 32
2.3.2 Fiber-Bragg sensor responses 32
2.3.3 Comparative analysis 34
2.4 Analysis 35
3 Tests at high accelerations 37
3.1 The Hopkinson bar 37
3.2 Modifications of experimental setup 39
3.2.1 Sensor 39
3.2.2 Setup 40
3.3 Results and analysis 41
3.3.1 Visits summary 41
3.3.2 Signals 42
3.3.3 Sensor responses 42
3.3.4 Linearity 45
3.3.5 Cross-axial measurements 46
3.3.6 Noise analysis 47
3.3.6.1 Aluminium mount 47
3.3.6.2 Ceramic ferrule 49
3.4 Analysis 51
4 Alternative detection scheme 53
4.1 New configuration 53
4.1.1 Scheme proposed 53
4.1.2 Principle 55
4.2 Theoretical results 56
4.3 Measurement setup 60
4.4 Experimental results 62
4.5 Analysis 65
5 Final Prototype 66
5.1 Schematic 66
5.2 Operation of the Final Prototype 67
5.3 Results 70
Conclusion 72
A Trigger setup and signals 74

B Sensor mount 76
C Fiber preparation 78
D Cantilever: filtering 80
E Original recordings 81
F Visits summary 84
G Program 89
H Specifications 90

List of Figures

1.1 Sensor design used in the finite element simulations. a) Bragg grating in a straight fiber. b) Bragg grating in a mass-loaded fiber. 4
1.2 Delta strain versus position at different times for the first half of the loading pulse for a 10 mm long bare fiber. 8
1.3 Delta strain versus position at different times for the first half of the loading pulse of a 4 mm long mass-loaded fiber. 9
1.4 Measurement setup using a broadband light source (LED). The entire reflection spectrum of the Bragg grating is integrated by the photodetector. 10
1.5 Measurement setup using a narrowband light source (laser diode). The photodetector measures the reflectivity of the Bragg grating at the discrete wavelength of the laser diode. 11
1.6 Ratio as a function of the chirp produced under acceleration of the spectral area of the reflected light of a chirped grating 3 mm long to the spectral area of the light from the same grating in the unchirped state. The different traces correspond to different maximum reflectivities in the unchirped state. 12
1.7 Ratio as a function of the chirp produced under acceleration of the spectral area of the reflected light of a chirped grating 10 mm long to the spectral area of the light from the same grating in the unchirped state. The different traces correspond to different maximum reflectivities in the unchirped state. 13
1.8 Variation in reflectivity of a 10 mm long fiber Bragg grating at twelve discrete wavelengths. The 12 wavelengths are identified in a) with letters from A to L. In b), c) and d) the variation of the reflectivities at each of the 12 wavelengths versus strain are shown. The length of the grating is 0.6 mm in a 10 mm long fiber. 15

1.9 Variation in reflectivity of a 4 mm long mass-loaded fiber Bragg grating at twelve discrete wavelengths. The 12 wavelengths are identified in a) with letters from A to L. In b), c) and d) the variation of the reflectivities at each of the 12 wavelengths versus strain are shown. The length of the grating is 0.2 mm in a 4 mm long mass-loaded fiber. 16

2.1 The two sensor options are a) the bare fiber case and b) the mass-loaded case. In both cases, the fiber is bound to the mount but a small length is free to stretch under an acceleration load. 19
2.2 Two strain detection schemes have been retained: In a), a light-emitting diode (LED) is combined with a long Bragg grating and in b), a laser diode is used with a short Bragg grating. 20
2.3 The measurement principle is based on the fiber elongation with strain, changing the grating period and resulting in a shift of the spectral response toward the long-wavelength region. 21
2.4 The principle of the accelerometer is based on the transfer of energy between a heavy steel ball striking a light anvil at rest. Two anvils were provided, one with a rubber pad and the other without. 22
2.5 The Bragg spectral shift caused by an acceleration of 6.5 kg$_n$ applied on a 1 mm-long grating:10 mm-long fiber. 24
2.6 Differential reflectivity of the sensor at the 6.5 kg$_n$ acceleration peak. 24
2.7 The Bragg spectral shift caused by an acceleration of 10 kg$_n$ applied on a 1 mm-long grating:10 mm-long fiber. 25
2.8 Differential reflectivity of the sensor at the 10 kg$_n$ acceleration peak. 25
2.9 The Bragg spectral shift caused by an acceleration of 50 kg$_n$ applied on a 1 mm-long grating:10 mm-long fiber. 26
2.10 Differential reflectivity of the sensor at the 50 kg$_n$ acceleration peak. 26
2.11 The Bragg spectral shift caused by an acceleration of 100 kg$_n$ applied on a 1 mm-long grating:10 mm-long fiber. 27
2.12 Differential reflectivity of the sensor at the 100 kg$_n$ acceleration peak. 27
2.13 Sensor mount. a) top view, b) side view showing the two different size grooves. 29
2.14 Expanded view of the sensor mount showing important lengths and the location of the Bragg grating. 29
2.15 The optical setup used for the detection of the grating spectral shift under acceleration. 30
2.16 Spectrum of the sensor Bragg grating. 31

2.17 Spectrum of the laser diode frequency-locked by a stabilized Bragg grating. . 32
2.18 Signals measured using Endevco sensor for the 3 balls provided. The cantilever was attached to the bare anvil. 33
2.19 Signals measured using Endevco sensor for the 3 balls provided. The cantilever was attached to the anvil with a rubber pad on its top. 33
2.20 Bragg grating sensor responses for the 3 balls provided when the wavelength of the laser diode is on the long-wavelength side of the grating spectrum. . . 34
2.21 Bragg grating sensor responses for the 3 balls provided when the wavelength of the laser diode is on the short-wavelength side of the grating spectrum. . . 35

3.1 Schematic of the Hopkinson bar apparatus. 38
3.2 Illustration of the sensor mount with the protective jacket now squeezed between both halves of the mount. 40
3.3 Illustration of the sensor mount used for the cross-axial experiments. 40
3.4 Relation of the detector bandwith versus the resistor gain value. 41
3.5 Comparison of the Bragg grating sensor response with the acceleration signal (derivative of the strain); a) strain, b) acceleration, c) sensor signal. 43
3.6 Sensor response showing the successive reflections of the compression wave. . 44
3.7 Typical response of the Bragg sensor at an acceleration of 67 kg_n. The acceleration (dots) and sensor (thin line) responses are plotted. 44
3.8 Typical response of the Bragg sensor at an acceleration of 137 kg_n. The acceleration (dots) and sensor (thin line) responses are plotted. 45
3.9 Linearity tests made using 3 different sensors. 46
3.10 Comparison between the first acceleration pulse and the resulting sensor signal. 47
3.11 Cross-axial measurement at an acceleration level of 85 kg_n. In a), a longitudinal measurement is plotted for comparison. 48
3.12 Effect on the sensor response when an aluminium mount is used a) with and b) without guiding rods. 49
3.13 Effect on the sensor response for two mounts with different hole diameter. . . 50
3.14 Longitudinal measurement of the sensor set in a ceramic ferrule inserted in a modified mount. The dotted circle at around 100 μs draws attention to a special feature associated only to the ceramic ferrule. 51
3.15 Cross-axial measurement made with the ceramic ferrule showing a strong sensor signal. 52

4.1 The laser detection scheme senses the level of light back-reflected by a sensor Bragg grating. 54

4.2 The principle of the detection is based on a change in the level of light back-reflected to the photodiode. 54
4.3 The new detection scheme uses an LED instead of a laser-diode and a second Bragg grating is put in front of the photodetector. 54
4.4 The LED spectrum is very wide compared to the Bragg spectrum. 55
4.5 A second configuration is possible by placing the photodetector at the end of the unused coupler arm. 56
4.6 The principle of the new detection scheme is based on the convolution (product) of the gratings' responses. In the convolution integration, the following scenarios are observed: a) gratings aligned b) slightly offset and c) completely offset. 57
4.7 Spectral convolution $S(\omega) \cdot (1 - R(\omega))$ between two identical uniform and apodized Bragg gratings. Linear regions are extracted for different tolerance errors on the linearity. 58
4.8 Spectral convolution $S(\omega) \cdot R(\omega)$ between two identical uniform and apodized Bragg gratings. Linear regions are extracted for different tolerance errors on the linearity. 59
4.9 Illustration of the new fiber mount using a ceramic ferrule. 61
4.10 Illustration of the setup used for the LED detection scheme. 62
4.11 Typical result for the $S(\omega) \cdot (1 - R(\omega))$ configuration. The level of the first pulse is fitted to the acceleration in the inset. 63
4.12 Typical result for the $S(\omega) \cdot R(\omega)$ configuration. The level of the first pulse is fitted to the acceleration in the inset. 64

5.1 Schematic of the final prototype. 67
5.2 Electrical schematic of the circuit. 68
5.3 Layout of the printed circuit board. 68
5.4 Ball-dropping low acceleration test measured using final prototype. 71

A.1 The trigger signals for the 3 balls provided. The curves are y-shifted for clarity. 75

B.1 Detailed description of the sensor mount. 77

C.1 The sensor preparation involves a) a precise cleaving of the fiber and b) a fiber end angle polishing to reduce unwanted back reflections. 79

D.1 Noise reduction by the introduction of a 100 kHz low-pass filter in the cantilever measurements. 80

List of Tables

4.1 Wavelength and reflectivity percentage variations for the different tolerance errors on the linearity. 60

Introduction

This report describes the feasibility study of a Fiber Bragg Grating (FBG) based accelerometer. FBGs are periodic modulation of the refractive index of the core in an optical fiber. This periodic modulation creates an optical narrowband reflection filter which can be used in a variety of applications in telecommunications and in sensing.

The first FBG was observed at the Communications Research Centre (CRC) by K. O. Hill in 1978. FBGs became a hot research topic in 1989 when side writing through the cladding was first demonstrated at United Technologies Corporation. What made FBGs practical devices was the phase mask writing technique developed at CRC in 1992. Now FBGs are manufactured in large quantities throughout the world.

This project is the first study of FBGs as accelerometers. FBGs have been studied for strain, temperature and hydrostatic pressure sensing because they have unique advantages over classical electrical systems. These advantages are electromagnetic interference immunity, light weight and small size, high temperature and radiation tolerance, flexibility, stability and durability against harsh environments. Also they have the advantage of being absolute, linear in response and of very low insertion loss so that they can be multiplexed in series for distributed sensing along a single monomode fiber.

The technique used in this study to sense acceleration is based on the measurement of the strain developed across a grating under acceleration. The strain is produced by the fiber own's weight which is free to stretch or compress under acceleration.

In phase 1 of the feasibility study modeling is carried out to evaluate the sensor's response to shock loading. The simulations identified as the most promising design a simple 10 mm long bare fiber with a 1 mm long FBG at the base of the free fiber. The interesting characteristics of this sensor are a near-linear response to acceleration and a large damping of the sensor's natural oscillation frequency. Also phase 1 proposes two techniques to measure the dynamic strain induced in the sensor. The first technique uses a narrowband laser diode to interrogate the sensor whereas the second one uses a broadband light emitting diode (LED). The two techniques are studied and compared.

In phase 2 the laser diode measurement setup is implemented, a sensor mount developed and low acceleration dynamic testing carried out.

Phase 3 includes high acceleration testing at 100,000 g_n carried out on the Hopkinson bar at DREV. Linearity of the sensor response and cross-axial sensitivity are studied.

In phase 4 the broadband light emitting diode measurement setup is implemented and its performance studied. The sensitivity, linearity and signal-to-noise ratio are investigated.

Finally phase 5 presents the final prototype. The laser diode measurement setup is used to build a compact battery operated sensor consisting of a FBG sensor head and the control unit which houses the electronics and opto-electronics components.

Phase 1

Design and modeling

Phase 1 of this feasibility study on the use of fiber Bragg gratings as high-g_n-level accelerometers consists in the preliminary design and the modeling of the sensor. The criteria used in the design of the sensor are: small size, simplicity of the structure, ease of measurement and high mechanical resonance frequency (≥ 1.5 MHz).

The modeling consists in the evaluation of the sensor's response to shock loading. The strain at different locations along the length of the fiber grating is modeled as a function of time during shock loading. The shock is simulated by an acceleration pulse with an amplitude of 100,000 g_n and a duration of 100 μs. Also sensitivity to lateral force (cross-axial sensitivity) is simulated by loading the sensor with an acceleration at an angle with respect to the fiber longitudinal axis. Finally the response of Bragg gratings to different strain distributions is modeled under two different scenarios for sensing acceleration using either a broadband or a narrowband light source.

1.1 Evaluation of potential sensor accelerometer designs

Several sensor designs using fiber Bragg gratings are possible. We considered the following options: a fiber cantilever with a Bragg grating in the free end of the cantilever, a fiber-bridge with a Bragg grating in the center of the span, a fiber-bridge with two Bragg gratings forming a Fabry-Perot and a straight fiber with its longitudinal axis parallel to the direction of the acceleration.

The most serious problem in the design of the sensor is to obtain a high sensitivity to acceleration and at the same time a high mechanical resonance frequency. Only the straight

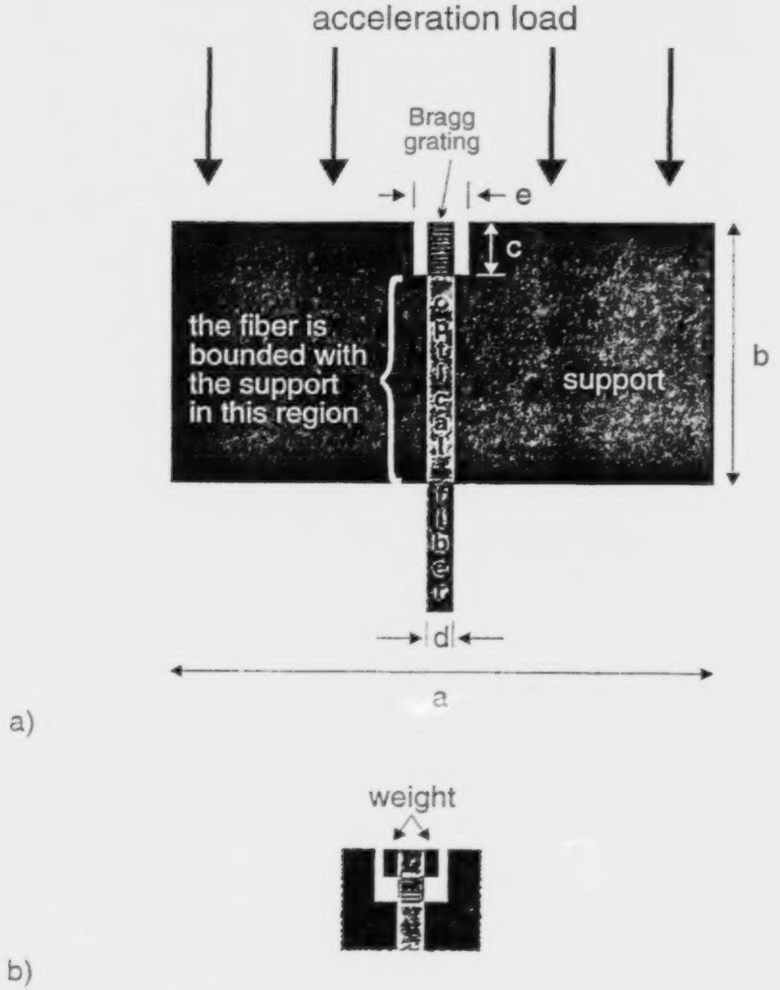
acceleration load
Bragg grating
e
c
b
the fiber is bounded with the support in this region
support
d
a
a)
weight
b)

Figure 1.1: Sensor design used in the finite element simulations. a) Bragg grating in a straight fiber. b) Bragg grating in a mass-loaded fiber.

fiber as shown in figure 1.1a has the potential to achieve enough sensitivity and still have a relatively high mechanical resonance frequency. Consequently the detailed finite element modeling was limited to considering the straight bare fiber and the mass-loaded configuration shown in figure 1.1. The precise characteristics of the sensor (e.g. fiber diameter, fiber length, length and diameter of mass attached to the fiber, Bragg grating length, location of grating in the fiber and reflectivity spectrum) will be determined from the modeling.

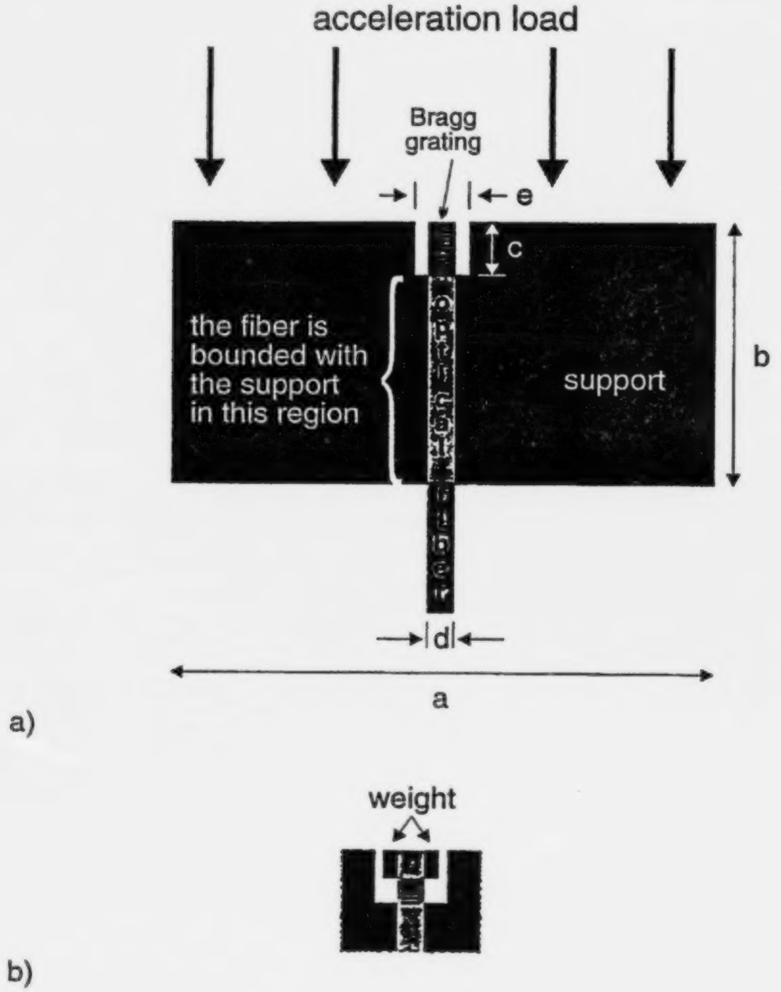
acceleration load
Bragg grating
e
c
the fiber is bounded with the support in this region
support
b
d
a
a)
weight
b)

Figure 1.1: Sensor design used in the finite element simulations. a) Bragg grating in a straight fiber. b) Bragg grating in a mass-loaded fiber.

fiber as shown in figure 1.1a has the potential to achieve enough sensitivity and still have a relatively high mechanical resonance frequency. Consequently the detailed finite element modeling was limited to considering the straight bare fiber and the mass-loaded configuration shown in figure 1.1. The precise characteristics of the sensor (e.g. fiber diameter, fiber length, length and diameter of mass attached to the fiber, Bragg grating length, location of grating in the fiber and reflectivity spectrum) will be determined from the modeling.

1.2 Modeling of sensor design to shock loading

A contract was issued to M. J. Worswick Analysis Ltd. to carry out the calculation of the distribution of stress and strain as a function of time within an optical fiber under acceleration. A copy of the final report is attached to this report. The two sensor configurations that were modeled are shown in figure 1.1.

1.2.1 Methodology

The finite element technique was used to determine the strain at different locations in the sensor configurations shown in figure 1.1. As discussed in the contractor's report, the finite element mesh required to model in two dimensions the fiber and its holder has so many elements that the computation time becomes excessive. Since preliminary calculation had shown that there is very little difference in the calculated stress between a bare fiber and a fiber in a holder, the calculations were simplified by modeling only a bare fiber without its holder.

The analysis of the cross-axial sensitivity of the sensor under shock loading at an arbitrary orientation to the longitudinal axis of the fiber requires the use of a 3D mesh. Again the computation time becomes excessive if the mesh grid is as fine as that used for the 2D calculations. Consequently a coarser mesh had to be used. Nevertheless the stress predictions are sufficiently accurate to assess the order-of-magnitude effect of the cross-axis acceleration on the response of the sensor.

It should be noted that the finite element technique used for the simulations doesn't have any built in damping. Because of this lack of damping we assume that the calculated frequency and the amplitude of the mechanical resonance of the system is a good approximation in spite of the fact that contribution of damping from the fiber holder is neglected in the calculations.

1.2.2 Results

1.2.2.1 Single fiber sensor

3 mm long fiber

In the case of a single bare fiber 3 mm long under an acceleration of 100,000 g_n, a maximum strain of about 10^{-4} is developed in the fiber and the resonance frequency is about 500 kHz. This strain is small and represents a lower limit for the sensitivity of a practical sensor. The resonance frequency of the bare fiber is 500 kHz which is low in comparison to the target of 1.5 MHz, but the amplitude of the resonant oscillations is only about 10% of the maximum strain.

10 mm long fiber

In order to increase the amount of strain developed in the fiber for 100,000 g_n acceleration, we lengthened the fiber. In this case the maximum amount of strain obtained is 3×10^{-4}, which represents a significant improvement over a 3 mm long fiber (see fig. 14 of M. J. Worswick Analysis report). Unfortunately the longer fiber has a lower resonance frequency, in this case about 150 kHz, but the amplitude of the oscillations are also smaller (about a few percents of the maximum strain). The large damping in the mechanical oscillations calculated for this fiber was unexpected and has not been explained at this point. The result makes the 10 mm long fiber sensor design interesting in that under acceleration a relatively high strain is obtained along with a large damping of the natural oscillation frequency.

1.2.2.2 Mass-loaded fiber

Another technique to increase the amount of strain in the sensor is to increase the mass of the free end of the fiber by coating it with a metallic film. Several designs for this sensor configuration were analyzed in which the length, size and type of mass on the fiber end is varied. In all cases of mass-loaded fiber sensor, the resonance frequency is typically below 300 kHz, and the amplitude of the mechanical oscillations are often many times the maximum strain obtained (see fig. 4 of M. J. Worswick Analysis report).

One configuration of particular interest is a fiber with a total length of 4 mm; the last 3 mm of the fiber is coated with gold to a thickness of 20 μm. The maximum strain for 100,000 g_n acceleration is 10^{-3} and the resonance frequency is about 150 kHz. The amplitude of the oscillations are less than 5% of the maximum strain (see fig. 8 of M. J. Worswick Analysis report). The design for this configuration is not optimum, nevertheless the result indicates that the mass-loaded sensor concept can achieve high strains with a high degree of damping of the natural frequency.

1.2.2.3 Cross-axial sensitivity

The cross-axial analysis was restricted to the 10 mm long bare fiber sensor configuration. A coarse 3D mesh was used and shown to give reasonably accurate results. Calculation of the bending stresses on the surface of the fiber indicates that the stress can be very large in some cases one or two order of magnitudes larger than the axial stress. However, these stresses don't affect the operation of the sensor because the bending stresses cancel out at the center of the fiber in the region where the optical signal propagates. Thus in-fiber Bragg grating acceleration sensor is insensitive to cross-axial loading because of its axial symmetry.

1.2.2.4 Linearity of sensor's response

Simulations were carried out to determine the linearity of the sensor response by calculating the stress developed for a shock loading of 50,000 g_n over 120 μs. In the case of both the 10 mm long bare fiber and the mass-loaded sensor configurations the strain of half the strain developed at 100,000 g_n over 70 μs indicating a very good linearity in the response.

1.2.3 Discussion

Based on the simulations carried out in this work, an in-fiber Bragg grating acceleration sensor with sufficient sensitivity and a resonance frequency larger than 500 kHz doesn't seem feasible. All the designs that produce large strains also have resonance frequencies well below 500 kHz. However the mass-loaded fiber or long bare fibers (e.g. 10 mm) can be designed to have sufficient sensitivity and yet even though the resonant frequency is low the oscillations are so strongly damped they are not important. In the section 1.3 the Bragg grating responses for the 3 mm long bare fiber, the 10 mm long bare fiber and the 4 mm long mass-loaded fiber sensor configuration are calculated.

1.3 Bragg grating response to shock loading

In order to calculate the Bragg grating response to shock loading we need to know the strain distribution along the length of the fiber versus time. The calculations of strain versus time for different locations along the length of the fiber (see fig. 10 and 13 of M. J. Worswick Analysis report) appear to respond linearly with acceleration if we ignore the oscillations of the mechanical resonance. This is confirmed in figure 1.2 and 1.3 which is a plot of the delta strain versus position at different times for the first half of the loading pulse. Only the first half (the rise) of the applied loading pulse is used because the oscillations of the resonance in this time frame are very small (typically $< 5\%$ of the full scale), in comparison to the oscillations in the latter half of the pulse. (A more appropriate way to analyze the linearity of the response is to take a Fourier transform of the strain versus time and to filter out the component due the mechanical resonance. Unfortunately, there are insufficient points to carry out the Fourier transform.). The responses shown in figure 1.2 and 1.3 confirm the linearity of the strain versus position at different times during shock loading and justify

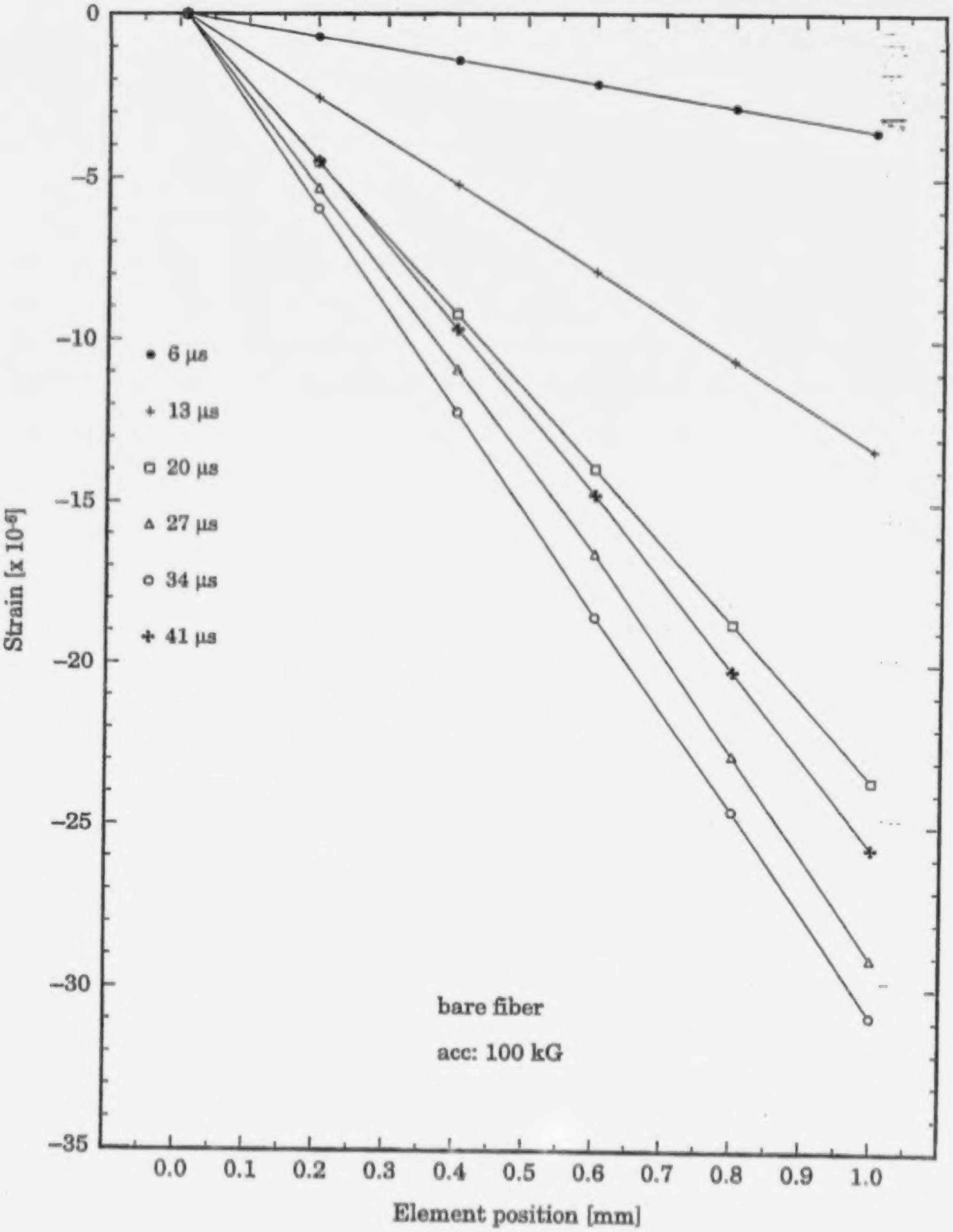

Figure 1.2: Delta strain versus position at different times for the first half of the loading pulse for a 10 mm long bare fiber.

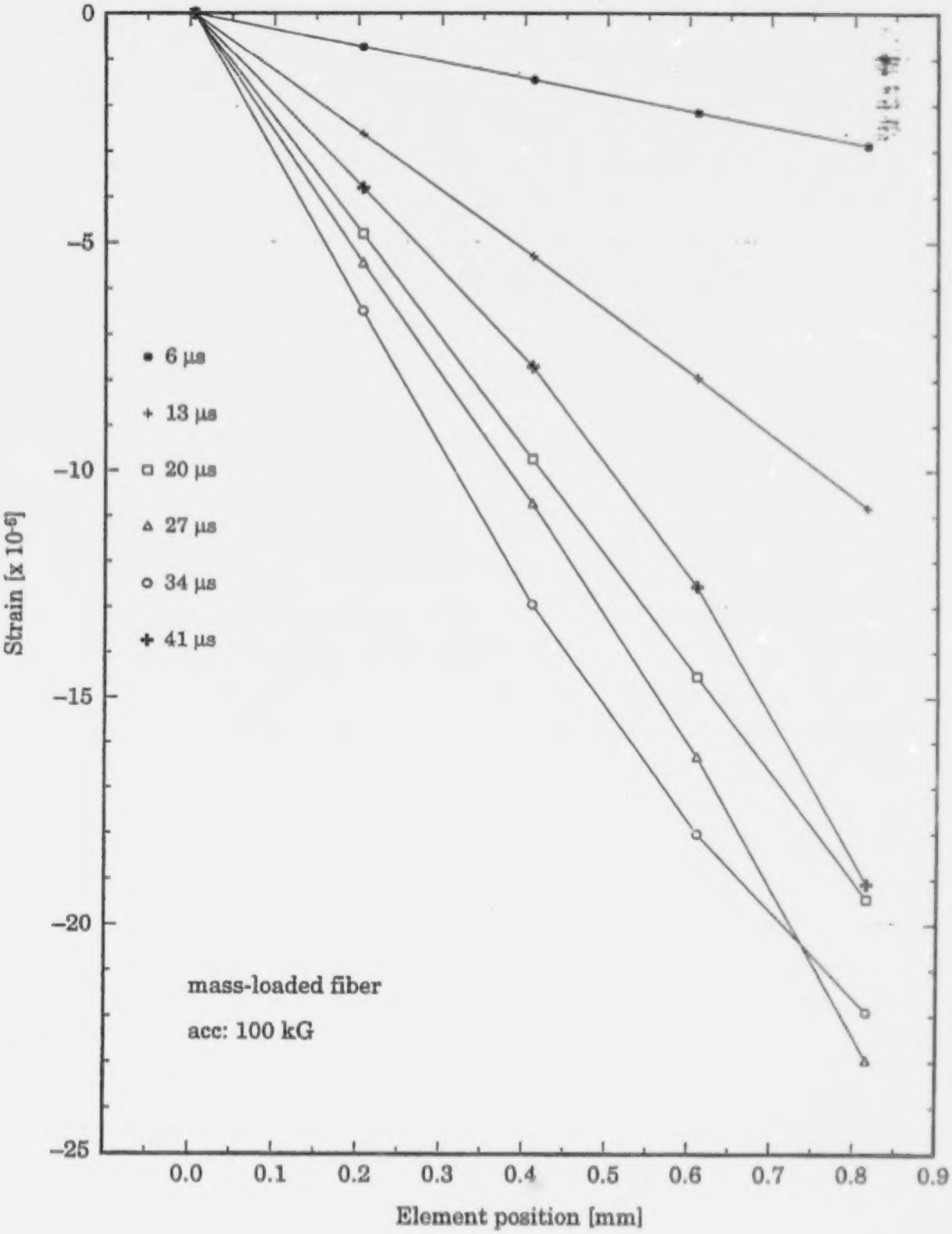

Figure 1.3: Delta strain versus position at different times for the first half of the loading pulse of a 4 mm long mass-loaded fiber.

the use of simple linear expressions for strain as a function of position instead of the more cumbersome data provided by M. J. Worswick Analysis.

Two simple measurement techniques are proposed for detecting the acceleration through the strain induced in the fiber Bragg grating. Figures 1.4 and 1.5 show these two techniques. In figure 1.4 an LED is used as a broadband source of light that has a FWHM (full width at half maximum) of about two order of magnitude larger than the reflection spectrum of the Bragg grating. The object of this technique is to integrate on the detector all of the light reflected from the Bragg grating. The technique is useful in measuring a strain which is nonuniform along the length of the fiber. With nonuniform strain, the bandwidth of the Bragg reflector broadens and its reflectivity will decrease; the total reflected light increases and is an indication of acceleration.

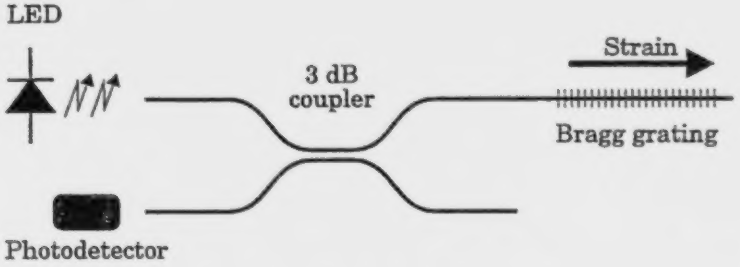

Figure 1.4: Measurement setup using a broadband light source (LED). The entire reflection spectrum of the Bragg grating is integrated by the photodetector.

The second method for detecting acceleration is shown in figure 1.5. In this case a semiconductor laser diode is used which is a narrowband light source. The FWHM of the laser is several order of magnitude smaller than the bandwidth of the Bragg grating reflector. The signal measured at the detector corresponds to the reflectivity of the Bragg grating at a discrete wavelength which has a strong dependence on the Bragg resonant wavelength. Under acceleration a uniform strain along the length of the Bragg grating shifts the resonant wavelength causing a change in reflectivity at a specific wavelength.

1.3.1 LED measurement technique

This measurement technique is intended to integrate all the light incident on the photodetector contained in the entire reflection spectrum of the Bragg grating. In this case we calculate the sensitivity and linearity of the integrated reflected spectrum for two type of Bragg gratings subjected to a linear variation of the strain along its length. We study a 3 mm long grating on a 3 mm long fiber and a 10 mm long grating on a 10 mm long fiber.

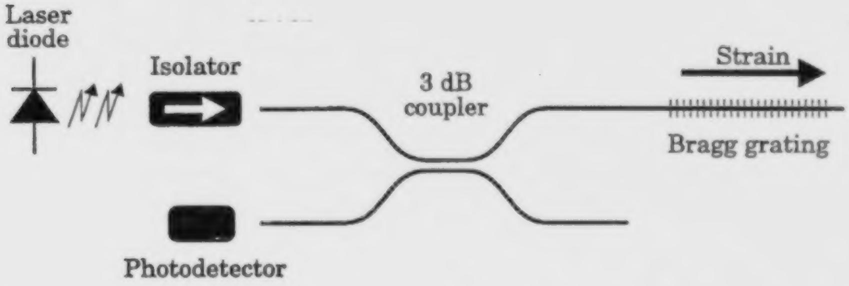

Figure 1.5: Measurement setup using a narrowband light source (laser diode). The photodetector measures the reflectivity of the Bragg grating at the discrete wavelength of the laser diode.

A change in the strain distribution along the length of a fiber Bragg grating spreads its spectrum (reflectivity versus wavelength) an effect that is commonly called "chirp" which is usually expressed as a percentage of change in the period of the grating. A uniform strain along the length of the grating shifts the entire resonant wavelength of the spectrum but the spectral shape does not broaden.

Figure 1.6 shows the response for the case of a 3 mm long Bragg grating at different reflectivities (the Bragg reflectivity can be controlled by changing the modulation of the photoinduced index of refraction). We define a quantity called the "spectral area ratio" which is the ratio of the reflected spectral areas of the chirped response over the unchirped one. The amount of strain developed along the fiber is quite small because of the short fiber length, thus the amount of chirp applied to the gratings is also small. Consequently, a small ratio is produced between the integrated power spectrum of the chirped response compared to the unchirped one. In figure 1.6 the maximum for the chirp along the abscissa, 0.01%, corresponds to the maximum strain calculated using the finite element method. The variation of the ratio versus the chirp is not linear and the maximum ratio of 1.1 is not very practical, i. e. under maximum strain there is a 10% increase in the light reflected onto the detector.

In figure 1.7 we see the result for a series of 10 mm long Bragg gratings. The ratio of the integrated power spectra is larger than in the case of the 3 mm long fiber reaching a maximum value of 2.5 for strong reflectivities of 99.99% and more. The response of the 99.99% and the 99.999% gratings approach a linear dependence. The maximum chirp of 0.03% correspond to the maximum strain of 0.03% calculated by the finite elements.

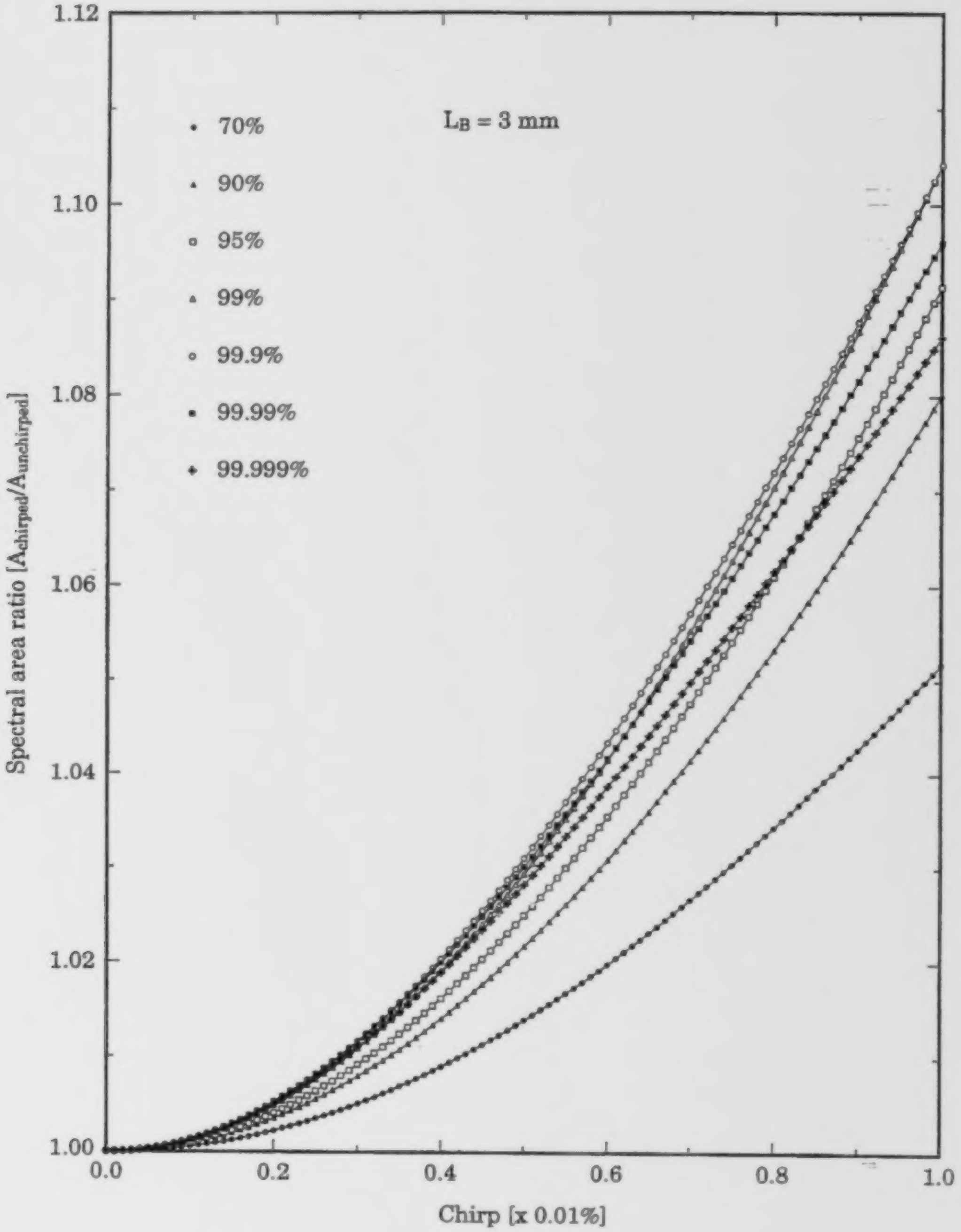

Figure 1.6: Ratio as a function of the chirp produced under acceleration of the spectral area of the reflected light of a chirped grating 3 mm long to the spectral area of the light from the same grating in the unchirped state. The different traces correspond to different maximum reflectivities in the unchirped state.

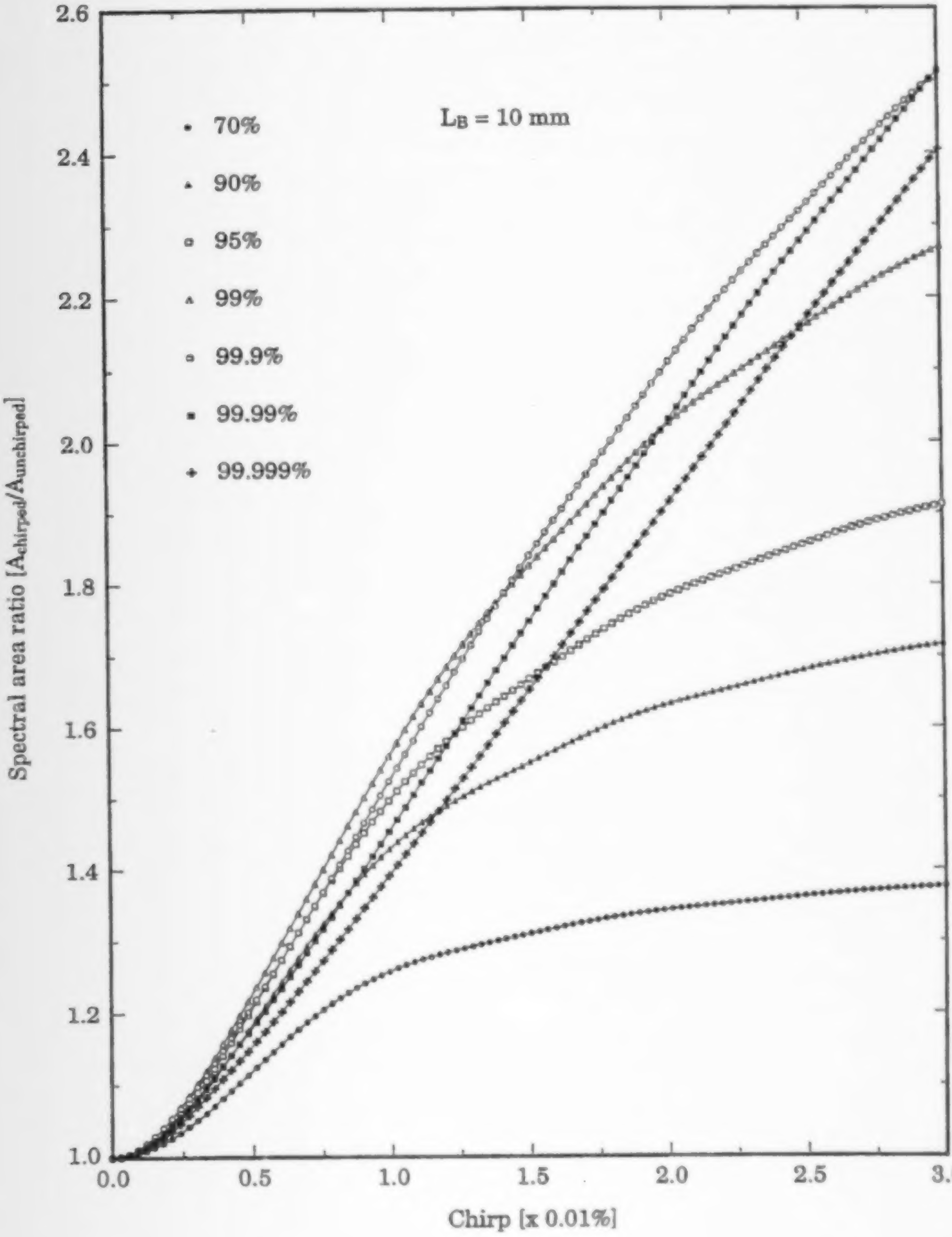

Figure 1.7: Ratio as a function of the chirp produced under acceleration of the spectral area of the reflected light of a chirped grating 10 mm long to the spectral area of the light from the same grating in the unchirped state. The different traces correspond to different maximum reflectivities in the unchirped state.

1.3.2 Laser diode measurement technique

This technique is intended to measure the change in reflectivity at a discrete wavelength for a Bragg grating under a uniform strain along its length. The effect of the uniform strain is to shift the sinc–like spectral reflection response of the grating keeping its shape constant. Thus chirp in the grating (a nonuniform strain along its length) is not desirable because it changes the shape of the Bragg response rather than shifting the center resonant wavelength. Two structures are reported here: a 0.6 mm long Bragg grating in a 10 mm long fiber and a 0.2 mm long grating in a 4 mm long mass-loaded fiber.

Figure 1.8 shows the change in reflectivity of the 10 mm long grating in a bare fiber. The 12 discrete wavelengths are chosen arbitrarily on the sinc–like response of a Bragg grating and are shown in figure 1.8a. In figure 1.8b, 1.8c and 1.8d we see the change in reflectivity at each of the 12 wavelengths as a function of the uniform strain developed across the fiber Bragg grating by accelerations. Wavelengths E and K show a reflection response that approaches a linear dependence on strain.

The same calculation was carried out for the 0.2 mm long Bragg grating in a 4 mm long mass-loaded fiber (see figure 1.9). The magnitude of the strain developed is 4 times larger than in the case of the 10 mm long bare fiber. Wavelengths E and K again have the most linear dependence on strain however the linearity is not as good as in the case of the bare fiber.

1.3.3 Discussion

The most promising approaches for the use of Bragg gratings as acceleration sensors are the 10 mm long Bragg grating using the LED measurement method, the 0.6 mm long grating in a 10 mm long fiber or the 0.2 mm long grating in a 4 mm long mass-loaded fiber using the laser diode measurement technique. The mass-loaded fiber approach generates the largest strain but the linearity of its response versus strain is not as good as in the case of the bare fiber. Thus the bare fiber using either the LED or the laser diode measurement technique appears to have the best potential for implementing a Bragg grating accelerometer. An important result in reaching this conclusion is the fact that the low mechanical resonance frequency of this sensor configuration is highly damped.

1.4 Analysis

Based on the results obtained in phase 1, phase 2 will consider only using bare fiber configurations. Because the different sensor configurations studied in phase 1 are not necessarily

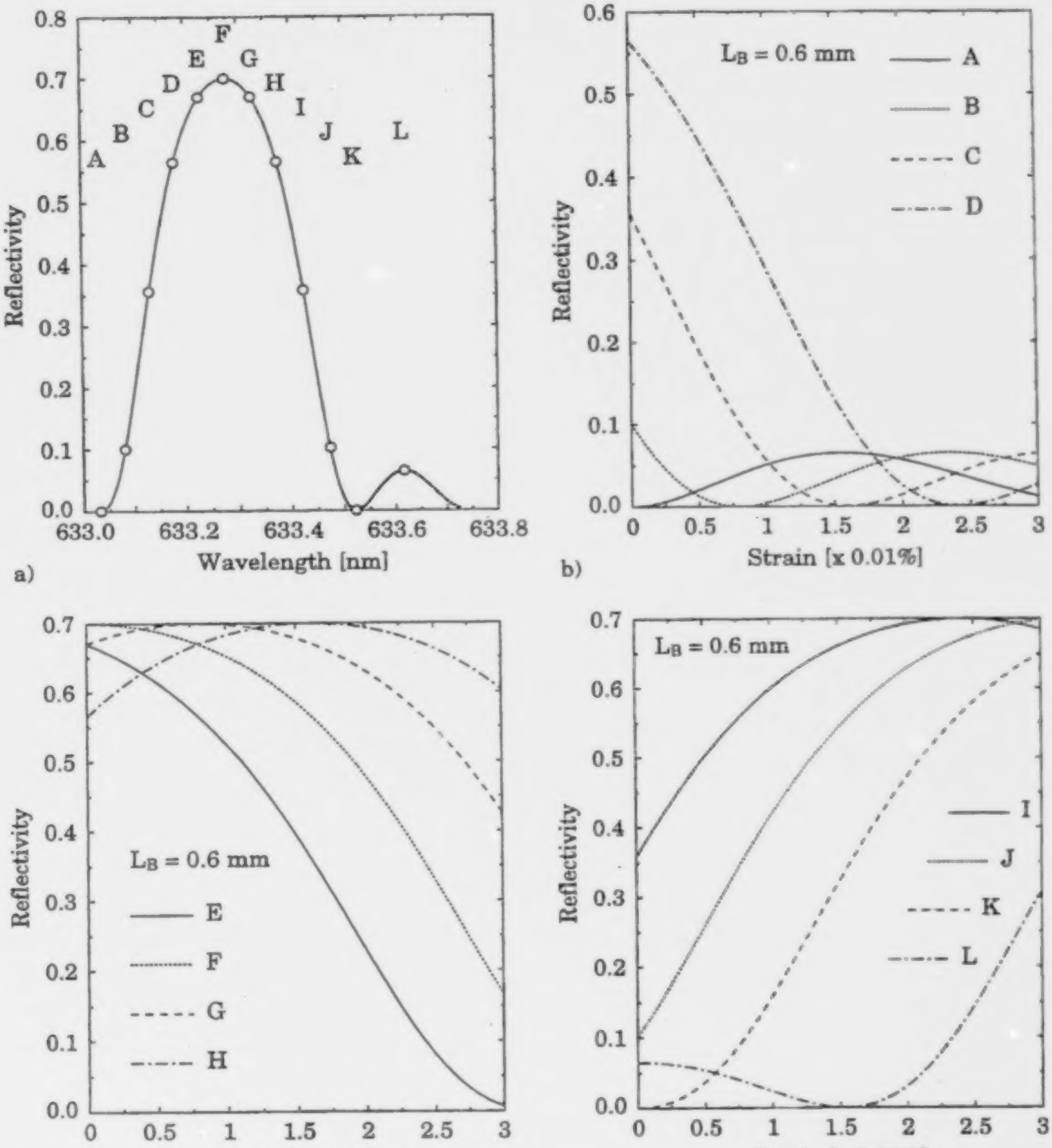

Figure 1.8: Variation in reflectivity of a 10 mm long fiber Bragg grating at twelve discrete wavelengths. The 12 wavelengths are identified in a) with letters from A to L. In b), c) and d) the variation of the reflectivities at each of the 12 wavelengths versus strain are shown. The length of the grating is 0.6 mm in a 10 mm long fiber.

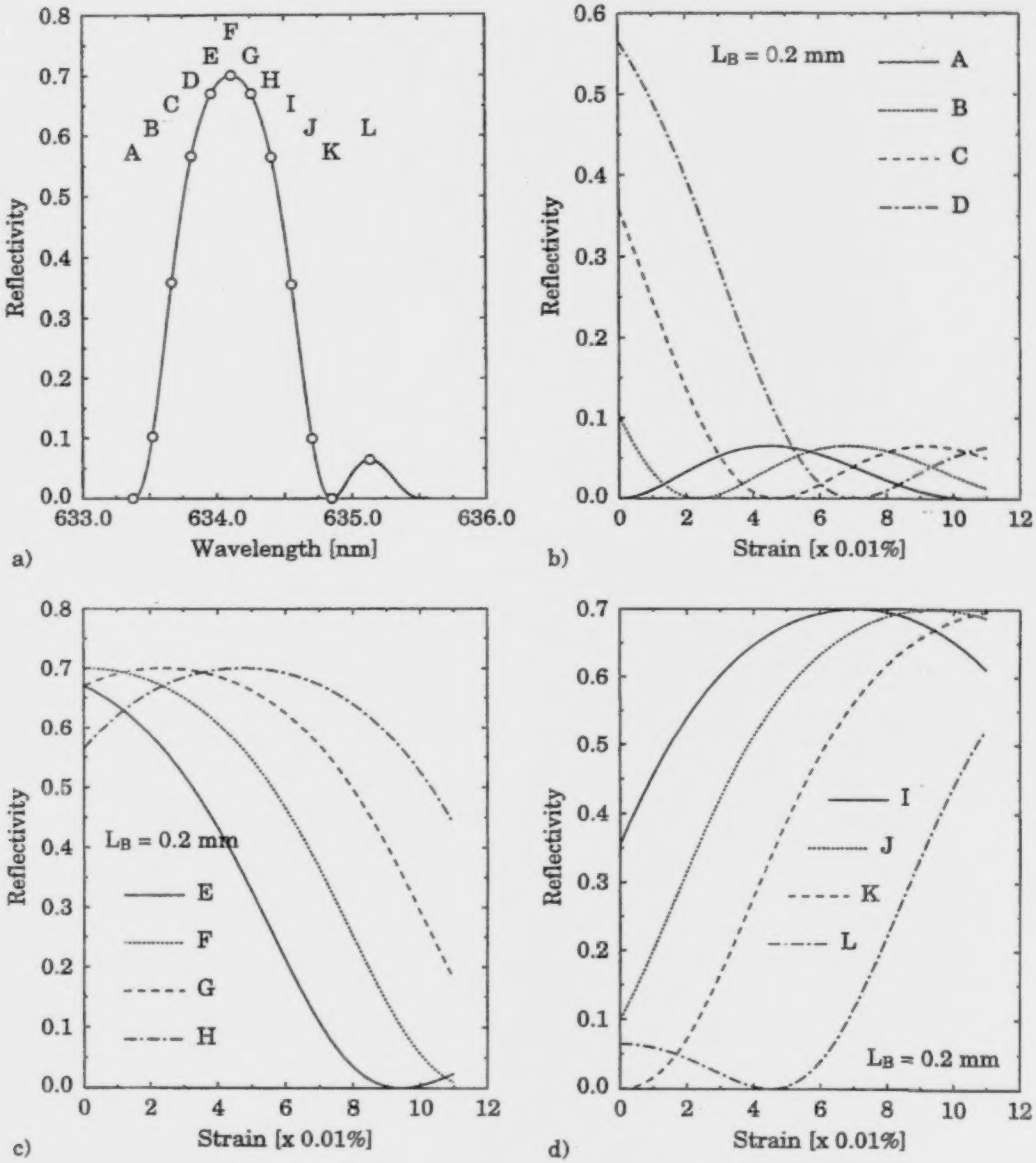

Figure 1.9: Variation in reflectivity of a 4 mm long mass-loaded fiber Bragg grating at twelve discrete wavelengths. The 12 wavelengths are identified in a) with letters from A to L. In b), c) and d) the variation of the reflectivities at each of the 12 wavelengths versus strain are shown. The length of the grating is 0.2 mm in a 4 mm long mass-loaded fiber.

optimum, we will test fibers having a length between 3 and 10 mm. The lengths of the Bragg gratings will vary also between a fraction of a millimeter to 10 mm. A 10 mm long phase mask will be needed to photoinduce the Bragg gratings. The choice of operating wavelength has not been determined and depends on the availability of suitable laser diodes and LEDs.

It is very important to confirm experimentally whether or not the large damping observed in the finite element simulations is in fact real. This result impacts the choice of the sensor configurations in the final design.

Phase 2

Development of the sensor

Numerical simulations carried out in phase 1 of this feasibility study demonstrated the potential of fiber-Bragg-gratings for acceleration sensing. Two fiber configurations were proposed, the long bare fiber and the short mass-loaded fiber. Two measurement techniques were proposed both providing real time electrical signals proportional to the acceleration.

The objectives of phase 2 are to develop and implement the measurement techniques proposed in phase 1, to develop a sensor mount and a packaging technique and to initiate dynamic testing at low g_n levels with a ball-dropping apparatus.

A decision was made to restrict the scope of the project to the development of one fiber configuration and one measurement technique. The most promising combination was selected, the long bare fiber sensor with a short Bragg grating and the laser diode as the narrowband light source.

This section starts with a short introduction on the sensor configuration selected then it describes the experimental setup which provides real time measurement of the acceleration, the sensor mount and packaging technique and finally introduces some measurements done at low acceleration levels.

2.1 Sensor design and measurement technique

2.1.1 A reminder

In phase 1, finite-element numerical simulations were performed to find out the best fiber configuration and the optimum measurement scheme. The basic concept of the fiber-Bragg sensor proposed here is based on the change in the spectral response of a Bragg grating when it experiences strain. The Bragg grating is located in the core of an optical fiber which is free to stretch under acceleration. A change in the period of the Bragg grating under strain can be detected and related to the acceleration load.

Two fiber-Bragg structures were analyzed in phase 1, a bare fiber and a mass-loaded fiber.. The proposed fiber structures are shown in figure 2.1 where a fiber is bound to a mount and a small length (< 10 mm) of the fiber is free to stretch. The fiber Bragg grating is located close to the fiber–mount interface. In figure 2.1b, a thin coating of metal is deposited on the fiber surface to increase the sensor weight.

Two detection schemes were considered to measure the acceleration. The first scheme, shown in figure 2.2a, uses an LED as an optical source and a long grating as the sensor. The LED spectrum is much broader than the Bragg spectrum thus the reflected light detected by the photodetector is the spectral integration of the grating response. Under acceleration the total light reflected by the grating changes because the grating becomes chirped, i.e. its period becomes non-uniform along the fiber. The shape of the spectrum changes and the value of the integration of the light back reflected changes.

The second scheme consists in a laser diode used in combination with a short Bragg grating. In this case, the Bragg spectrum is much broader than the laser spectrum. Thus the laser light reflected by the grating corresponds to the reflectivity of the Bragg grating at

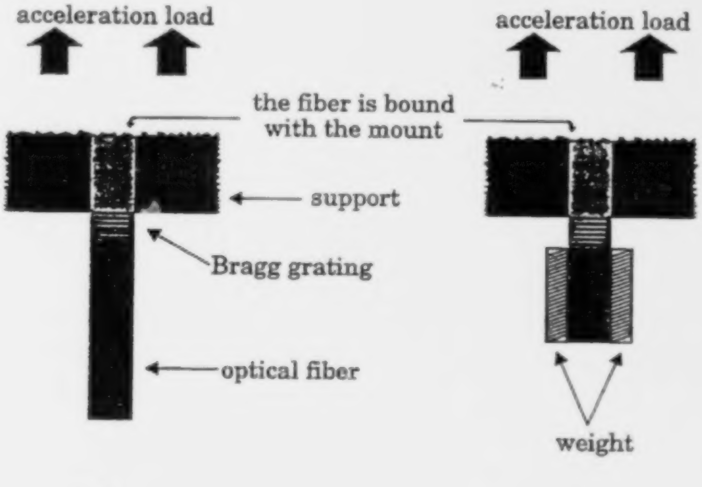

a)

b)

Figure 2.1: The two sensor options are a) the bare fiber case and b) the mass-loaded case. In both cases, the fiber is bound to the mount but a small length is free to stretch under an acceleration load.

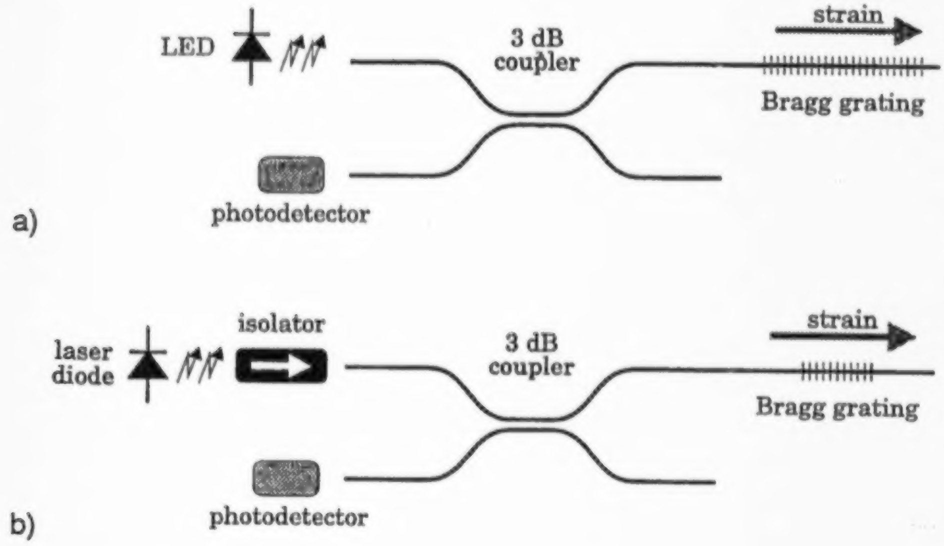

Figure 2.2: Two strain detection schemes have been retained: In a), a light-emitting diode (LED) is combined with a long Bragg grating and in b), a laser diode is used with a short Bragg grating.

a discrete wavelength. Under acceleration, the Bragg spectral response shifts and changes the level of light reflected.

2.1.2 Sensor configuration selected

The design configuration chosen for phase 2, 3 and 4 of the feasibility study is the 10 mm long bare fiber. For this configuration a short 1 mm long Bragg grating is located at the base of the free fiber as shown in figure 2.3. Used in combination with the laser scheme, this design was identified as the most promising in phase 1.

The advantages of this configuration is the large dynamic range that is obtained and the natural damping that limits the amplitude of the resonance frequency. The laser scheme is also more linear and more sensitive compared to the LED scheme. However the setup is more complex.

Based on the modeling done in phase 1, we consider that a short Bragg grating (e.g. 1 mm) is subjected to a uniform strain along its length if the free fiber is an order of magnitude longer than the grating. Under these conditions a 10 mm long free fiber under acceleration produces a quasi-uniform strain along the length of the short grating and the sinc-like response of the Bragg grating simply shifts without any significant chirp (the chirp

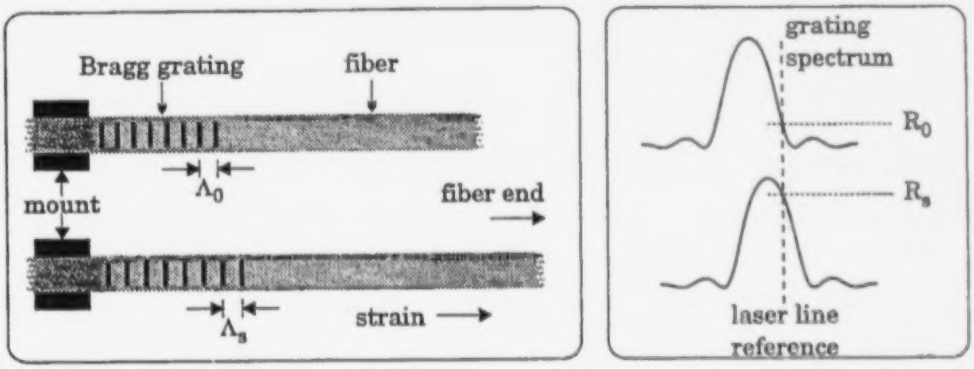

Figure 2.3: The measurement principle is based on the fiber elongation with strain, changing the grating period and resulting in a shift of the spectral response toward the long-wavelength region.

is a spreading of the spectral response which increases the full width at half maximum of the sinc-like response).

The detection technique used for this configuration is based on a simple wavelength shift of the Bragg spectral characteristic (see figure 2.3). This wavelength shift is measured against the emission wavelength of the reference laser diode because the reflectivity of the grating changes at the laser frequency. If we consider that the spectrum moves toward long wavelengths, the reflected light level will increase if the laser is located on the right side of the grating spectrum (see figure 2.3), $R_0 \rightarrow R_s$, or will decrease if the laser is located on the left side.

2.1.3 The accelerometer

The fiber Bragg grating sensor was tested under low accelerations using a ball-dropping apparatus supplied by DREV. The schematic of the accelerometer is presented in figure 2.4. The acceleration is generated by dropping a steel ball inside a column on a lightweight anvil which holds the sensor. Two anvils were provided with the apparatus. One anvil has a rubber pad to attenuate the shock. Also three steel balls of 1, 1.5 and 2 inches in diameter were provided.

The maximum acceleration possible with this instrument is about 12 kg_n. However, the average accelerations are respectively 10 kg_n for the bare anvil and 6.5 kg_n for the anvil with a rubber pad.

As shown in figure 2.4, we added an optical trigger to the accelerometer to detect the passage of the ball into the column. This trigger is used to start the acquisition of data

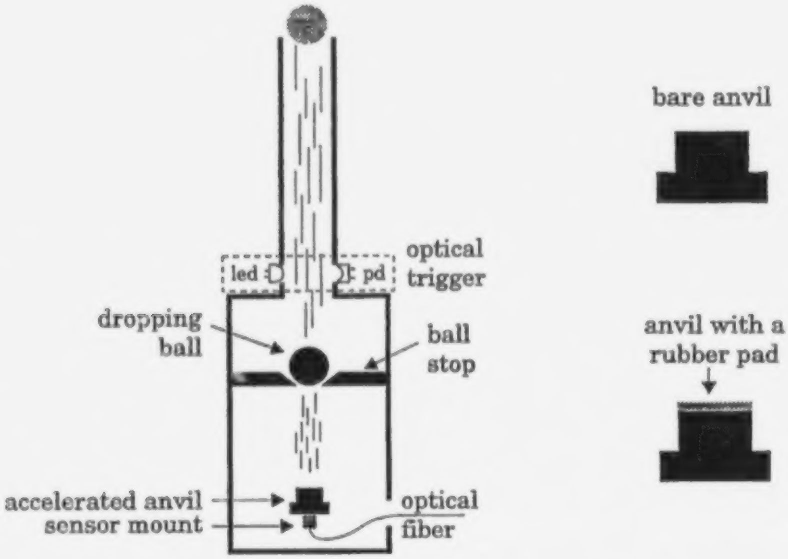

Figure 2.4: The principle of the accelerometer is based on the transfer of energy between a heavy steel ball striking a light anvil at rest. Two anvils were provided, one with a rubber pad and the other without.

provided by the sensor. More details on this trigger are presented in appendix A.

The ball dropping setup was especially useful to developed the measurement technique. The highest accelerations possible correspond only to about 10% of the maximum scale of the sensor so this series of results is insufficient to draw any conclusion on the overall performance of the sensor. Tests up to 100 kg$_n$ will be carried out during phase 3 at DREV using an Hopkinson bar.

2.1.4 Evaluation of the sensor dynamic range

Before attempting any experience it is necessary to determine precisely what is the expected response of the sensor under different scenarios. Using the selected fiber-configuration (1 mm–long Bragg grating at the base of a 10 mm–long bare fiber) we need to determine the best wavelength of operation for the laser diode given the grating specifications. The selected wavelength of operation should give the maximum variation in reflectivity for a given acceleration, and also the most linear response.

Four scenarios are considered here corresponding to acceleration levels of 6.5 kg$_n$ and 10 kg$_n$ provided by the ball-dropping apparatus, and 50 kg$_n$ and 100 kg$_n$ that will be tested on the Hopkinson bar at DREV. The values used for the wavelength shifts are based on the strain simulations carried out in phase 1.

For comparison purposes the spectrum of the Bragg grating at rest is plotted with its shifted version for the 4 scenarios in figures 2.5, 2.7, 2.9 and 2.11. For each case the difference in reflectivity between the reflectivity at rest and the reflectivity once shifted under maximum acceleration is calculated for each possible wavelength of operation and plotted in figures 2.6, 2.8, 2.10 and 2.12. For example in fig. 2.6 the graph indicates that a maximum change in reflectivity of 0.07 is detected for a wavelength of operation of the laser diode 0.18 nm longer or 0.15 nm shorter than the center wavelength of the Bragg grating at rest. Figures 2.8 and 2.10 show maximum differential reflectivities of 0.11 and 0.45 respectively for 10 kg_n and 50 kg_n for offset wavelengths of +0.2 nm or −0.1 nm. The maximum change in reflectivity occurs for an acceleration of 100 kg_n as shown in fig. 2.12, but the wavelength shift produced in this case is too large to be practical. It is clear by inspecting fig. 2.11 that the amount of offset created by the acceleration is larger than the quasi linear region of the Bragg grating slope located between the offset wavelengths of 0.05 nm and 0.2 nm. This creates a nonlinear response and must be avoided. To correct this problem a shorter length of bare fiber can be used to reduced the amount of strain developed in the grating. Also the use of a shorter Bragg grating would increase the bandwidth of the spectrum and thus extend the quasi-linear region of operation.

For the low level accelerations in phase 2 we selected a 1 mm long Bragg grating in a 10 mm long bare fiber in spite of the fact that it is not acceptable for the maximum scale of 100 kg_n. This way the sensor offers slightly more sensitivity for the ball-dropping setup which generates accelerations of only about 10% of the maximum scale. For optimum operation with the selected sensor configuration the laser emission wavelength should be located 0.2 nm longer than the peak of the Bragg grating at rest or 0.1 nm shorter.

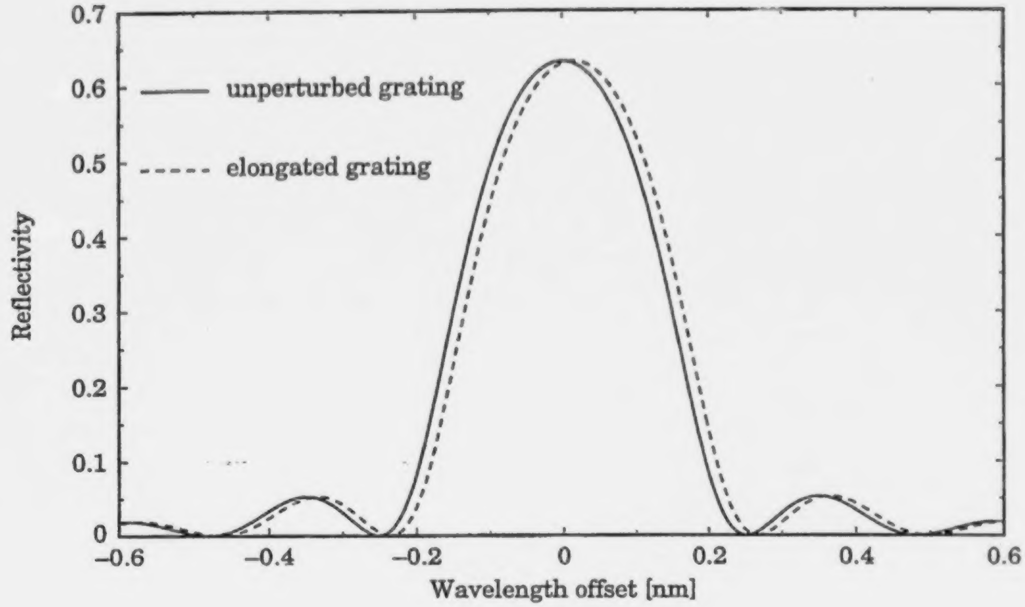

Figure 2.5: The Bragg spectral shift caused by an acceleration of 6.5 kg_n applied on a 1 mm-long grating:10 mm-long fiber.

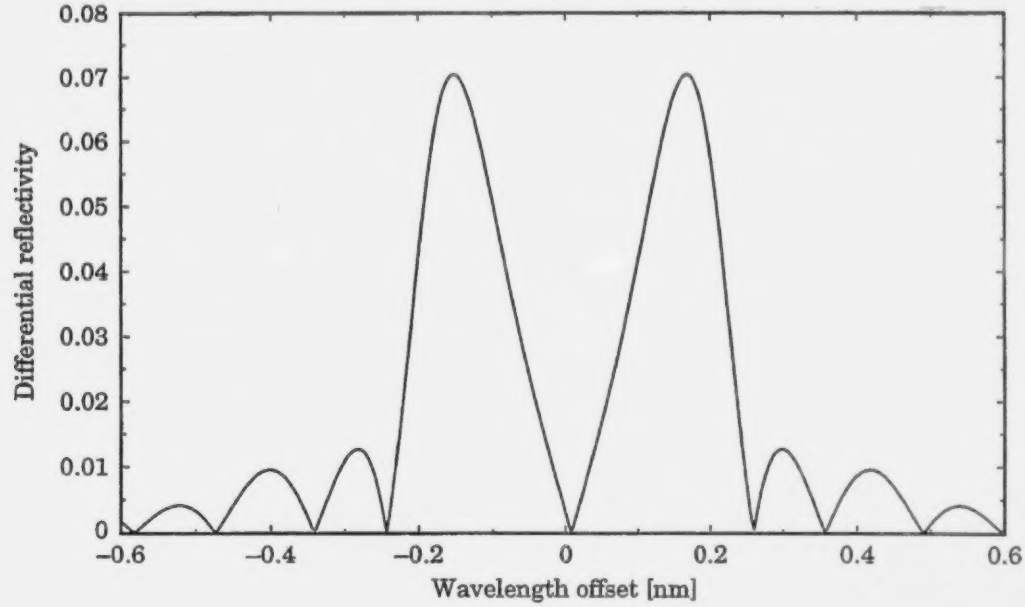

Figure 2.6: Differential reflectivity of the sensor at the 6.5 kg_n acceleration peak.

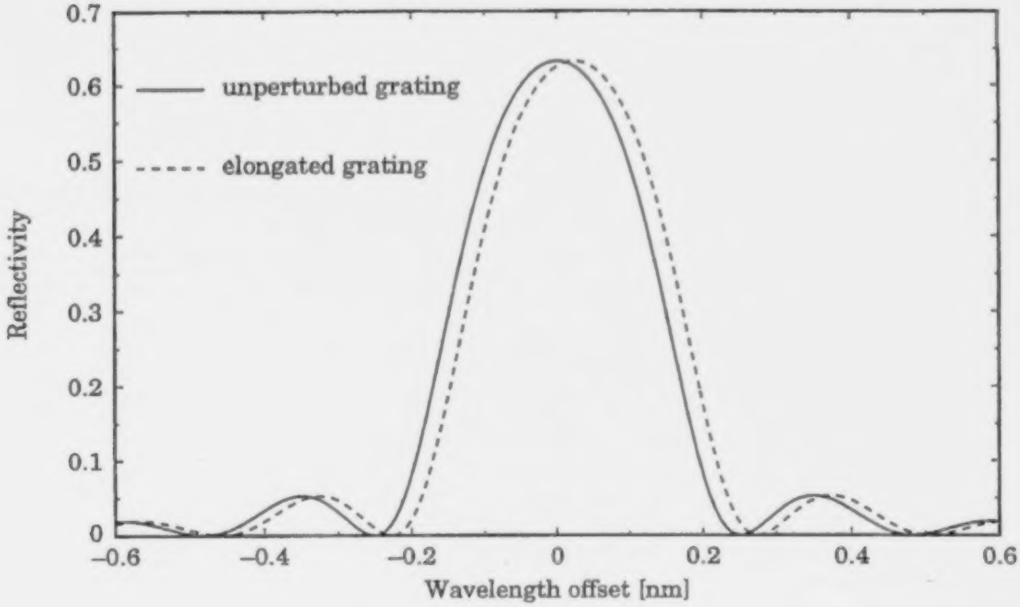

Figure 2.7: The Bragg spectral shift caused by an acceleration of 10 kg_n applied on a 1 mm-long grating:10 mm-long fiber.

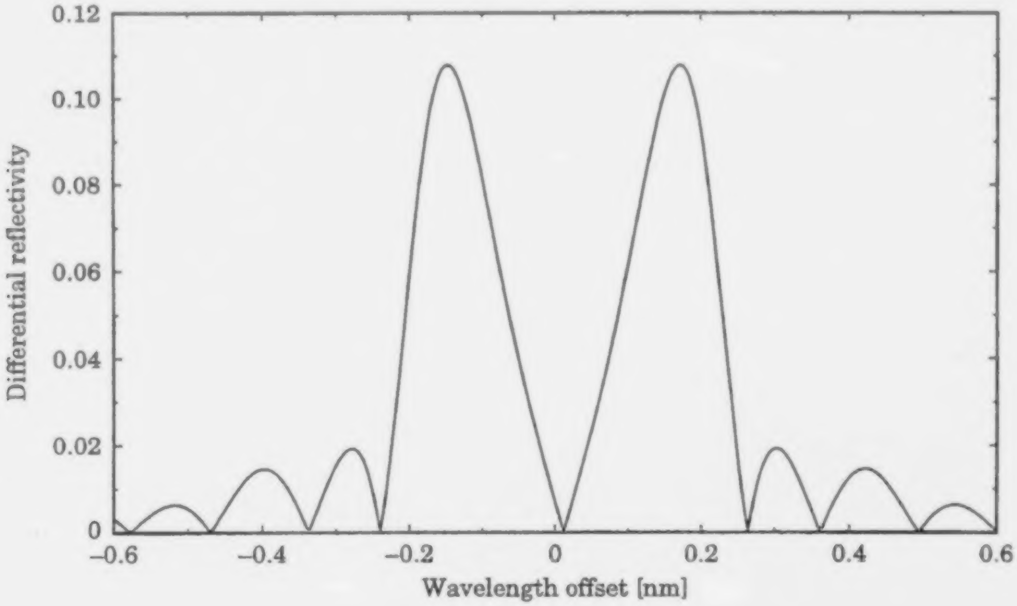

Figure 2.8: Differential reflectivity of the sensor at the 10 kg_n acceleration peak.

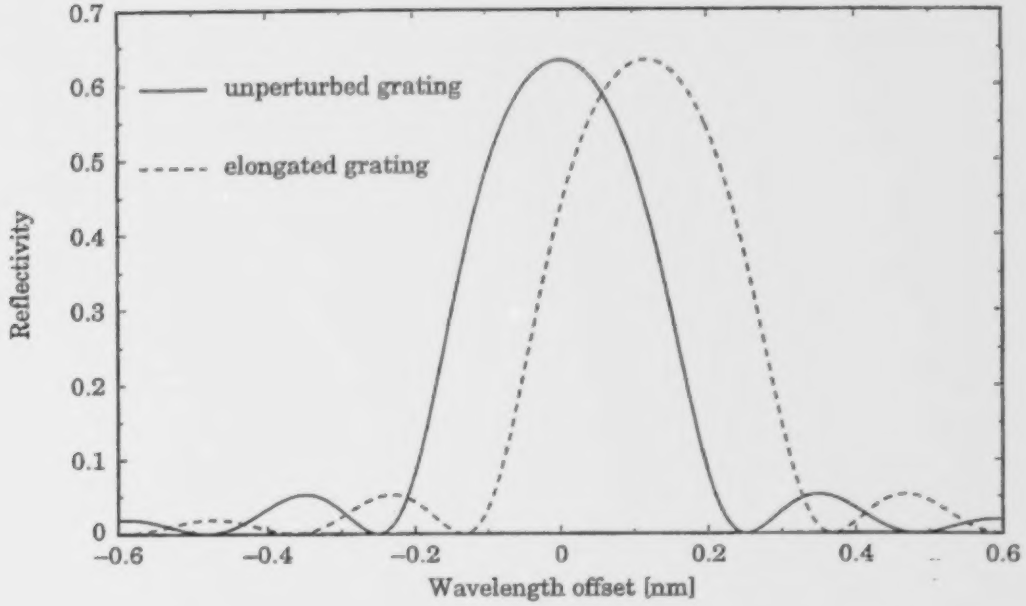

Figure 2.9: The Bragg spectral shift caused by an acceleration of 50 kg_n applied on a 1 mm-long grating:10 mm-long fiber.

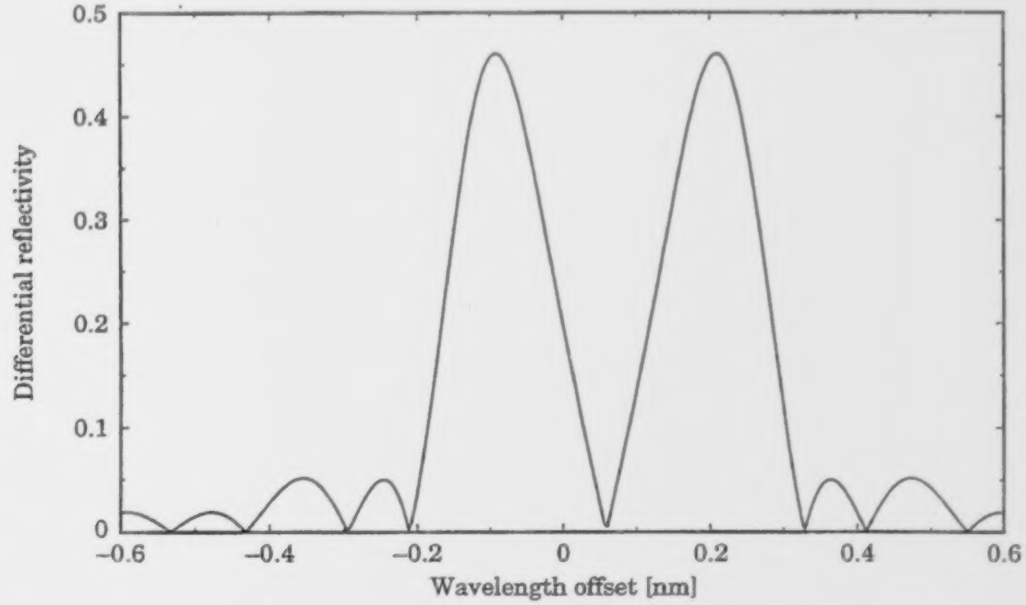

Figure 2.10: Differential reflectivity of the sensor at the 50 kg_n acceleration peak.

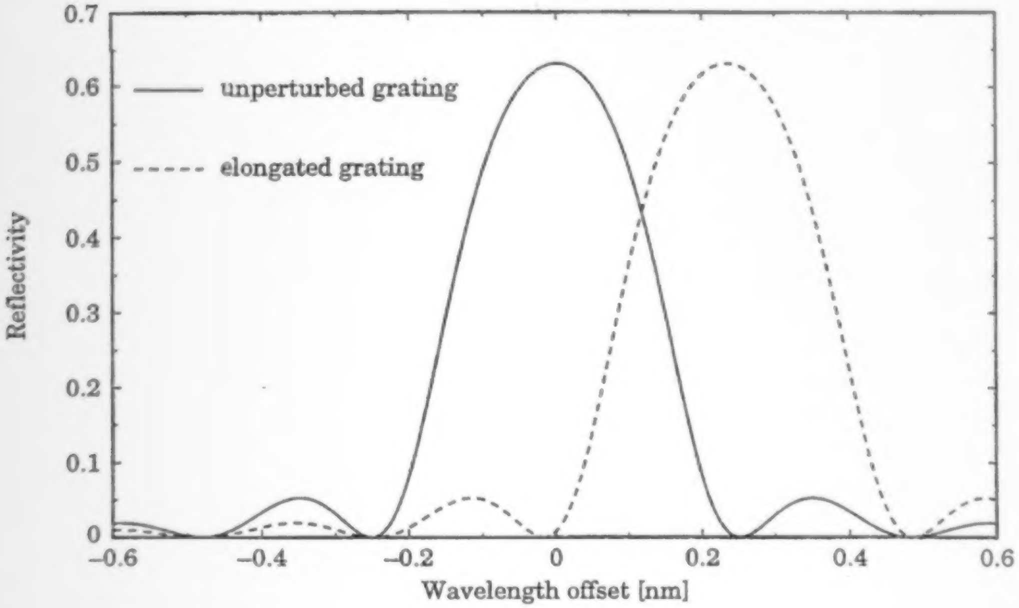

Figure 2.11: The Bragg spectral shift caused by an acceleration of 100 kg$_n$ applied on a 1 mm-long grating:10 mm-long fiber.

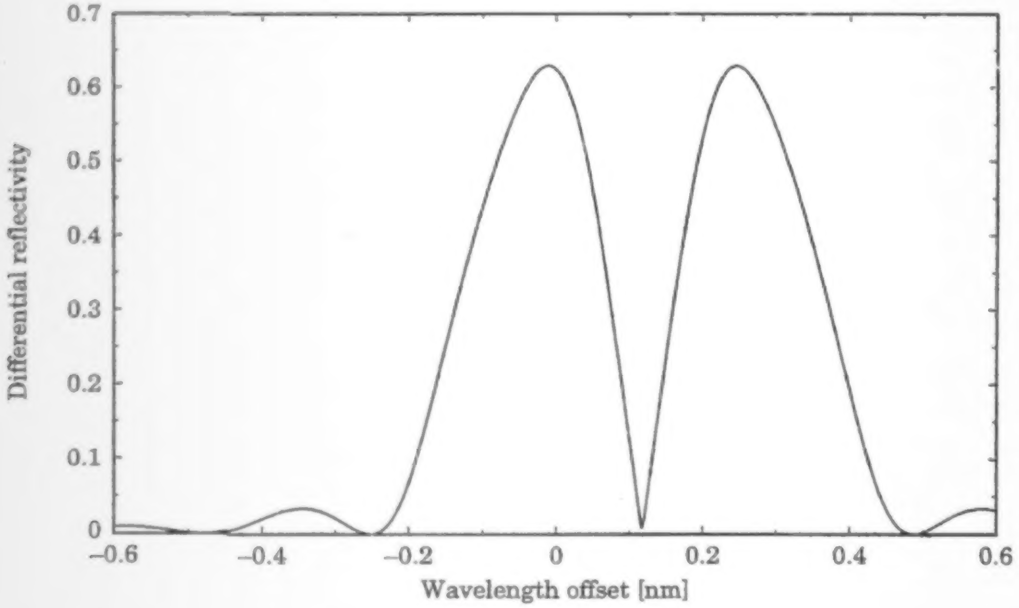

Figure 2.12: Differential reflectivity of the sensor at the 100 kg$_n$ acceleration peak.

2.2 Experimental configuration

2.2.1 Sensor mount

The function of the sensor mount is to hold the optical fiber in close proximity to the Bragg grating and to leave the free fiber unobstructed and free to stretch under acceleration. Figure 2.13 shows the schematic of the mount. The material used to make the mount is aluminum (Al 6061-T6). In order to make the mount reusable it is constructed of 2 half cylinders (fig. 2.13a). The 2 halves are secured together using 4 setscrews. The optical fiber lays inside two set of grooves. The first groove is 60 μm deep, 5 mm long and is designed to hold tightly a bare fiber of 125 μm diameter; the second groove is 500 μm deep, 1 cm long and protects the free fiber without holding it. Also the long groove prevents the bare fiber from bending under cross-axial load which could chirp the response of the grating. More details on the sensor mount are presented in appendix B.

The fiber has to be positioned very accurately inside the mount. Before mounting the fiber the Bragg grating has to be photoimprinted about 5.5 mm away from the end of the protective coating of the fiber (see fig. 2.14). This is important to make sure that the grating is located at the base of the free fiber, that 5 mm of bare fiber is tightly secured in the mount and that a minimum length of bare fiber is exposed outside of the mount where it can be easily broken. Glue is used to cover whatever length of bare fiber that extends outside of the mount.

In order to get the desired length of free fiber, a precise cleave of the fiber is practiced using a diamond tip. The cleaved fiber end is then polished at a specific angle to get rid of any unwanted reflections. This results in a better signal to noise ratio for the measurement. More details on the fiber preparation are presented in appendix C.

2.2.2 Signal generation and recovery

A schematic of the measurement setup is shown in figure 2.15. It consists of a stabilized laser diode as a narrowband light source, a 3 dB fused coupler, a Bragg grating as the sensing element and a high-sensitivity photodetector. The measurement of acceleration is based on the wavelength shift of the Bragg sensor response.

From this experimental setup real time measurement of the acceleration becomes a simple evaluation of the light power reflected back by the grating into the detector. The signal measured by the detector at any time corresponds simply to the light reflectivity of the Bragg grating at the discrete wavelength of the laser diode. The linewidth of the laser diode is about 10 MHz and is several orders of magnitude smaller than the spectral full width at

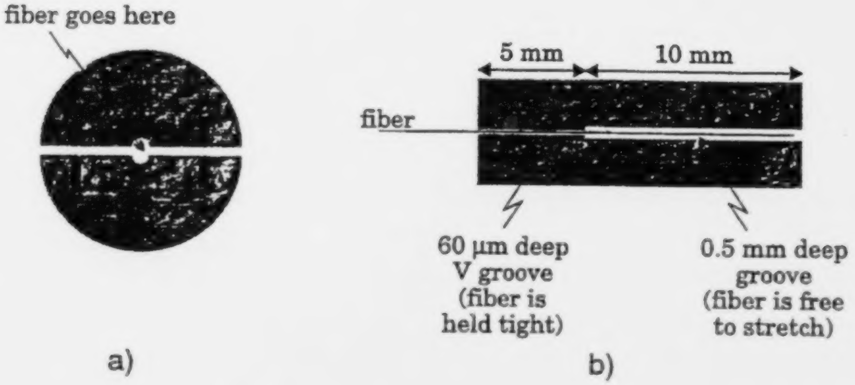
fiber goes here
5 mm
10 mm
fiber
60 µm deep
V groove
(fiber is
held tight)
0.5 mm deep
groove
(fiber is free
to stretch)
a)
b)

Figure 2.13: Sensor mount. a) top view, b) side view showing the two different size grooves.

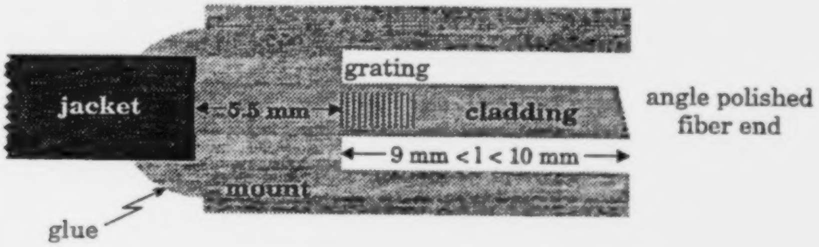
jacket
5.5 mm
grating
cladding
angle polished
fiber end
9 mm < l < 10 mm
mount
glue

Figure 2.14: Expanded view of the sensor mount showing important lengths and the location of the Bragg grating.

half maximum (FWHM) of the Bragg grating which is approximately 1 nm (435 GHz at 830 nm). In order to obtain the largest dynamic range possible the emission wavelength of the laser diode is located in the quasi-linear region of spectral response of the grating.

The relative position of the laser diode emission wavelength versus the Bragg grating response is critical. Without the presence of any acceleration the light power reflected by the Bragg grating has to be stable and insensitive to any environmental change. Any sudden relative shift between the source and the grating would be interpreted as an acceleration. Because the Bragg grating and the laser are affected differently by environmental changes, a slow drift of the ambient temperature for example would change the relative position of the laser wavelength versus the spectrum of the Bragg grating. This problem would affect the sensor performance and is clearly undesirable.

The technique developed to control the emission wavelength of the laser source and to avoid differential spectral shifts caused by environmental variations is the use of a second Bragg grating to stabilize the laser diode. This second Bragg grating acts as an external cavity to the laser and locks the emission wavelength. This second Bragg grating is slightly

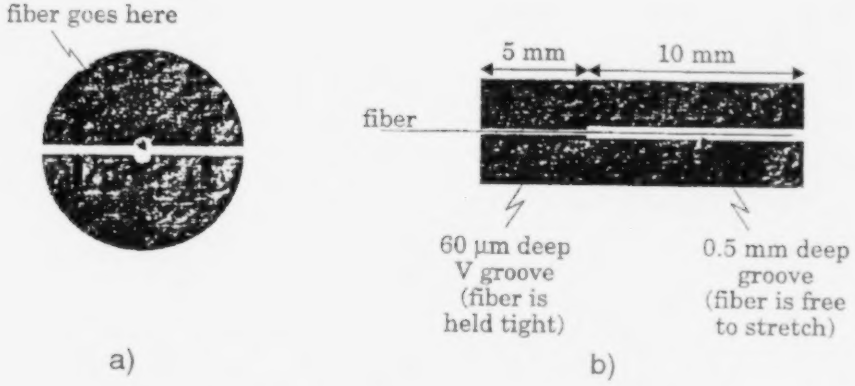
fiber goes here
5 mm
10 mm
fiber
60 μm deep V groove (fiber is held tight)
0.5 mm deep groove (fiber is free to stretch)
a)
b)

Figure 2.13: Sensor mount. a) top view, b) side view showing the two different size grooves.

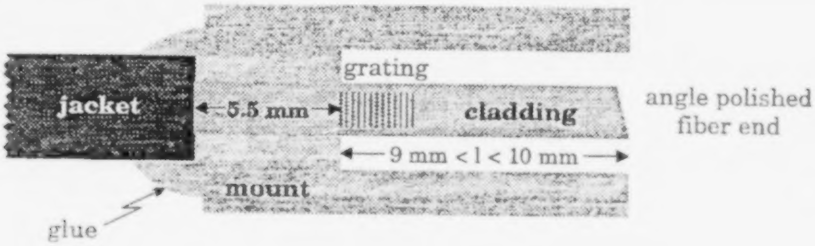
grating
jacket
5.5 mm
cladding
angle polished fiber end
9 mm < l < 10 mm
mount
glue

Figure 2.14: Expanded view of the sensor mount showing important lengths and the location of the Bragg grating.

half maximum (FWHM) of the Bragg grating which is approximately 1 nm (435 GHz at 830 nm). In order to obtain the largest dynamic range possible the emission wavelength of the laser diode is located in the quasi-linear region of spectral response of the grating.

The relative position of the laser diode emission wavelength versus the Bragg grating response is critical. Without the presence of any acceleration the light power reflected by the Bragg grating has to be stable and insensitive to any environmental change. Any sudden relative shift between the source and the grating would be interpreted as an acceleration. Because the Bragg grating and the laser are affected differently by environmental changes, a slow drift of the ambient temperature for example would change the relative position of the laser wavelength versus the spectrum of the Bragg grating. This problem would affect the sensor performance and is clearly undesirable.

The technique developed to control the emission wavelength of the laser source and to avoid differential spectral shifts caused by environmental variations is the use of a second Bragg grating to stabilize the laser diode. This second Bragg grating acts as an external cavity to the laser and locks the emission wavelength. This second Bragg grating is slightly

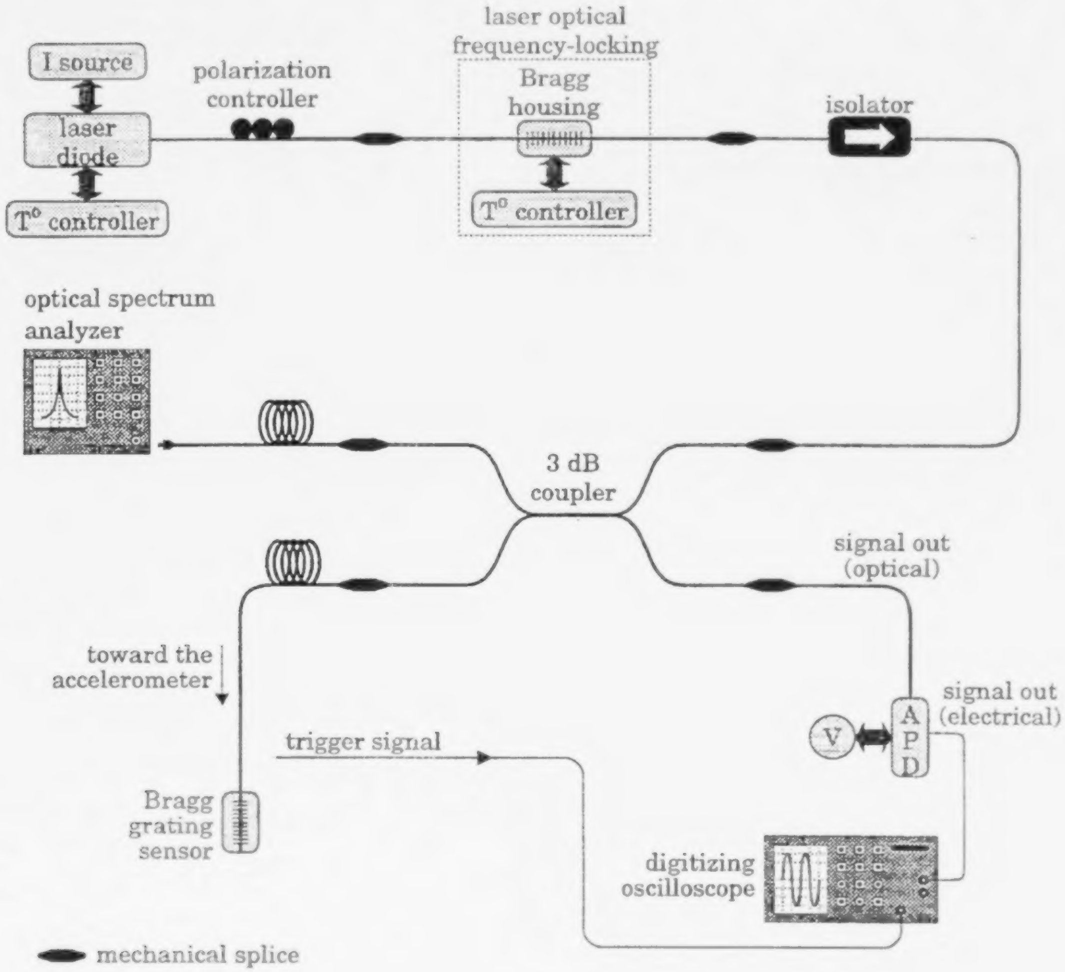
laser optical frequency-locking
I source
polarization controller
Bragg housing
isolator
laser diode
T° controller
T° controller
optical spectrum analyzer
3 dB coupler
signal out (optical)
toward the accelerometer
signal out (electrical)
V
A P D
trigger signal
Bragg grating sensor
digitizing oscilloscope
mechanical splice

Figure 2.15: The optical setup used for the detection of the grating spectral shift under acceleration.

detuned compared to the sensor grating. The detuning is simply a wavelength shift of the spectral response which can be achieved for example during fabrication of the grating or after fabrication by applying a small strain on it or by heating it. The detuning is required to position the emission wavelength of the laser in the quasi-linear region of the Bragg sinc-like response. The characteristics of this second grating can vary significantly between laser diodes depending on the laser mode content and the quality of the mirrors. Two sources were assembled each requiring slightly different Bragg characteristics. The advantages of this stabilization technique are that the grating is internal to the optical fiber which interconnects the source and the sensor and that any environmental change (e.g. temperature change)

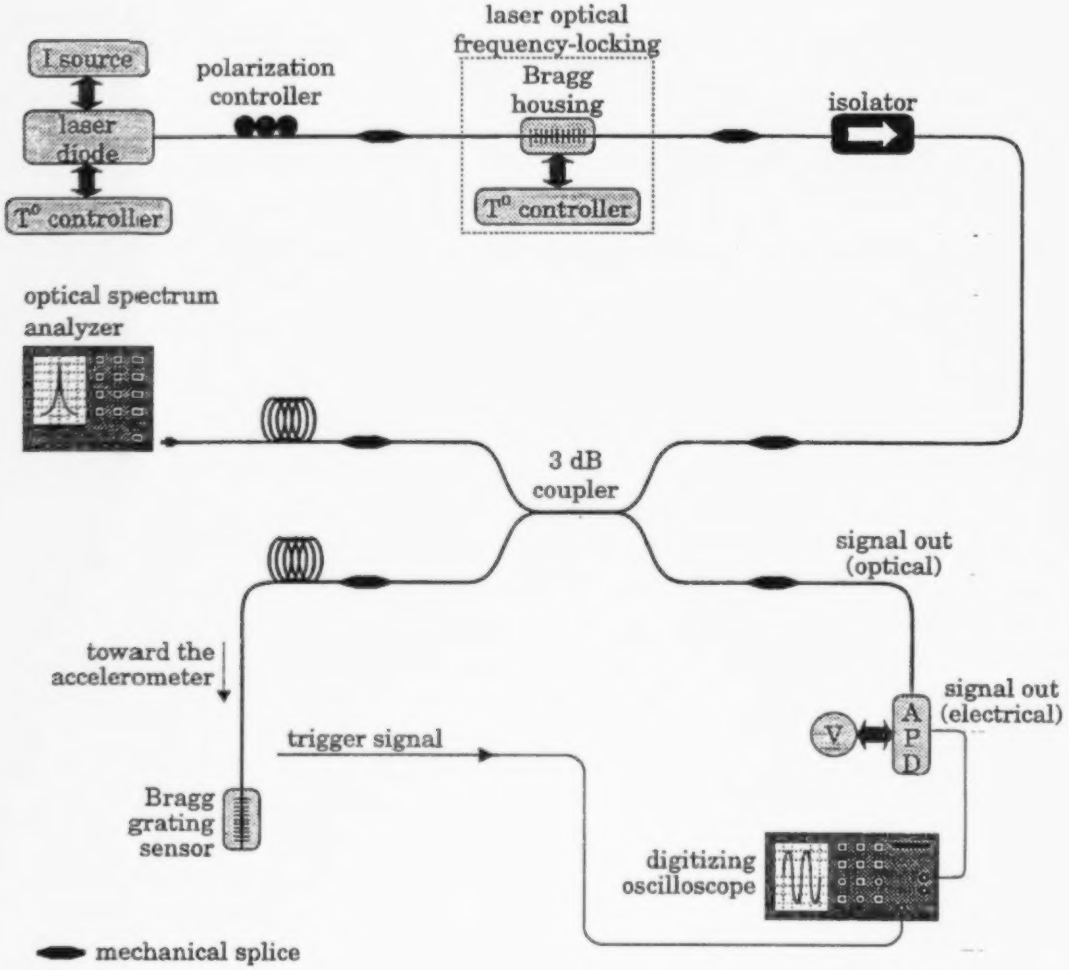
laser optical frequency-locking
I source
polarization controller
Bragg housing
isolator
laser diode
T° controller
T° controller
optical spectrum analyzer
3 dB coupler
signal out (optical)
toward the accelerometer
signal out (electrical)
V
A P D
trigger signal
Bragg grating sensor
digitizing oscilloscope
mechanical splice

Figure 2.15: The optical setup used for the detection of the grating spectral shift under acceleration.

detuned compared to the sensor grating. The detuning is simply a wavelength shift of the spectral response which can be achieved for example during fabrication of the grating or after fabrication by applying a small strain on it or by heating it. The detuning is required to position the emission wavelength of the laser in the quasi-linear region of the Bragg sinc-like response. The characteristics of this second grating can vary significantly between laser diodes depending on the laser mode content and the quality of the mirrors. Two sources were assembled each requiring slightly different Bragg characteristics. The advantages of this stabilization technique are that the grating is internal to the optical fiber which interconnects the source and the sensor and that any environmental change (e.g. temperature change) affects both gratings the same way thus maintaining correct relative position between the laser diode and the sensor spectral response.

To prevent any undesirable stray reflections which could perturb the laser diode an optical isolator is mounted in front of the coupler. The laser output power is optimized by using a polarization controller between the laser and the stabilization grating. An optical spectrum analyzer is used for monitoring the emission wavelength of the laser. The reflected light is detected with an avalanche photodiode (APD) and the electrical signal is sampled with a digitizing oscilloscope triggered by the passage of the ball in the accelerometer.

Figure 2.16 shows the response of the Bragg grating sensor used. The length of the grating is 1 mm and it was photoimprinted in Corning 800 Flexcore fiber. The fiber is singlemode at the wavelength of operation of 826 nm. The reflectivity of the grating was chosen at 65% and the FWHM was 0.3 nm.

Figure 2.17 shows the spectral response of the laser diode with proper relative positioning before acceleration. Under acceleration the sinc-like response shifts towards longer wavelengths and the light signal reflected back to the detector follows the slope towards the top of the response.

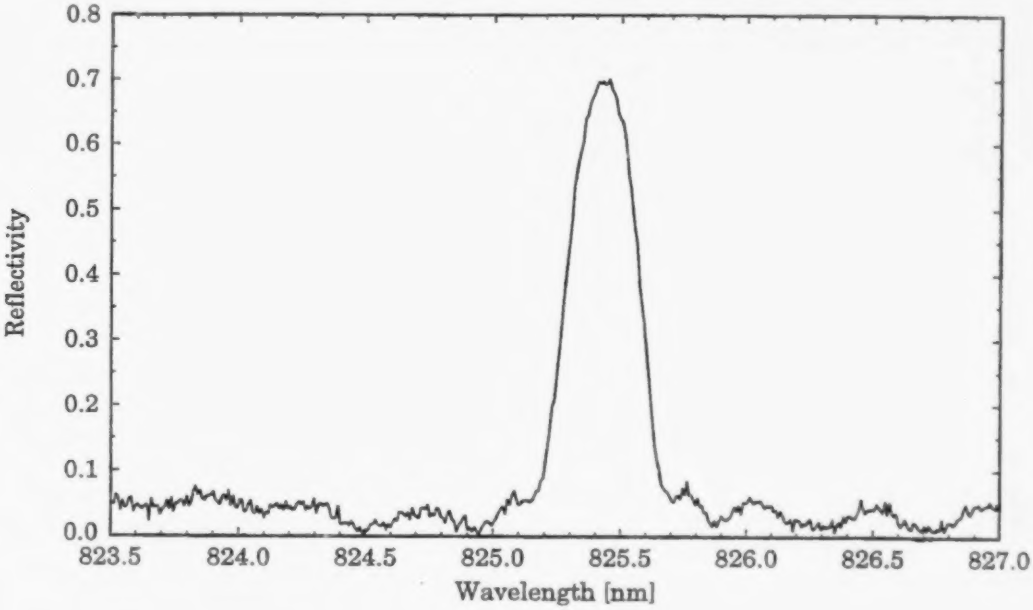

Figure 2.16: Spectrum of the sensor Bragg grating.

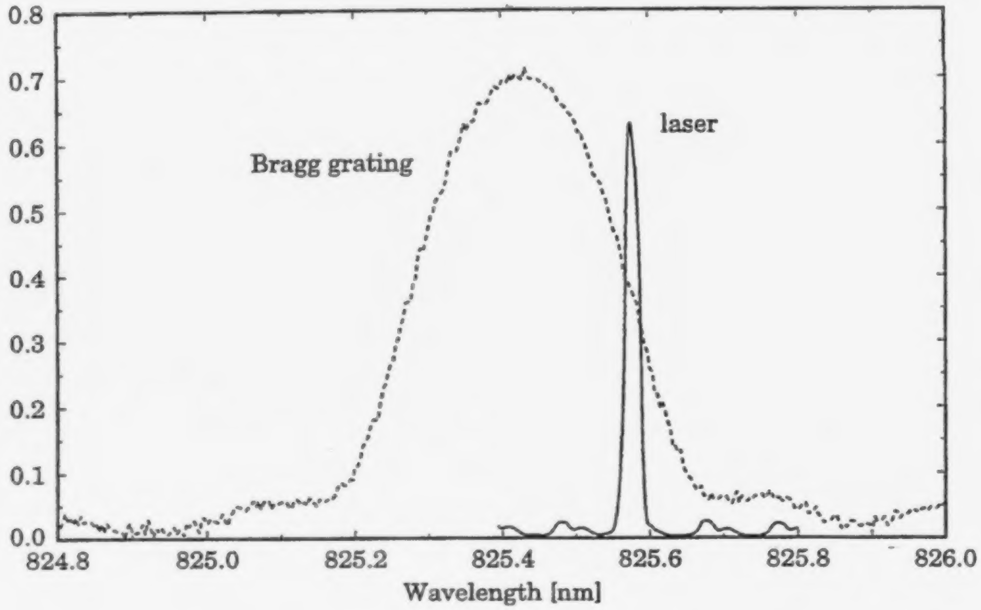

Figure 2.17: Spectrum of the laser diode frequency-locked by a stabilized Bragg grating.

2.3 Results

2.3.1 Cantilever measurements

The ball dropping apparatus was calibrated using a cantilever-type accelerometer from Endevco. Different accelerations can be generated using the ball-dropping setup by selecting various combinations of steel ball and anvil weights. The maximum acceleration developed is about 12 kg$_n$ and the duration of the pulses varied between about 50 μs to 125 μs. The shape of the acceleration pulses varied whether the anvil had a shock absorbing rubber pad or not.

The results for the 3 steel balls are plotted in figure 2.18 for the bare anvil and in figure 2.19 for the anvil with a rubber pad. The maximum voltage change at the peak of the highest acceleration is about 40 mV.

The signals shown in figures 2.18 and 2.19 were filtered with a 100 kHz low-pass filter to reduce the noise. See appendix D for more details.

2.3.2 Fiber-Bragg sensor responses

We have tested the fiber-Bragg sensor using the three balls but only with the bare anvil. The results are shown in figures 2.20 and 2.21. (see appendix E for original recordings). In

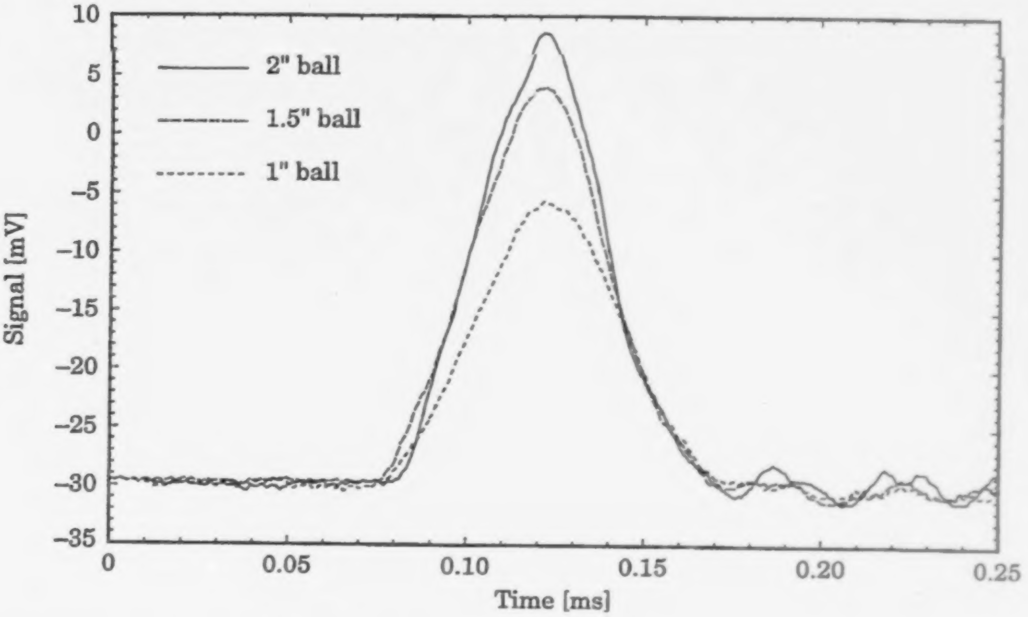

Figure 2.18: Signals measured using Endevco sensor for the 3 balls provided. The cantilever was attached to the bare anvil.

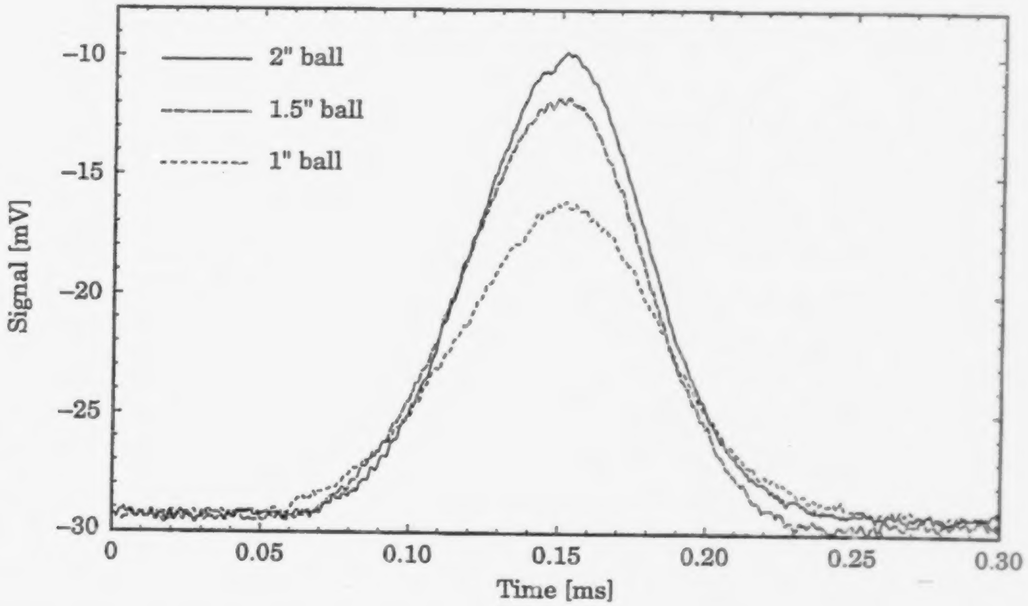

Figure 2.19: Signals measured using Endevco sensor for the 3 balls provided. The cantilever was attached to the anvil with a rubber pad on its top.

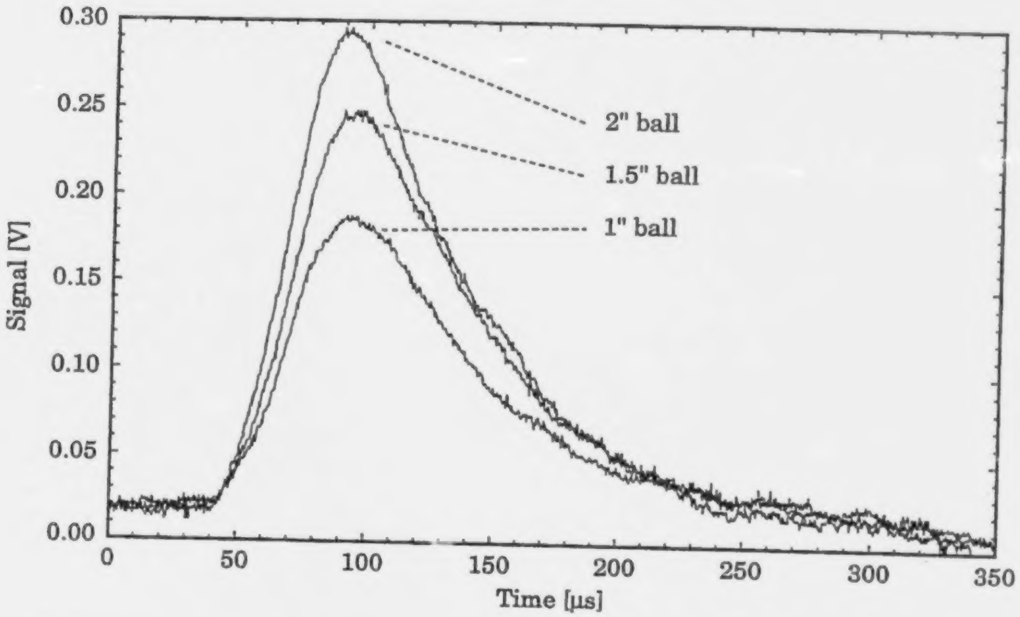

Figure 2.20: Bragg grating sensor responses for the 3 balls provided when the wavelength of the laser diode is on the long-wavelength side of the grating spectrum.

figure 2.20 the laser emission wavelength was located on the right side of the sensor spectral response, whereas in fig. 2.21 the laser was located on the left side of the sensor spectral response and close to the top of the response in order to get the maximum linear variation of the reflectivity under acceleration.

No signal processing was done on the responses shown in figures 2.20 and 2.21. The results agree well with the predictions of phase 1. No resonance frequency was detected confirming the presence of natural damping in the sensor.

2.3.3 Comparative analysis

The original objective of the comparative analysis was to conduct an extensive series of experiments using all possible combinations of balls and anvils and to characterize the performance of the fiber-Bragg sensor using the Endevco sensor for calibration. Unfortunately it was not possible to carry out this analysis because of reproducibility problems with the ball-dropping apparatus. These problems were especially serious when the 2" ball was used on the anvils not equipped with rubber pads. It appeared that whenever the ball was hitting the anvil off-center the resulting shock was reduced significantly.

Also the Endevco sensor proved difficult to use because its signal to noise ratio was quite

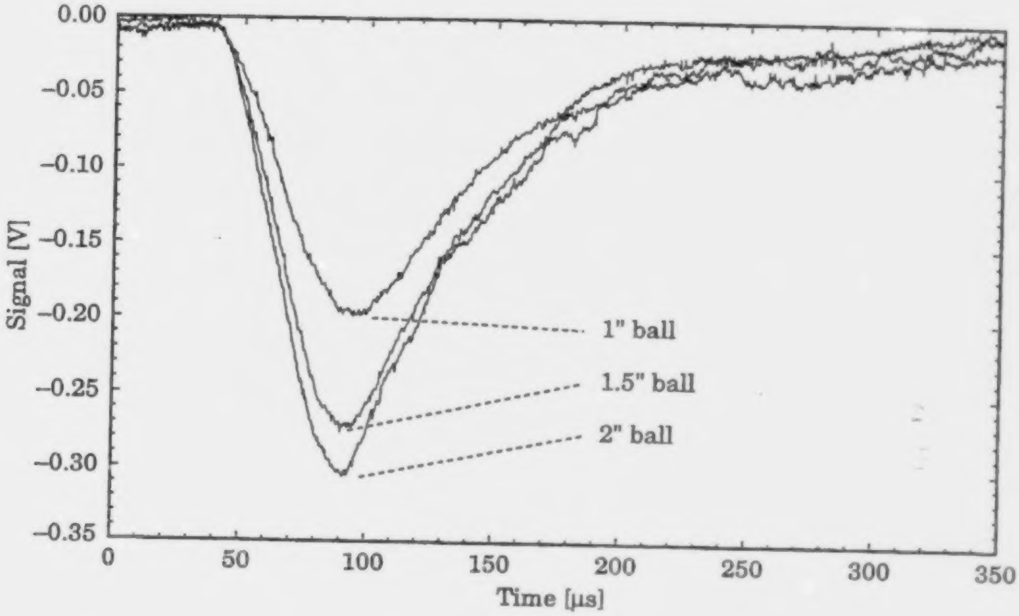

Figure 2.21: Bragg grating sensor responses for the 3 balls provided when the wavelength of the laser diode is on the short-wavelength side of the grating spectrum.

poor (see appendix D). It was impossible to use it without filtering the signal with a 100 kHz low-pass filter. This may have been caused by a noisy electro-magnetic environment at CRC. On the other hand the signal obtained from the fiber-Bragg sensor was of much higher amplitude (10 dB higher) even at only 10% of the maximum scale. Also the signal to noise ratio was significantly higher.

2.4 Analysis

Phase 2 of this feasibility study on a fiber-Bragg sensor consisted in the development of a real-time measurement technique, the development of a mount for the sensor and some preliminary tests at low g_n levels using a ball-dropping apparatus supplied by DREV. A measurement technique was successfully developed to obtain real time information on the value of the acceleration. The principal problem encountered with the measurement technique was the stabilization of the laser diode which required a level of control higher than expected.

A sensor mount was designed and a procedure to package the fiber-gratings was developed. The sensor was tested only up to a maximum of 10 kg_n using the ball-dropping apparatus.

Preliminary results obtained at low g_n levels were very promising. Unfortunately it was impossible to make a more complete experimental analysis using the ball-dropping apparatus because of reproducibility problems. In spite of this lack of experimental data the results show a dependence versus acceleration that appear to be linear even for signals below 10% of the full scale of the sensor. More significantly the results confirm the natural damping of the resonance frequency. Further tests at high acceleration levels will take place at DREV using the Hopkinson bar during phase 3.

Phase 3

Tests at high accelerations

Phase 2 of this feasibility study on a fiber-Bragg sensor consisted in the development of a real-time measurement technique and the development of a mount for the sensor. Preliminary results obtained at low g_n levels using a ball-dropping apparatus supplied by DREV were very promising. The results showed a linear dependence versus acceleration and confirmed the natural damping of the resonance frequency. However the sensor was tested only up to a maximum of 10 kg_n using the ball-dropping apparatus.

During phase 3, experiments were carried out at DREV using the Hopkinson bar in order to test the accelerometer at accelerations exceeding 100,000 g_n.

This section presents the modifications made to the experimental setup and to the sensor mount. The shape of various signals is studied. Linearity of the sensor response and cross-axial measurements are also presented.

3.1 The Hopkinson bar

The Hopkinson bar apparatus is described in figure 3.1. To summarize, pressurized air drives a projectile toward a collision with a long elastic bar. The impact creates a compression wave which travels down the bar. On the way toward the accelerometer which is mounted at the other end, the wave is measured by strain gages. When the wave reflects off the end of the bar, it imparts a known acceleration to the accelerometer. Digital analysis of the data from the strain gages and accelerometer provides the calibration.

Low pressure shop air is the source of energy for the pulse. The reservoir in which it is accumulated is the hollow structural steel beam which serves also as the frame of the system. Before each test, the plumbing union is opened, allowing a projectile to be installed

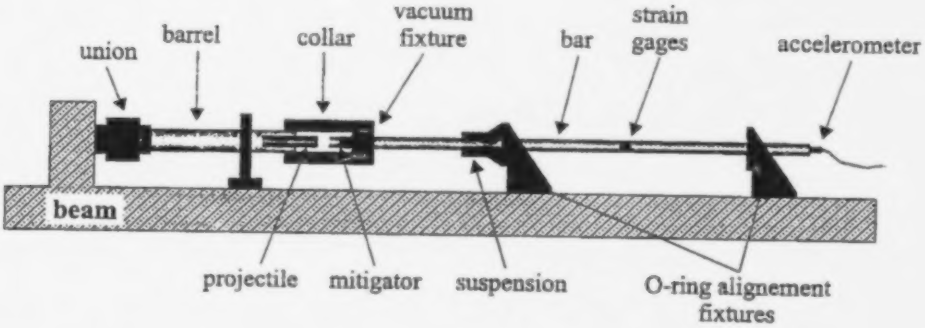

Figure 3.1: Schematic of the Hopkinson bar apparatus.

in the end of the barrel. After sliding the barrel back into position along alignment fixtures attached to the beam, a tracing paper diaphragm is clamped between the halves of the union. Air is then introduced into the beam, to be released into the barrel by the rupture of the diaphragm.

The Hopkinson bar is elastic to strains of one percent. The bar is held in by two O-rings which allow longitudinal slippage. Although ideally the bar should be free, displacement due to an impact is limited to a few centimeters by a suspension system comprised by epoxied, clamped shrink tubing and annular rubber bumpers.

A vacuum is used to hold a sacrificial piece of aluminium onto the end of the bar. This piece of aluminium serves as a shock mitigator. Acoustic couplant is applied to the interface to assure intimate contact.

Alignment between the barrel and the bar is maintained by a cylindrical collar which spans the gap between them, slipping over the barrel and the vacuum fixture. It also serves to shield the region of the impact.

The projectile is a cylindrical piece of hardened steel. It begins its flight near the diaphragm and is accelerated. During the collision, the aluminium mitigator plastically deforms and axially loads the bar, setting up a compression wave.

The compression wave is attenuated by a few percent as it passes by the suspension system and travels toward the accelerometer essentially unchanged thereafter. At the midpoint of the bar, two strain gages are mounted diametrically-opposed on the bar and are epoxied in place. An externally completed four-arm bridge is formed such that the gages are opposite active legs. With this configuration their response to longitudinal strains add, and their response to the bending strains cancel.

When the compression wave reaches the end of the bar, the accelerometer moves with a velocity directly proportional to the strain. The accelerometer is secured on the bar, so successive accelerations resulting from the compression wave bouncing back and forth along the bar can be recorded.

3.2 Modifications of experimental setup

Experiments carried out during phase 3 led to some modifications of the measurement setup and the sensor mount.

3.2.1 Sensor

During phase 2 experiments, the fiber was secured in the mount by squeezing a bare section of the fiber between the metal halves of the mount. This holding technique resulted in multiple fiber fractures at high acceleration levels. Fortunately, the problem was solved simply by squeezing the fiber with its protective jacket (without any glue to fix the fiber to the mount). The presence of the jacket doesn't appear to affect in any way the performance of the sensor. This technique reduces also the risks of breaking the fiber when assembling the sensor.

The configuration proposed in phase 2, a 1 mm-long Bragg grating at the base of a 10 mm-long free fiber was modified to accommodate the operation of the sensor in both compression and elongation. This became necessary because the sensor was attached to the Hopkinson bar and thus experienced positive and negative acceleration as the compression wave bounced back and forth along the bar. To stay in the linear region of the Bragg response, the free fiber was cut down to a length of 5-6 mm and the location of the Bragg grating was moved by about 2 mm away from the end of the holding groove, as shown in figure 3.2. Also the wavelength of the laser diode was shifted to the middle of the slope of the Bragg response to allow operation in both directions (positive and negative accelerations).

In order to realize the cross-axial measurements, a new mount was designed (see figure 3.3). The main objective was to prevent the fiber from exiting the mount at 90 degrees and then to prevent any fracture or any bending that could cause a signal variation.

Finally ceramic ferrules, like the ones used in standard fiber optic connectors, have been tested. The diameter of the hole in the middle of the ferrule is 127 microns, almost the same diameter as that of the fiber (125 microns). The lateral movement of the fiber is thus strongly restricted.

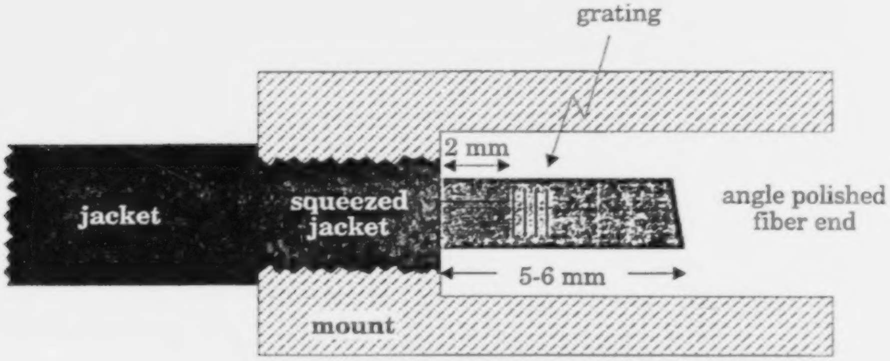
grating
2 mm
jacket
squeezed jacket
angle polished fiber end
5-6 mm
mount

Figure 3.2: Illustration of the sensor mount with the protective jacket now squeezed between both halves of the mount.

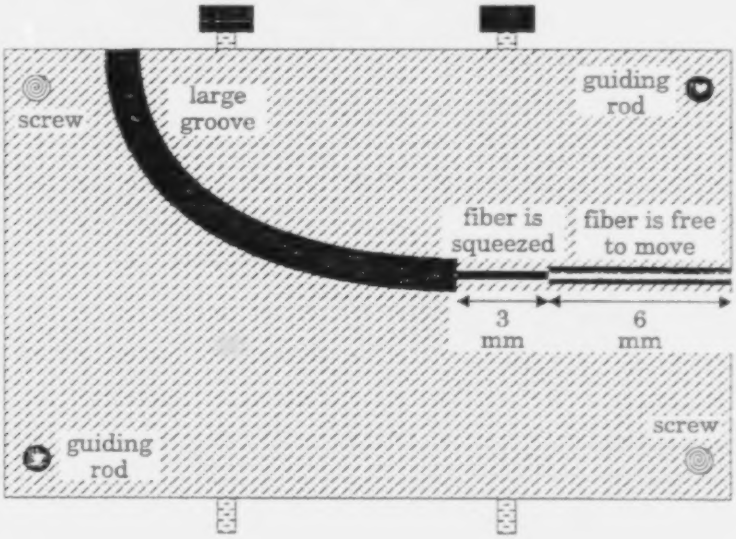
screw
large groove
guiding rod
fiber is squeezed
fiber is free to move
3 mm
6 mm
screw
guiding rod

Figure 3.3: Illustration of the sensor mount used for the cross-axial experiments.

3.2.2 Setup

During the measurements of phase 2, the bandwith of the detector was settled too small to follow the signals. This explains the asymmetry in the sensor response as shown in figures 2.20 and 2.21 of the phase 2. Actually, the 3-dB bandwith of the detector is shown in figure 3.4. A gain resistor of 100 kΩ was used for the measurements in phase 2, giving a bandwith of only 15 kHz. In order to get sufficient bandwith, the value of the resistor has to be reduced below 10 kΩ. Unfortunately the sensitivity of the photodetector is also reduced by a factor of 10. This problem was overcome by using a more powerful semiconductor laser.

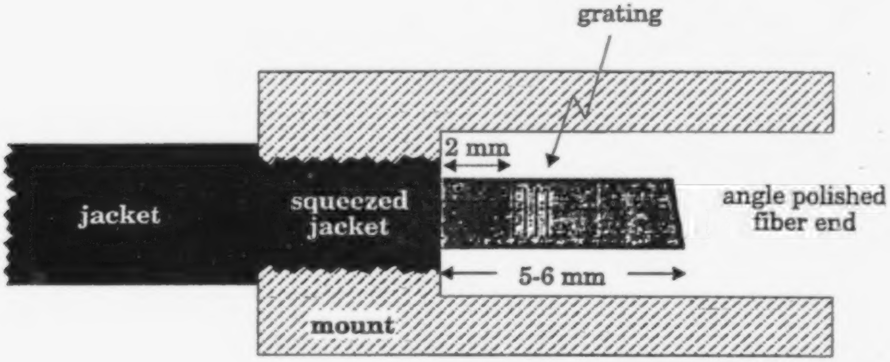
grating
2 mm
jacket
squeezed jacket
angle polished fiber end
5-6 mm
mount

Figure 3.2: Illustration of the sensor mount with the protective jacket now squeezed between both halves of the mount.

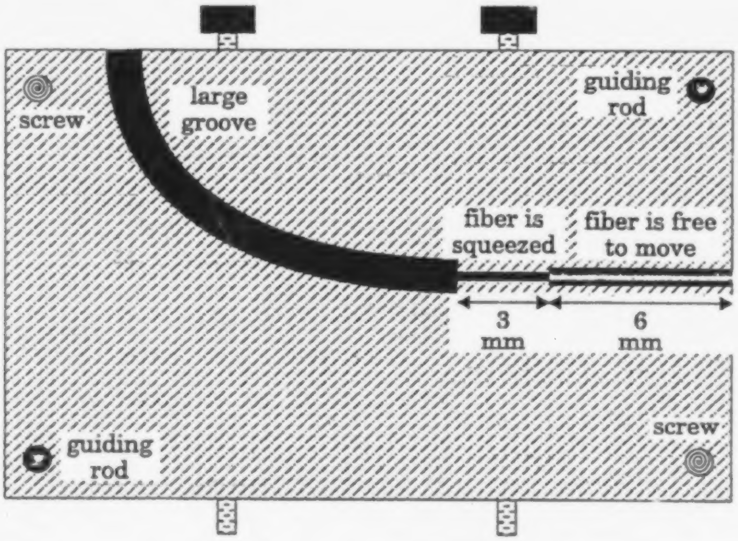
screw
large groove
guiding rod
fiber is squeezed
fiber is free to move
3 mm
6 mm
guiding rod
screw

Figure 3.3: Illustration of the sensor mount used for the cross-axial experiments.

3.2.2 Setup

During the measurements of phase 2, the bandwith of the detector was settled too small to follow the signals. This explains the asymmetry in the sensor response as shown in figures 2.20 and 2.21 of the phase 2. Actually, the 3-dB bandwith of the detector is shown in figure 3.4. A gain resistor of 100 kΩ was used for the measurements in phase 2, giving a bandwith of only 15 kHz. In order to get sufficient bandwith, the value of the resistor has to be reduced below 10 kΩ. Unfortunately the sensitivity of the photodetector is also reduced by a factor of 10. This problem was overcome by using a more powerful semiconductor laser.

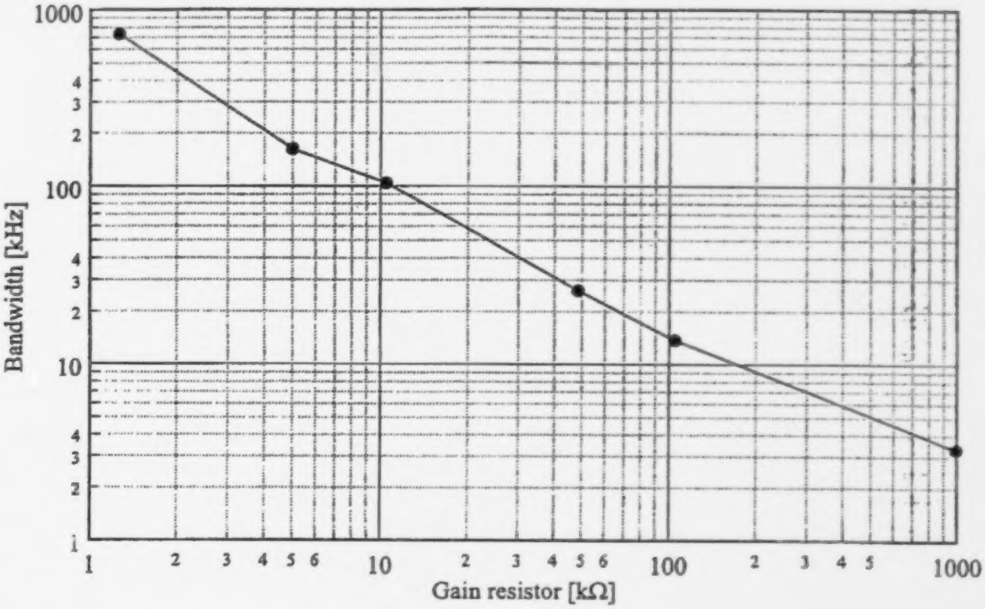

Figure 3.4: Relation of the detector bandwith versus the resistor gain value.

The new single mode laser couples up to 30 mW in the fiber (the specifications are included in appendix H). Also, the thermoelectric unit used to tune and lock the wavelength of the laser diode was replaced by a stretching device which strains the fiber Bragg grating.

3.3 Results and analysis

3.3.1 Visits summary

During phase 3, 4 visits were made to DREV. During the first visit, many fiber fractures have been experienced. This problem was fixed by squeezing the jacket in the mount. During the second visit, the detector bandwith was not sufficiently large to give symmetrical responses. Thus the resistor gain was reduced. During the third visit, the mount used to make the cross-axial measurements was too heavy, loosing or breaking the screws securing the sensor to the bar, even at low accelerations. We have experienced the same problem during the fourth visit even with the new cross-axial mount. Also the Hopkinson bar was not operating very well, seeming to be somewhat uncalibrated.

A summary of the tests carried out during the last 3 visits is included in appendix F.

3.3.2 Signals

The strain gages provide a signal that is used to calculate the acceleration as shown in figure 3.5. The acceleration signal (fig. 3.5b) is the derivative of the strain signal (fig. 3.5a). The corresponding Bragg grating sensor signal is included in fig. 3.5c.

The Bragg grating sensor follows the rapid features of the acceleration signal quite well. The sensor signal is delayed by about 130 μs from the acceleration signal, corresponding to the propagation time of the compression wave travelling from the strain gages to the end of the bar. Also, because the strain gages are placed in the middle of the bar, they experience twice as many acceleration pulses than a sensor placed at the end of the bar.

A glitch sometimes appears in the strain signal which brings about a much stronger glitch once the derivative of the strain is done to get the acceleration signal.

In figure 3.6 the acceleration sensor signal recorded for multiple reflection of the compression wave is plotted. We see the attenuation of the compression wave as it travels back and forth along the bar. Also we observe that the noise level (mechanical resonances of the mount) between each pulse increases with time, possibly because the free fiber undergoes a lateral movement within the mount.

3.3.3 Sensor responses

Typical responses of the Bragg sensor are shown in figures 3.7 and 3.8 for acceleration levels of 67 and 137 kg_n respectively. The latter acceleration is by far higher than the target specifications and proves the robustness of the Bragg sensor. In these figures, the time axis has been shifted for curve matching between the acceleration signal (dots) and the sensor signal (thin line).

For the case in figure 3.7 (maximum acceleration of 67 kg_n), we observe a close-to-perfect fit in the positive part between the acceleration curve and the sensor curve. In the negative part, the sensor follows the features of the acceleration but the signal levels are not equal. The explanation for this discrepancy is that the laser wavelength was located to optimize the linearity regime of the sensor in the positive pulse only. So the sensor response in the negative part is not linear but the correspondence is quite good.

For the very high acceleration case shown in figure 3.8 (maximum acceleration of 137 kg_n), the positive part of the sensor signal again fits to the acceleration signal well. Only the positive part of the signal is significant because the laser wavelength was located near the bottom of the Bragg response in order to get maximum linearity on the positive excursion at 137 kg_n. The negative excursion of the signal corresponding to the compression of the Bragg grating is then distorted. The noise mostly present between acceleration pulses will

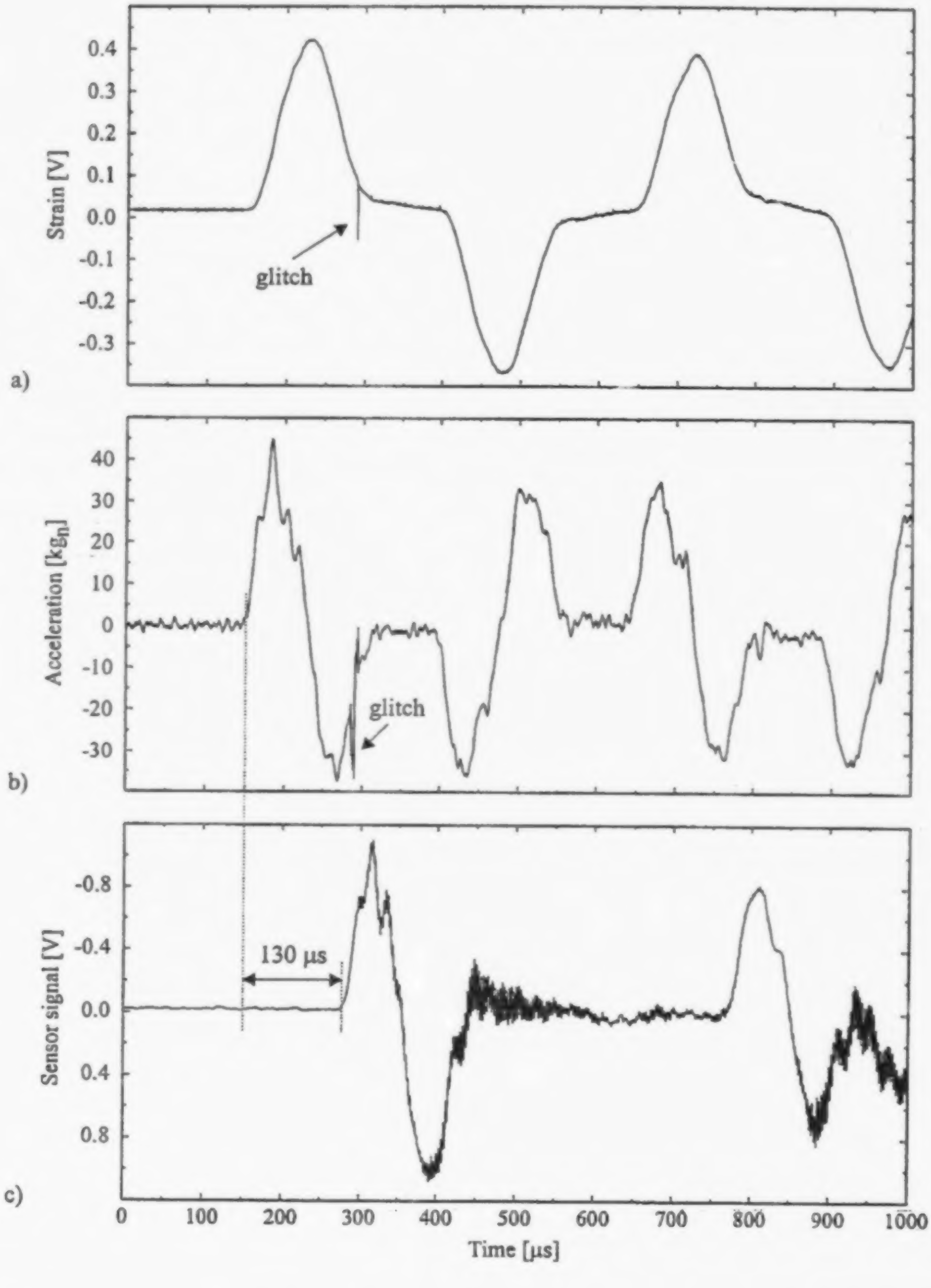

Figure 3.5: Comparison of the Bragg grating sensor response with the acceleration signal (derivative of the strain); a) strain, b) acceleration, c) sensor signal.

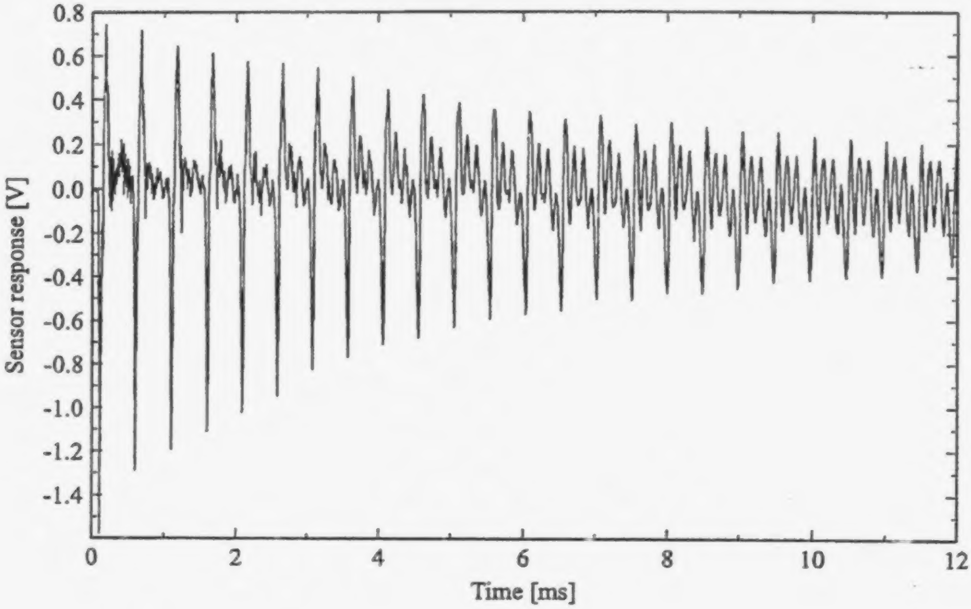

Figure 3.6: Sensor response showing the successive reflections of the compression wave.

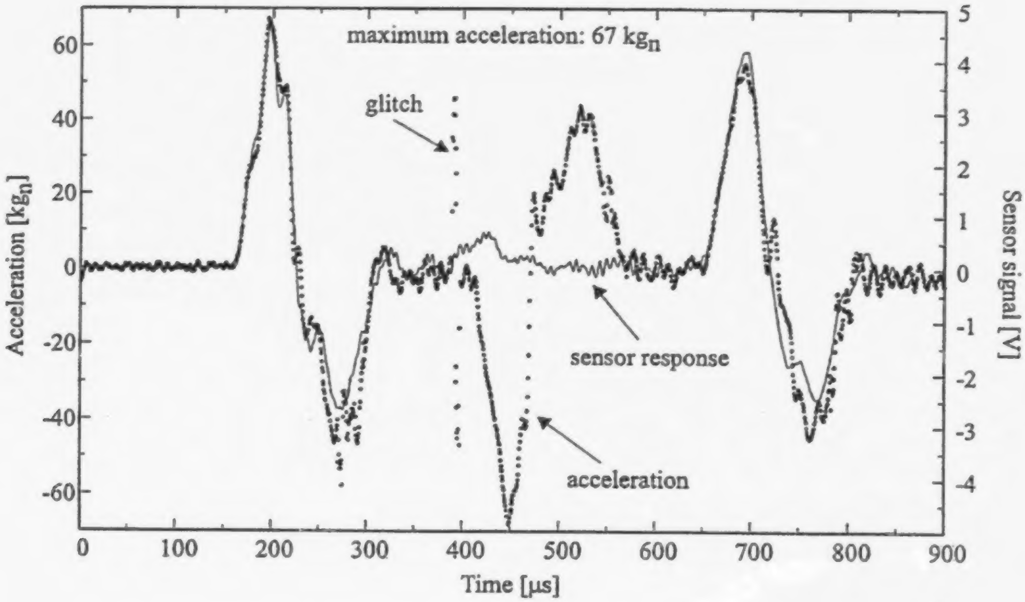

Figure 3.7: Typical response of the Bragg sensor at an acceleration of 67 kg$_n$. The acceleration (dots) and sensor (thin line) responses are plotted.

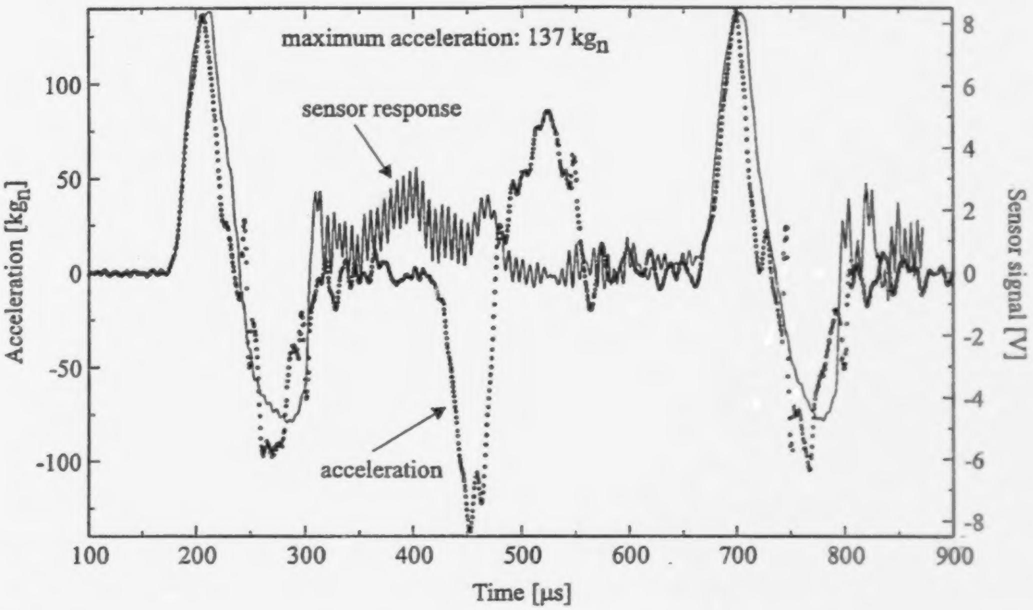

Figure 3.8: Typical response of the Bragg sensor at an acceleration of 137 kg$_n$. The acceleration (dots) and sensor (thin line) responses are plotted.

be discussed in section 3.3.6.

Actually, the sensor has been tested in both directions, either in elongation or in compression, without any discrepancy between each case.

3.3.4 Linearity

The linearity analysis is divided in two parts, one quantitative and one qualitative.

First, the linearity of the sensor between 0 and 170 kg$_n$ was measured and evaluated, as shown in figure 3.9. 3 series of measurements were made and only the peak sensor signal versus the peak acceleration measured for a specific test is plotted. Then each symbol is attached to a specific series and the corresponding line is a least-square fit.

For the measurement series 1 and 3, the laser wavelength was located on the right side of the Bragg response thus producing positive slopes. The sensitivity of the two sensors is different and the resulting slopes are 0.0217 V/kg$_n$ and 0.0101 V/kg$_n$. Actually, the sensor fiber in the series 3 was shorter and the Bragg grating was shifted by 2 mm, explaining the reduced sensitivity. For the series 2, the laser wavelength was located on the left side of the Bragg response thus producing a negative slope of -0.0536 V/kg$_n$.

The sensor looks to be quite linear and remains so up to 170 kg$_n$ which was the maximum

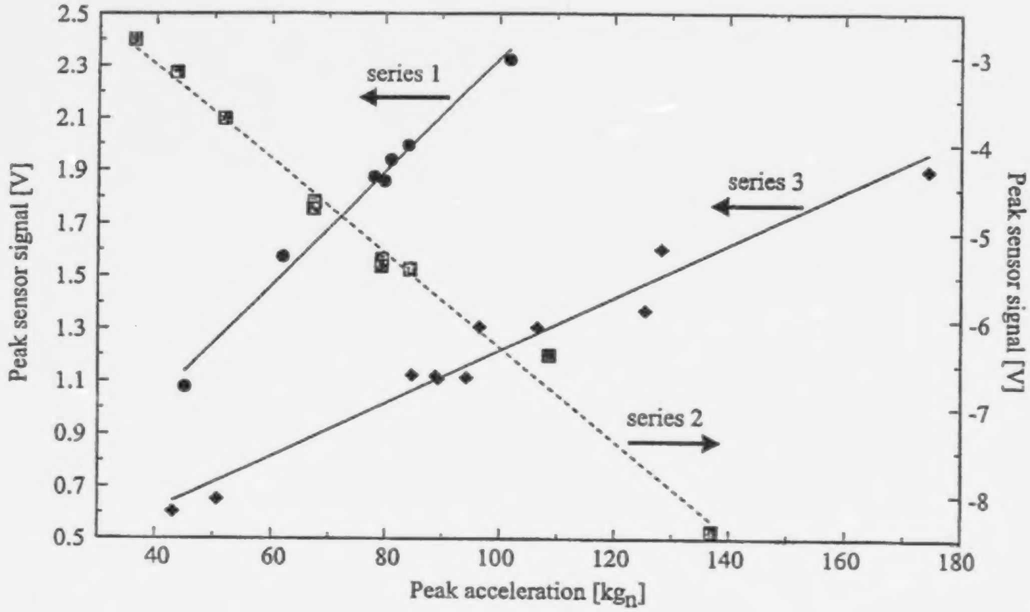

Figure 3.9: Linearity tests made using 3 different sensors.

acceleration generated by the Hopkinson bar setup.

Using only the maximum value of the acceleration from each test may not be the most accurate way to evaluate the sensor linearity. A second technique to evaluate the linearity consists simply in comparing the Bragg sensor signal to the derivative of the strain versus time for a given test, as shown in figure 3.10. The signals fit very well, even in figure 3.10b where many features are present. This qualitative representation shows that the sensor follows linearly the acceleration pulse.

3.3.5 Cross-axial measurements

The cross-axial sensitivity of the Bragg sensor was measured using the new mount as described in section 3.2.1. The results at an acceleration level of 85 kg$_n$ are presented in figure 3.11a where a longitudinal measurement is plotted for comparison. In figure 3.11b, the same cross-axial signal is expanded for better inspection.

These results show clearly the extremely low cross-axial sensitivity of the Bragg grating sensor. The presence of noise observed in figure 3.11b will be discussed in the next section.

On the other hand, the size of the hole around the free fiber is very important for low cross-axial sensitivity. The cross-axial mount used for the measurement had a hole diameter of 150 μm. For larger hole diameters the fiber is free to bend and shows a non-zero acceleration

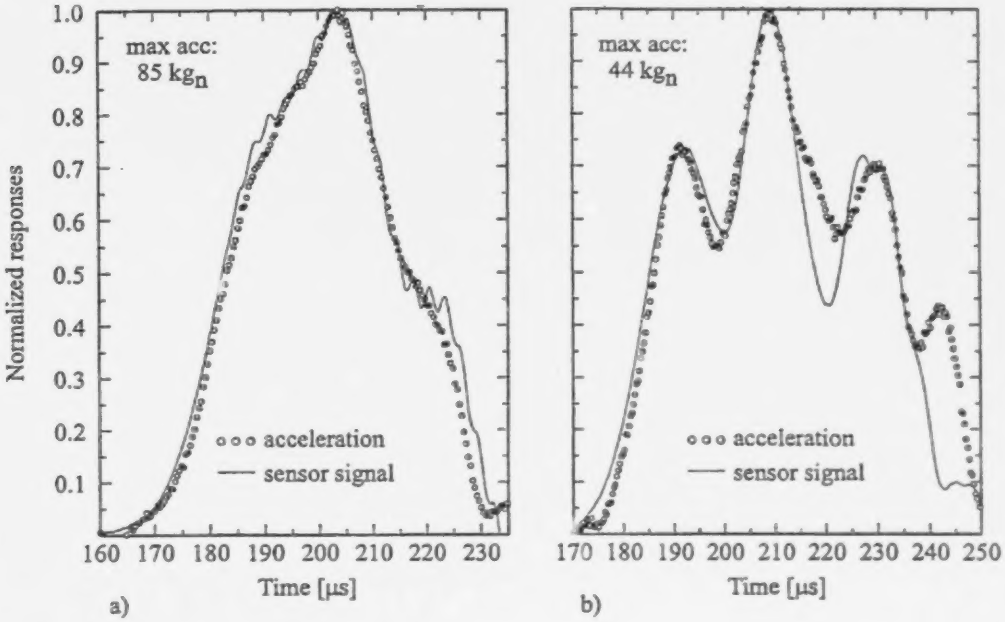

Figure 3.10: Comparison between the first acceleration pulse and the resulting sensor signal.

3.3.6 Noise analysis

The acceleration signals observed during the acceleration pulses are free of noise and follow the derivative of the strain quite well. But we have observed the presence of mechanical resonances which occur between acceleration pulses. This noise observed between pulses changes in amplitude and frequency depending on the mount used.

3.3.6.1 Aluminium mount

During new measurements made with the column, we have observed that the high frequency component of the noise (> 200 kHz) is related to the guiding rods used to align both halves of the aluminium mount. Figure 3.12 shows the effect of the rods on the sensor response. These rods are somewhat free to move and can enter into resonances. This effect was strongly dependent on the mount used. The remaining noise in figure 3.12b could have been introduced by the screws.

Also, 2 different mounts, each with a different hole size, have been tested and typical results are shown in figure 3.13. In the first case (fig. 3.13a), a mount with a 500 μm hole size was used and a strong signal amplitude variation was observed between the pulses (as previously mentioned, the high frequency component is related to the guiding rods). In

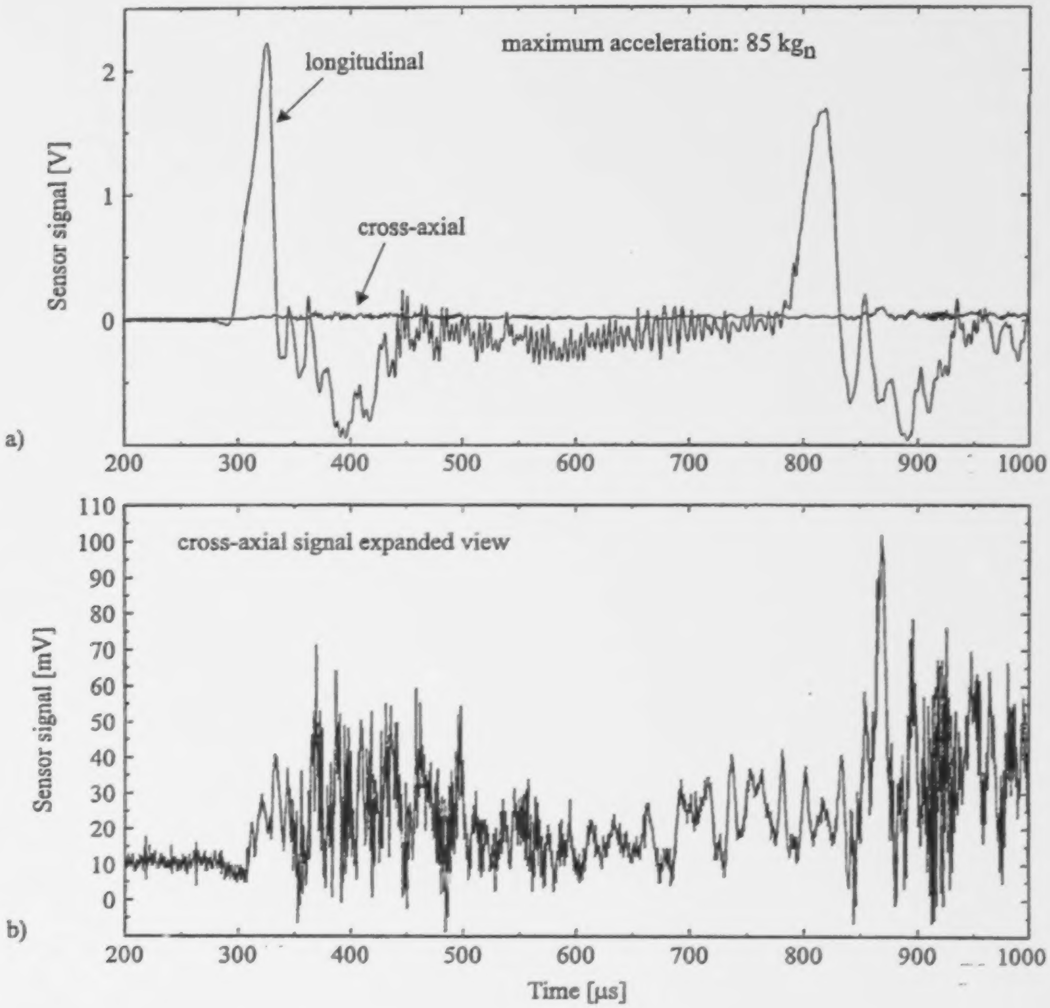

Figure 3.11: Cross-axial measurement at an acceleration level of 85 kg$_n$. In a), a longitudinal measurement is plotted for comparison.

this case the 125 μm-diameter fiber has a lot of room to move and undergoes strong lateral oscillations.

In fig. 3.13b, a mount with a hole size of 150 μm gives much better results. The fiber lateral oscillations are greatly reduced and they become more important only after many pulses, as shown in figure 3.13c.

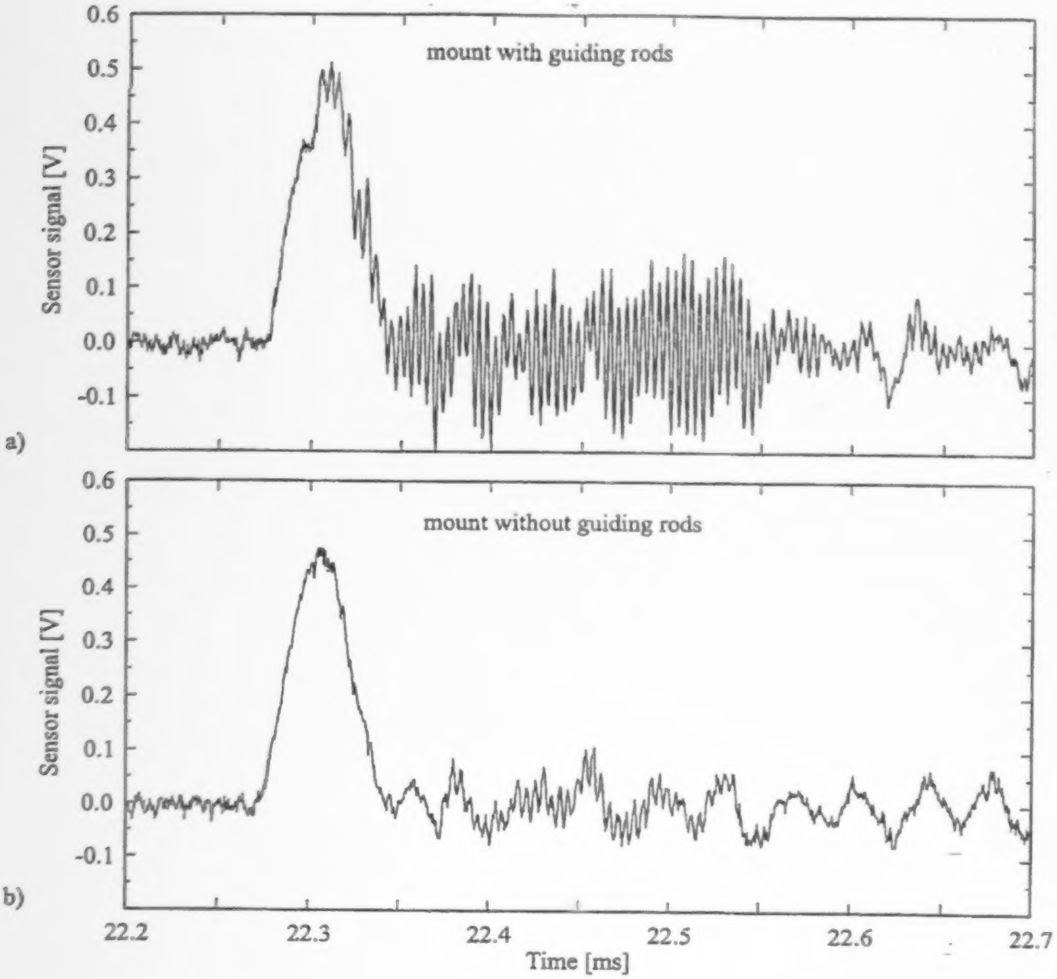

Figure 3.12: Effect on the sensor response when an aluminium mount is used a) with and b) without guiding rods.

3.3.6.2 Ceramic ferrule

A ceramic ferrule used in commercial optical connectors was inserted in a modified mount. The ferrule has a hole diameter of 127 μm compared to the fiber diameter of 125 μm. A typical result is shown in figure 3.14. The frequency of the oscillations is 37 kHz and a small pulse is observed prior to the start of the acceleration pulse (inside the dotted circle around 100 μs). Actually the ferrule is more compressible than expected and when the compression wave travels through the ceramic, the fiber experiences some friction with the ferrule. This explains why the fiber is compressed before elongated thus creating the small pulse. The low

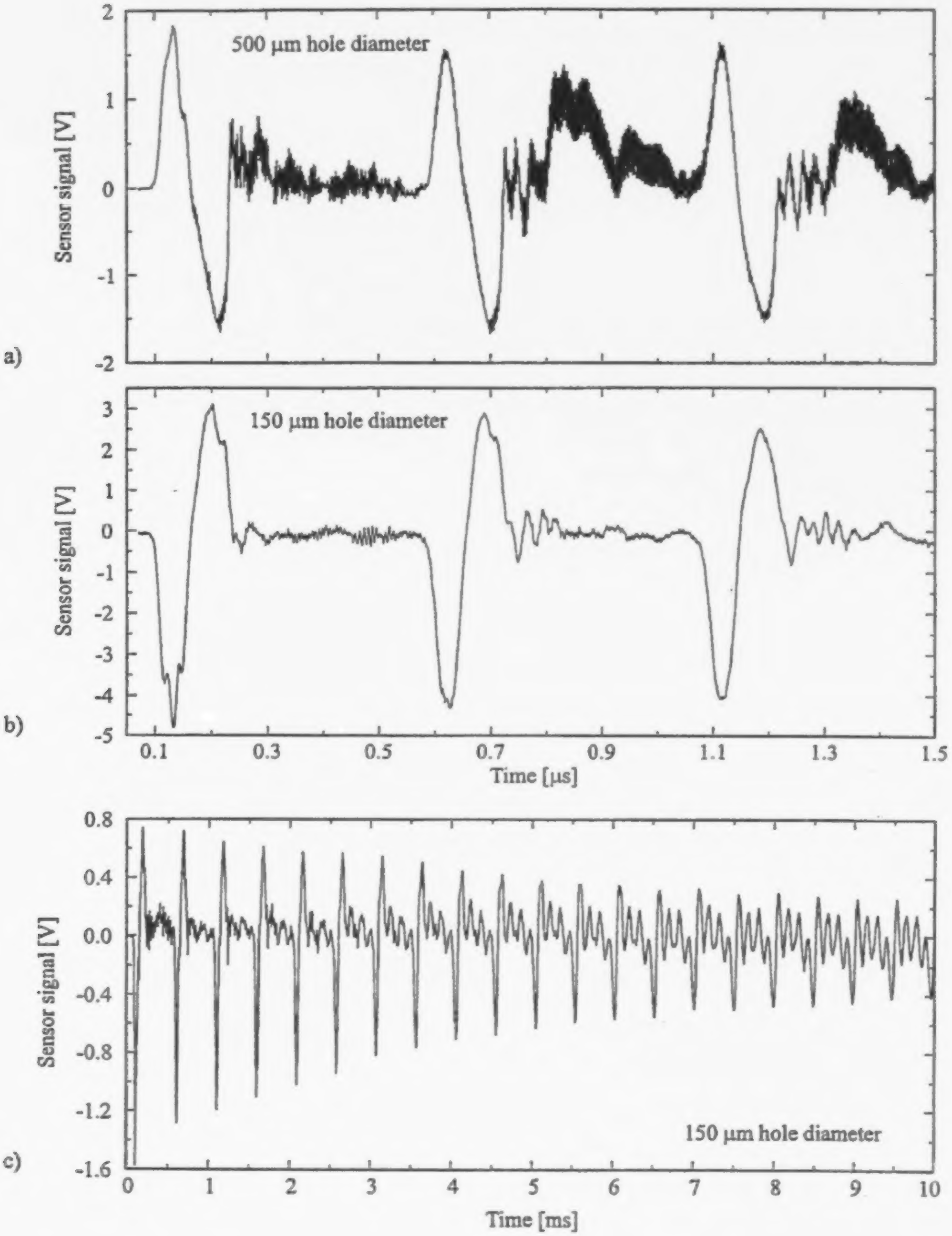

Figure 3.13: Effect on the sensor response for two mounts with different hole diameter.

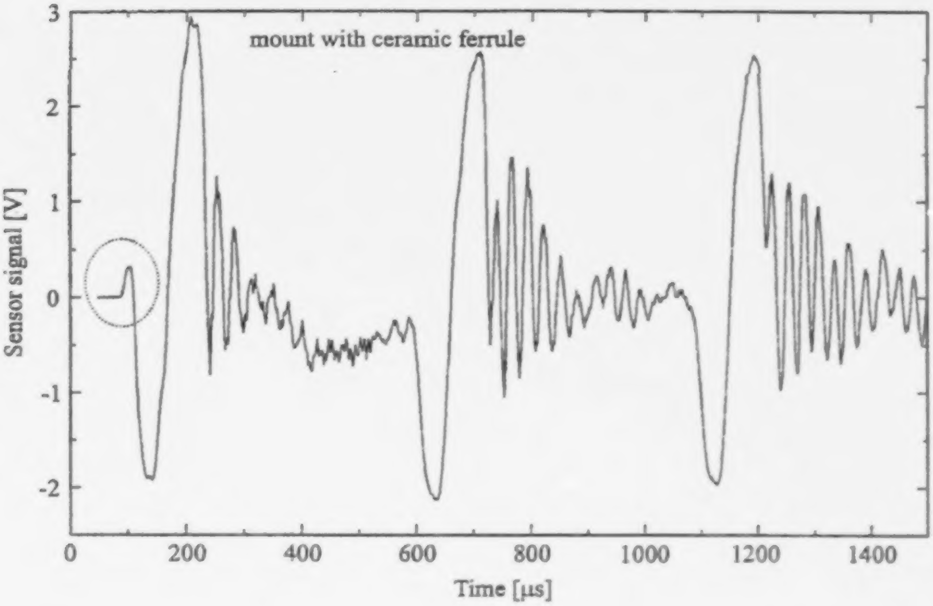

Figure 3.14: Longitudinal measurement of the sensor set in a ceramic ferrule inserted in a modified mount. The dotted circle at around 100 μs draws attention to a special feature associated only to the ceramic ferrule.

frequency variation is created by the resonance of the ferrule.

The cross-axial measurement made with the ceramic ferrule, shown in figure 3.15, demonstrates that the ceramic ferrule is compressible. Even at 90 degrees the fiber experienced a strong compression wave. This means that the 127 μm hole diameter is too small relative to the 125 μm diameter of the fiber. The ceramic ferrule could be a good candidate because of the clean edge of the hole but the size of the hole should be larger.

3.4 Analysis

The tests carried out at high acceleration levels using the Hopkinson bar confirm the potential of Bragg gratings for acceleration sensing. The fiber sensor has shown linearity with acceleration and has demonstrated its robustness by resisting to acceleration levels up to 170 kg_n. Also the sensor has shown very low cross-axial sensitivity.

Recent developments concerning the noise reduction are very promising. Further improvements to the sensor mount is now necessary.

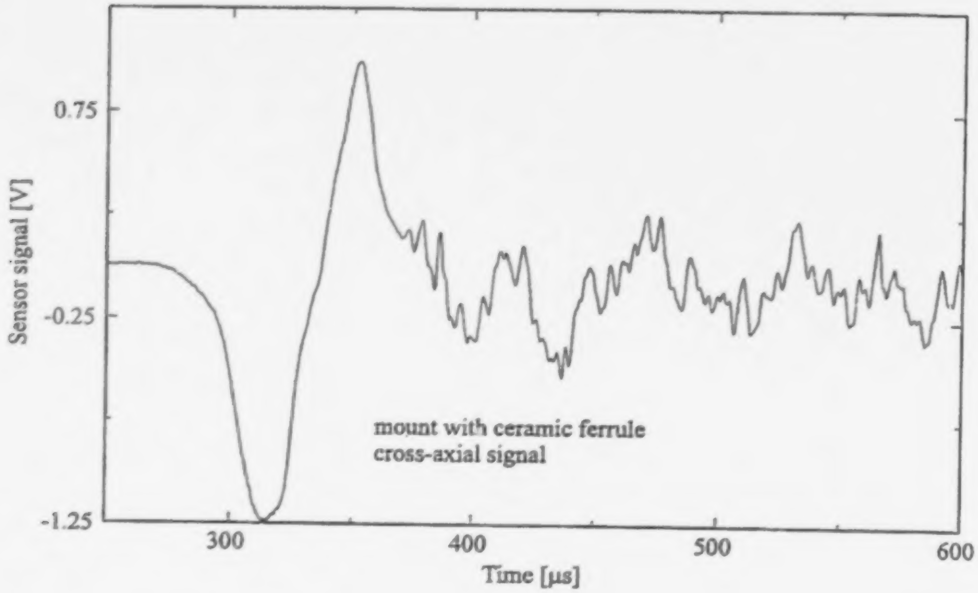

Figure 3.15: Cross-axial measurement made with the ceramic ferrule showing a strong sensor signal.

Phase 4

Alternative detection scheme

During phase 3, the feasibility of using a fiber Bragg grating as an acceleration sensor has been demonstrated. The fiber showed robustness and linear response to acceleration up to 170 kg_n and the detection setup based on sensing the Bragg response shift using a narrowband laser diode gave good signal-to-noise ratio and low cross-axial sensitivity.

Once integrated in a real system (e.g. missile), the laser diode setup could suffer from temperature changes. Also the laser diode requires optical feedback isolation. In order to circumvent these problems, a new insensitive and less bulky setup using an LED instead of a laser diode is proposed.

This section presents the theoretical and experimental performances of the new detection scheme. Sensitivity, linearity and signal-to-noise ratio are investigated.

4.1 New configuration

4.1.1 Scheme proposed

The schematic setup of the laser diode setup described in the previous phase is shown in figure 4.1. A laser diode is used to interrogate the local reflectivity of a Bragg grating sensor. The reflected light is measured by a photodetector. The laser diode spectrum is very narrowband (10^{-4} nm) compared to the Bragg grating spectrum (~1 nm). When strained under acceleration the grating spectrum shifts in wavelength. The laser wavelength interrogating the grating is fixed so the light signal reflected back to the detector varies as shown in figure 4.2.

The new configuration is shown in figure 4.3. First, the laser diode and the isolator are replaced by an LED. Then, a second Bragg grating, used as a reference, is added just in

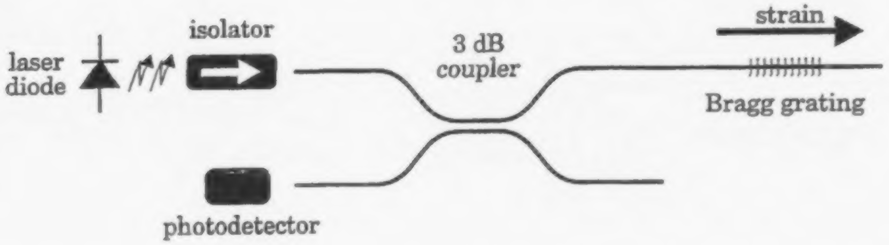
laser
diode
isolator
3 dB
coupler
strain
Bragg grating
photodetector

Figure 4.1: The laser detection scheme senses the level of light back-reflected by a sensor Bragg grating.

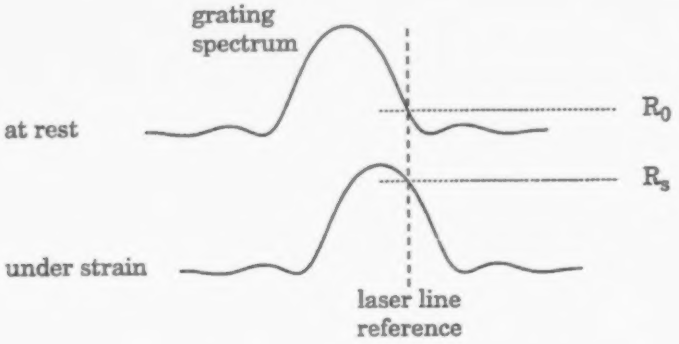
grating
spectrum
at rest
R_0
R_s
under strain
laser line
reference

Figure 4.2: The principle of the detection is based on a change in the level of light back-reflected to the photodiode.

front of the photodetector. This grating is not under the influence of the high acceleration, ensuring that its spectral response will not change.

As shown in figure 4.4, the LED spectrum is very wide (tens of nanometers) compared to the Bragg sensor response (~1 nm). The new scheme is simpler because there is no need to isolate the source as in the previous setup. Also temperature changes on the LED

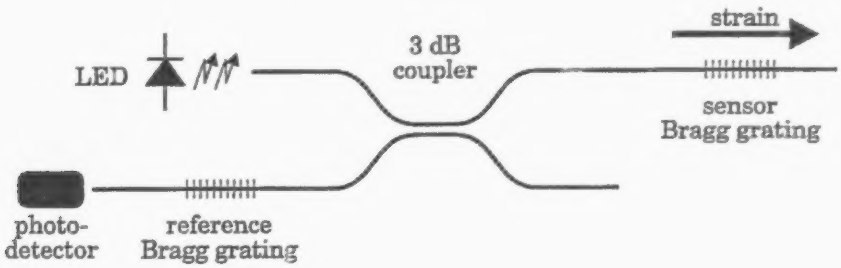
LED
3 dB
coupler
strain
sensor
Bragg grating
photo-
detector
reference
Bragg grating

Figure 4.3: The new detection scheme uses an LED instead of a laser-diode and a second Bragg grating is put in front of the photodetector.

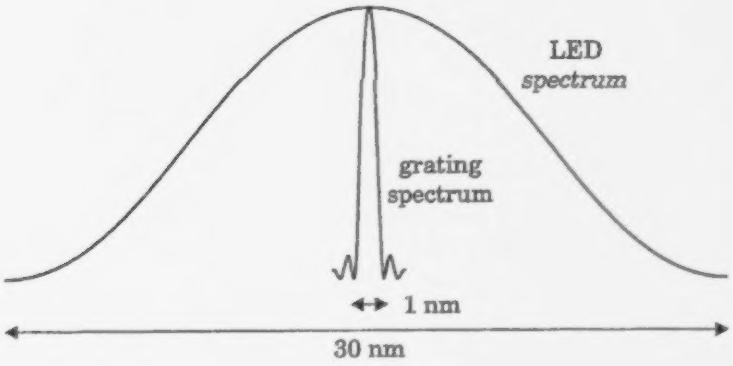

Figure 4.4: The LED spectrum is very wide compared to the Bragg spectrum.

are now irrelevant because of the wide spectral response of the LED which allows for a wide operating margin (see figure 4.4). More significantly, the sensor and reference gratings responses will shift the same way under temperature changes, making this new scheme temperature insensitive.

4.1.2 Principle

The basic principle of the new detection scheme is based on the spectral convolution between the spectra of the sensor and the reference gratings. For the configuration shown in figure 4.3, the convolution is expressed as

$$S(\omega) * (1 - R(\omega)) = \int_{-\infty}^{\infty} S(\omega)(1 - R(\omega - \tau))d\tau \tag{4.1}$$

where $S(\omega)$ and $R(\omega)$ are the spectral responses in the Fourier domain of the sensor and the reference gratings respectively. In that case, $S(\omega)$ is the reflection spectrum of the sensing Bragg grating and $1 - R(\omega)$ represents the transmission spectrum of the reference grating.

Also we can modify slightly the configuration by placing the photodetector at the end of the unused arm of the 3 dB coupler, as shown in figure 4.5. In this case, the convolution is expressed as

$$S(\omega) * R(\omega) = \int_{-\infty}^{\infty} S(\omega)R(\omega - \tau)d\tau \tag{4.2}$$

So, in the first configuration, the convolution is dependent on the transmission characteristic of the reference grating whereas in the second configuration it is dependent on the reflection characteristic.

Now let us suppose that the reflection spectra of the reference and the sensor gratings are identical and that the second configuration for the detection scheme $(S(\omega) \cdot R(\omega))$ is

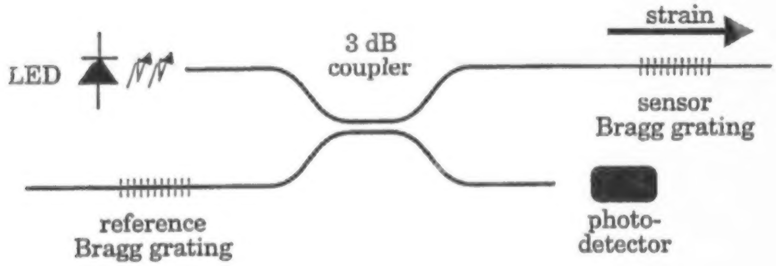

Figure 4.5: A second configuration is possible by placing the photodetector at the end of the unused coupler arm.

chosen. When both gratings are at the same center frequency, the same level of light at each frequency component will be back-reflected by both gratings giving a maximum signal as shown in fig. 4.6a. When they are slightly offset, some of the high reflectivity frequency components of the sensor fall outside the response of the reference grating, producing a lower signal (fig. 4.6b). Finally, when they are completely offset, none of the reflected light of the sensor grating will be reflected by the reference grating, giving no detectable signal (fig. 4.6c). If the two spectra have the same shape and they are perfectly aligned the spectral product will be maximum whereas if they are mutually exclusive, the spectral product will be nulled. Between these two extremes, the convolution is linear within a specific range as determined in the next section.

To use this new detection scheme as an acceleration sensor, we have to measure in real-time the photodetector signal corresponding to the product of both spectra during acceleration. Also to ensure that both gratings reflect the same amount of light, a wideband optical source like an LED is required as long as its spectrum is flat and free of ripples.

Finally, if the measurements are made in DC, the second configuration shows a lower S/N ratio because the incident laser light is added to the sensing signal. There is also possibility of saturation if too much light from the LED hits the photodetector. The first configuration eliminates the DC component produced by the direct LED light hitting the detector. Also the detected signal is 3 dB higher because the detected signal goes through the coupler one less time (2 passes versus 3 passes).

4.2 Theoretical results

Some calculations were performed to verify the linearity of the LED detection scheme. We tested the two configurations ($S(\omega) \cdot (1 - R(\omega))$ and $S(\omega) \cdot R(\omega)$) described in the previous section and compared for different Bragg spectral responses. We consider the case of uniform

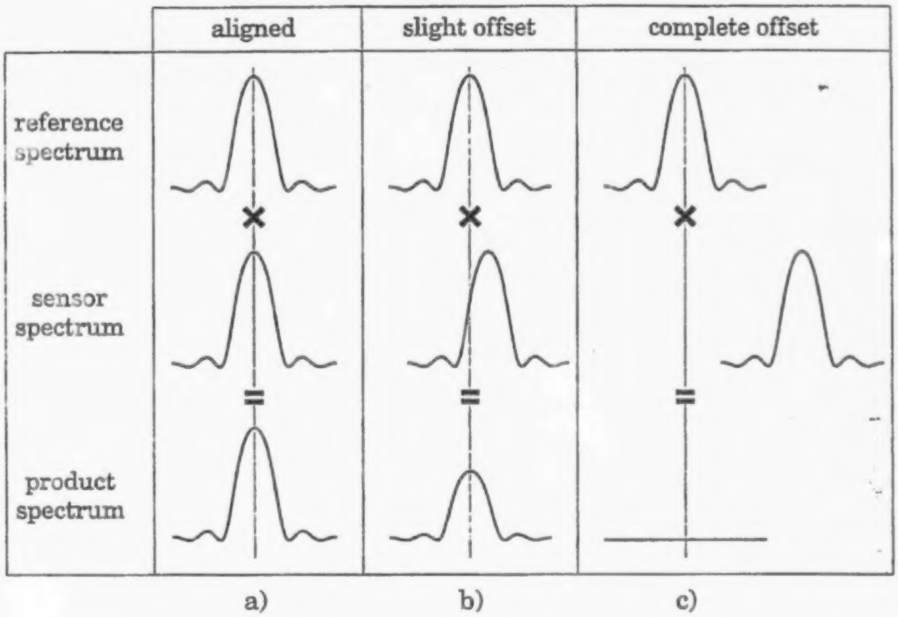

Figure 4.6: The principle of the new detection scheme is based on the convolution (product) of the gratings' responses. In the convolution integration, the following scenarios are observed: a) gratings aligned b) slightly offset and c) completely offset.

Bragg gratings (uniform coupling coefficient over the grating length) and apodized Bragg gratings (weighted coupling coefficient which reduces the sidebands).

For the calculations, we sequentially shifted the wavelength response of the sensor Bragg by small amounts and multiplied it by the spectrum of the reference Bragg, assuming identical Bragg gratings. A sample of the program is included in appendix G.

The results of the spectral convolution for the configuration $S(\omega) \cdot (1 - R(\omega))$ are shown in figure 4.7. Results for uniform and apodized Bragg gratings are shown. The maximum reflectivity of each grating is 70% and the length of the apodized grating is chosen as twice the length of the uniform grating in order to keep the same relative index difference. To evaluate the range of linearity, different tolerance errors were taken into account. We have extracted in figure 4.7 the linear part of the convolution result for maximum tolerance errors of 2%, 5% and 10%.

In figure 4.8 is shown the convolution results for the configuration $S(\omega) \cdot R(\omega)$ for the same grating reflectivity (70%).

When we compare the $S(\omega) \cdot (1 - R(\omega))$ configuration to the $S(\omega) \cdot R(\omega)$ configuration we observe that the signal has a negative slope in the second case and that the signal goes

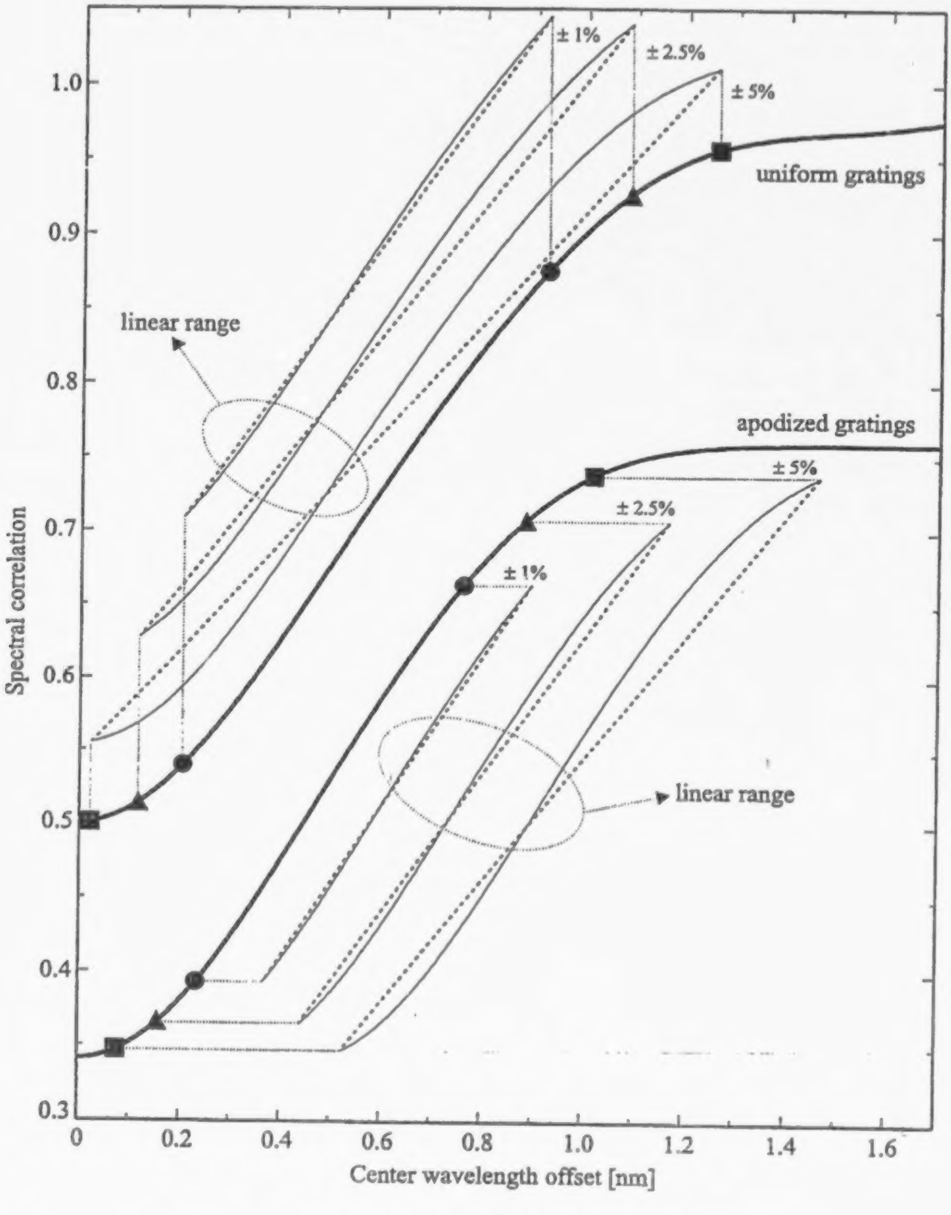

Figure 4.7: Spectral convolution $S(\omega)\cdot(1-R(\omega))$ between two identical uniform and apodized Bragg gratings. Linear regions are extracted for different tolerance errors on the linearity.

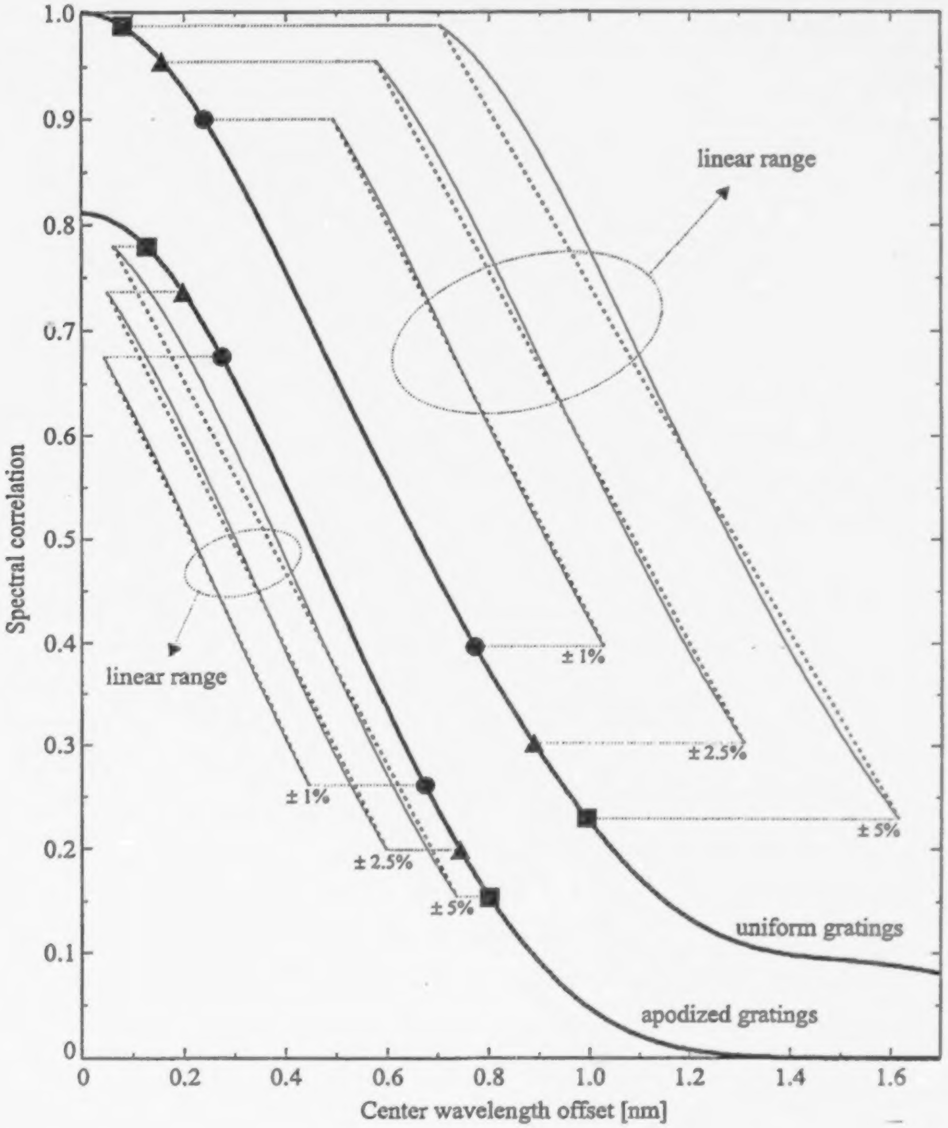

Figure 4.8: Spectral convolution $S(\omega) \cdot R(\omega)$ between two identical uniform and apodized Bragg gratings. Linear regions are extracted for different tolerance errors on the linearity.

to zero in the case of the apodized gratings. Also, as expected, the apodized gratings give lower signals because of the absence of sidebands.

The numerical results are summarized in Table 4.1. Considering that the gratings are identical for both configurations, the $S(\omega)\cdot(1-R(\omega))$ case shows a slight advantage over the $S(\omega)\cdot R(\omega)$ case for the wavelength ($\Delta\lambda$) variation and for the reflectivity variation (ΔR) related to the maximum signal variation. The slope for the apodized gratings are higher than for the uniform gratings.

	tolerance error	$S\cdot R$		$S\cdot(1-R)$	
		uniform	apodized	uniform	apodized
$\Delta\lambda$ (nm)	1%	0.42	0.32	0.53	0.41
	2%	0.53	0.40	0.72	0.53
	5%	0.73	0.55	0.97	0.73
	10%	0.91	0.67	1.24	0.94
ΔR (%)	1%	40.8	41.5	53.4	52.3
	2%	50.2	51.0	65.0	64.7
	5%	65.1	66.2	79.9	81.6
	10%	75.7	77.0	88.4	93.3
slope (%/nm)	1%	−0.961	−1.298	0.969	1.557
	2%	−0.940	−1.273	0.932	1.500
	5%	−0.890	−1.212	0.851	1.378
	10%	−0.830	−1.143	0.738	1.217

Table 4.1: Wavelength and reflectivity percentage variations for the different tolerance errors on the linearity.

Because of no sideband interactions and for the higher slope, which is better for low accelerations, apodized gratings offer better performance.

4.3 Measurement setup

The new detection scheme requires some modifications to the measurement setup used in phase 3.

First, we designed a new fiber mount. Measurements in phase 3 have shown resonances coming from loose screws and guiding rods in the original mount. The new mount is illustrated in figure 4.9. The fiber Bragg grating is inserted in a ceramic ferrule having an inner diameter of 140 microns. The fiber is then glued to the ceramic ferrule which is inserted

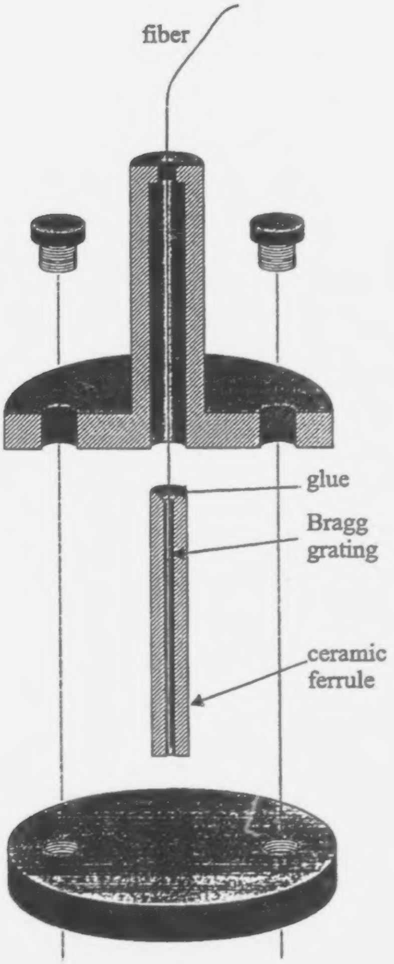

Figure 4.9: Illustration of the new fiber mount using a ceramic ferrule.

in the mount. The length and the diameter of the mounting hole are equal to those of the ceramic ferrule so the ferrule is tightly held in place once the bottom plate is screwed to the mount. The advantage of the ceramic ferrule is in its very precise hole diameter and its uniform inner surface. Again, the fiber end in the ceramic ferrule is polished at an angle to ensure that there is no reflection from the fiber end air-glass interface.

The experimental setup corresponding to the LED detection scheme is shown in figure 4.10. Compared to the laser setup described in phase 2, this setup is a lot more simpler in many ways. The laser diode, the temperature controller, the polarization controller, the laser optical frequency-locking setup using a Bragg grating and the isolator are replaced by a single LED. Actually we use a super luminescent diode (SLD) which is an LED with a high

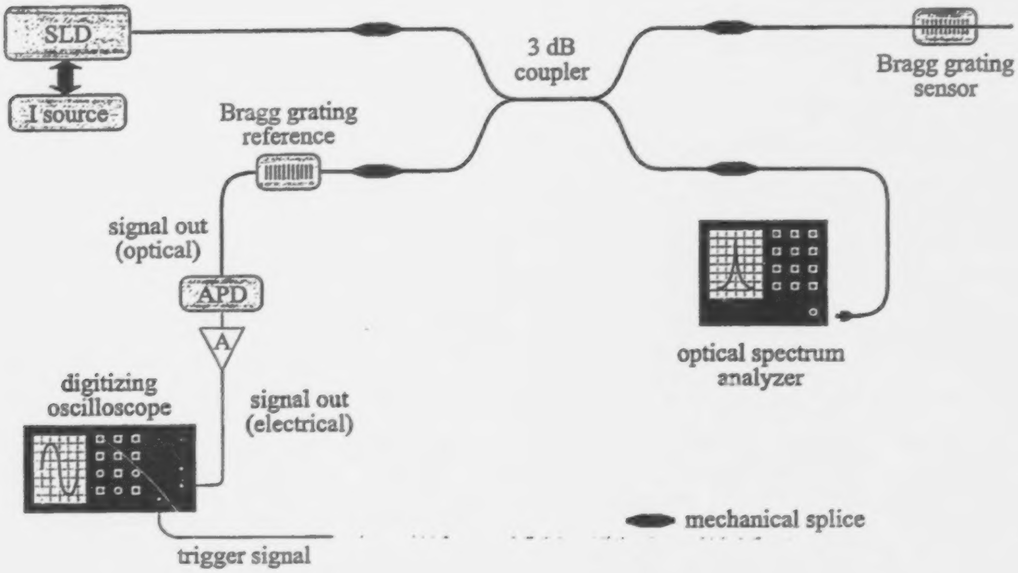
SLD
I source
Bragg grating reference
3 dB coupler
Bragg grating sensor
signal out (optical)
APD
A
digitizing oscilloscope
signal out (electrical)
optical spectrum analyzer
mechanical splice
trigger signal

Figure 4.10: Illustration of the setup used for the LED detection scheme.

output optical power. Also a low-noise amplifier is placed after the avalanche photodiode because only a small fraction of the SLD optical power is reflected by the Bragg gratings. The SLD specifications are included in appendix H.

The Bragg gratings used are slightly apodized and have a maximum reflectivity of 70%. Spectrally they have a little offset and the one at the shorter center wavelength is used as the reference.

4.4 Experimental results

The measurements were made at DREV using the Hopkinson bar. A summary of all the tests is included in appendix F. Almost all tests were made at accelerations around 100 kg$_n$.

In figure 4.11 is shown a typical result for the $S(\omega) \cdot (1 - R(\omega))$ configuration. During the acceleration pulse the sensor signal follows well the acceleration signal, as shown in the inset where the level of the first pulse has been fitted to the level of the acceleration. In that case the maximum acceleration is 110 kg$_n$.

In figure 4.12 is shown a typical result for the $S(\omega) \cdot R(\omega)$ configuration. For this configuration, the sensor signal goes down first, so for comparison it has been reversed. During the acceleration pulse the sensor signal follows well the acceleration signal, as shown in the inset where the level of the first pulse has been fitted to the level of the acceleration. In that

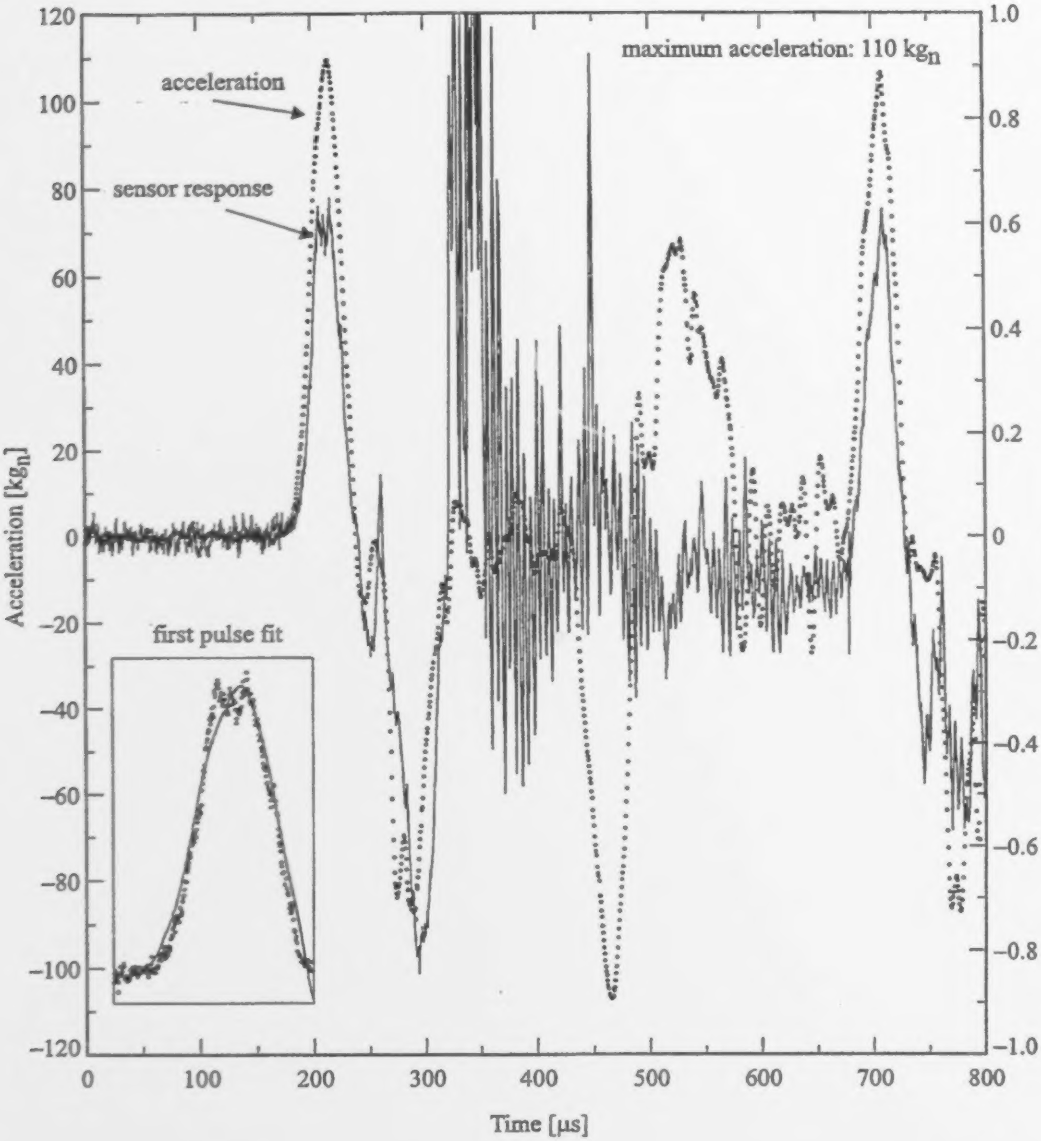

Figure 4.11: Typical result for the $S(\omega) \cdot (1 - R(\omega))$ configuration. The level of the first pulse is fitted to the acceleration in the inset.

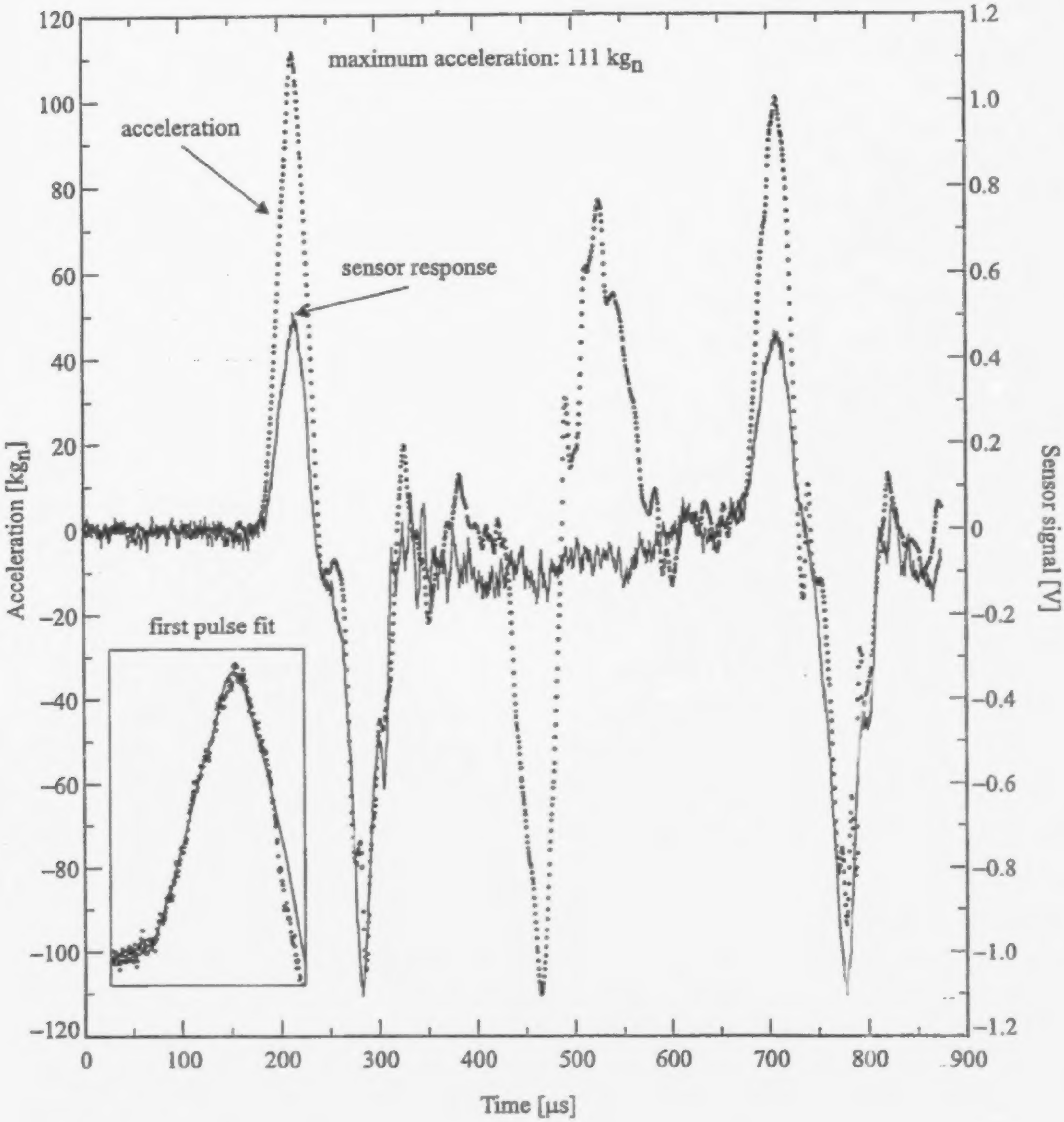

Figure 4.12: Typical result for the $S(\omega) \cdot R(\omega)$ configuration. The level of the first pulse is fitted to the acceleration in the inset.

case the maximum acceleration is 111 kg_n. The signal is also less noisy between acceleration pulses.

The Hopkinson bar setup was moved a few weeks before the visit and was not working optimally. The first results were not particularly good because of the instability in the bar setup. Also we experienced some noise that was related to the ceramic ferrule. The compressibility of the ferrule appeared to be higher than expected, even if the hole is large enough compared to the fiber diameter, i. e. 140 to 125 microns.

In spite of relatively good fits for the acceleration pulses in figures 4.11 and 4.12 the setup suffers from instabilities of the optical source. Any changes in the phase (e.g. handling of the fiber) of the light back reflected to the source also produced changes in the DC levels at the detector. This situation is not acceptable because it is difficult to distinguish between a real acceleration or a simple spectral change of the SLD. Also the spectrum of the source is not free of ripples. These ripples change with time in amplitude and phase.

4.5 Analysis

We have presented a new configuration to measure acceleration using a fiber Bragg grating. The setup is simpler because it uses an LED as the optical source. The setup is insensitive to temperature changes and is less sensitive to back reflections. Results show in some cases a good fit to the acceleration pulses but we found other problems which limit the usefulness of the setup. Instabilities in the LED spectrum and the presence of time varying ripple remain unresolved issues.

The new mount using a ceramic ferrule produced responses with strong mechanical resonances. It is still unknown whether the problem is caused by the use of different materials (e.g. aluminium mount and ceramic ferrule) or the unsuitable compressability of the ceramic.

After review of the results in phase 3 and 4 it was decided to adopt a modified laser diode setup for the final prototype. The improved performance provided by the locking fiber Bragg grating in front of the source promises temperature insensitivity and a more compact setup. The principal problem with this approach is the presence of the natural cavity of the laser diode which causes difficulties in finding optimum operating conditions of the laser diode (e.g. temperature, injection current and operating wavelength of the control Bragg grating).

Phase 5

Final Prototype

In this phase we present the final prototype. The objective of this phase of the project is to produce a prototype in a small package compatible with hard target munitions which can be powered from batteries. The sensor consists of a sensor head which includes the Fiber Bragg Grating (FBG) in a small cylindrical mount and the control unit. The sensor head is attached to the control unit by an optical fiber. Also presented in this phase are the low acceleration tests carried out with the column test apparatus. Finally a discussion on the operation of the prototype closes the section.

5.1 Schematic

The schematic of the final prototype is shown in figure 5.1. The setup is based on the laser diode configuration previously described in phase 2. The source is slightly modified from the original design; the polarization controller and the optical isolator used to isolate the laser diode from unwanted reflections are removed. The reference Fiber Bragg Grating (FBG) has a stronger reflectivity than before to isolate better the source from back reflections in the laser diode. Also the temperature controller of the laser diode is removed to allow operation independent of the temperature.

As indicated in figure 5.1 the sensor is composed of the sensor head and the control unit. The sensor head includes the Fiber Bragg Grating sensor in the aluminum mount described in phase 2 and 3. The control unit is attached to the sensor by an optical fiber which can be meters long if necessary. The control unit which is powered by a voltage of 5 V dc includes the laser diode, the Avalanche Photodiode (APD), the 3 dB fused coupler and the two miniature power supplies. The power supply for the laser diode is a current source which

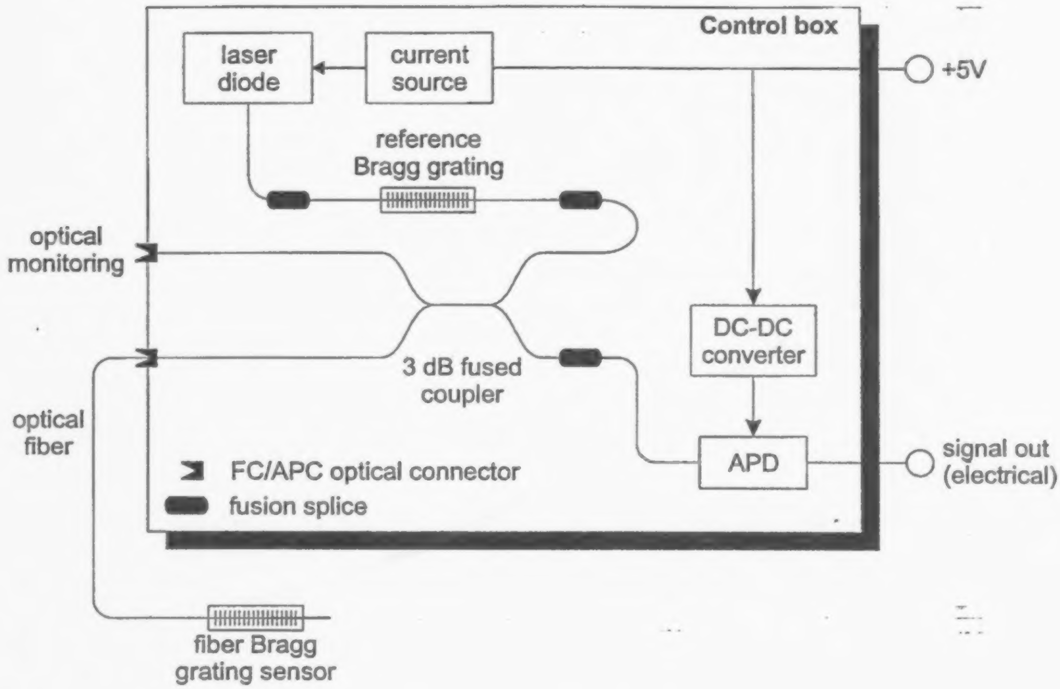
Control box
laser diode
current source
+5V
reference Bragg grating
optical monitoring
DC-DC converter
3 dB fused coupler
optical fiber
APD
signal out (electrical)
FC/APC optical connector
fusion splice
fiber Bragg grating sensor

Figure 5.1: Schematic of the final prototype.

can draw as much as 150 mA. The power supply for the APD is simply a DC-DC converter which generates 185 V at a maximum load current of 6.25 mA.

Figure 5.2 shows the electrical schematic of the circuit. The layout of the printed circuit board is shown in figure 5.3. The dimension of the PCB is 4.5 x 4.5 cm, and the overall dimension of the complete package without the sensor is 6.5 x 5.5 x 5.1 cm. The sensor is attached by an optical fiber supplied with a FC/APC connector. The specifications of the components are in appendix H.

5.2 Operation of the Final Prototype

In principle this configuration should provide temperature insensitive operation. This is true in the sense that both gratings (reference and sensor) experience the same ambient conditions and thus shift by equal amounts, maintaining proper relative positioning between the laser emission and the sensor.

The principal role of the reference FBG is to lock the emission spectrum of the laser diode by providing optical feedback. Without the reference grating the laser diode would

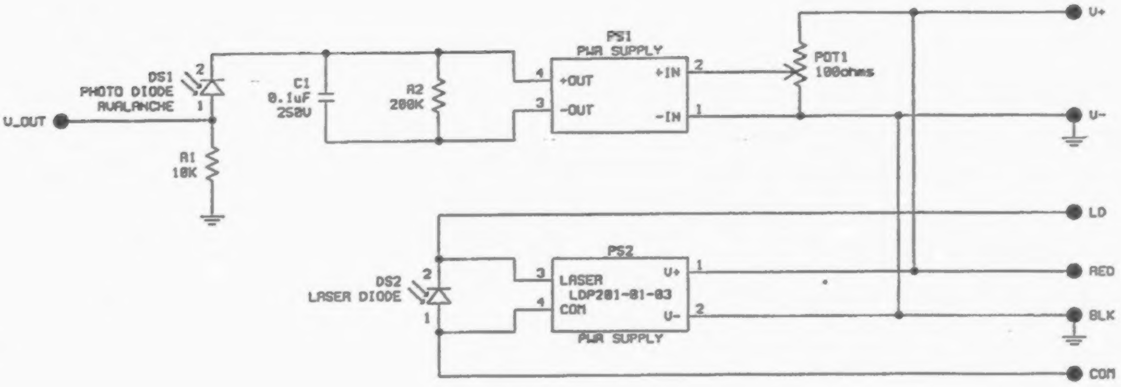
PS1
PWR SUPPLY
+OUT
-OUT
+IN
-IN
POT1
100ohms
V+
V-
DS1
PHOTO DIODE
AVALANCHE
C1
0.1uF
250V
R2
200K
V_OUT
R1
10K
LD
PS2
LASER
LDP201-01-03
COM
V+
V-
PWR SUPPLY
DS2
LASER DIODE
RED
BLK
COM

Figure 5.2: Electrical schematic of the circuit.

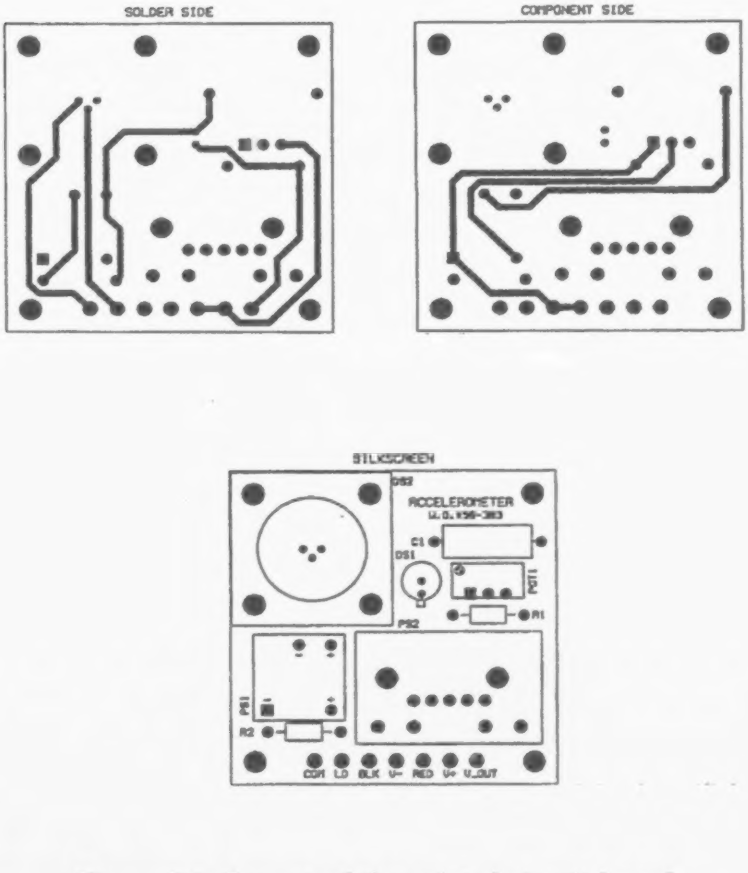
SOLDER SIDE
COMPONENT SIDE
SILKSCREEN
DS2
ACCELEROMETER
C1
DS1
POT1
R1
PS2
PS1
R2
COM
LD
BLK
V-
RED
V+
V_OUT

Figure 5.3: Layout of the printed circuit board.

be multimode with mode spacing as determined by the length of the laser diode cavity. The reference FBG creates a second cavity with the rear mirror of the laser diode. This second cavity selects a single lasing mode of the laser and locks its emission wavelength. It is important to notice that the relative positioning between the emission wavelength and the sensing FBG has to be maintained as before. The principal difficulty in achieving this precise relationship is the discrete emission of the laser modes. The laser diode consists of two mirrors, the rear mirror with a high reflectivity and the front one with a low reflectivity to permit good out coupling efficiency. Lasing occurs on discrete modes only, and because of the short length of the cavity the modes are spread far apart (0.3 nm spacing). In order to fine tune the emission spectrum of the laser relative to the FBG sensor it would be much more convenient to have modes spaced closer together or even better to have true continuous tuning.

One solution to this problem is to remove the reflectivity of the front mirror by applying an anti-reflection coating or by using an angled facet. This would eliminate the original laser cavity by removing the front mirror of the laser diode but keeping intact the gain of the laser diode. Indeed the mode spacing is determined by the length of the laser cavity therefore placing the reference FBG as the sole output mirror at a large distance from the diode would produce finer mode spacing. This way the source would have a single output mirror (the reference FBG) and would have a much smaller mode separation (going from 0.3 nm spacing to 0.001 nm for a spacing of 5 cm between the laser diode and the reference FBG). The source would then become multimode with a large number of modes falling underneath the reference FBG spectrum. Fine tuning would then be possible with a resolution of 0.001 nm.

Also this would solve another problem related to the temperature sensitivity of the source. In practice it is not impossible that a temperature change could cause some detuning of the source and prevent the sensor from operating properly. This is true when the reference FBG tries to pull the wavelength of the source between two modes of the laser diode cavity; what happens then is lasing on two modes at the same time or competition occurring between the modes when lasing alternates between the modes. In practice the most serious problem encountered is the relative positioning between the laser emission and the FBG sensor because of the large mode spacing. The technique used to select the laser wavelength is to stretch-tune the resonant wavelength of the reference FBG to the 3 dB point of the sensor FBG spectral response, but tuning of the laser is discrete going from one mode to another. To help fine tune the wavelength it is possible also to vary the injection current of the laser diode, a technique effective over a smaller wavelength range. Also temperature changes produce small shifts in the laser emission but because the temperature of the laser diode is not controlled, large changes in temperature can produce mode hopping and detune the source.

With an anti-reflection coating or an angled facet on the laser diode output mirror, the temperature changes would then produce a quasi-continuous shift in the source spectrum which would follow the sensor FBG very accurately. Unfortunately applying an anti-reflection coating or an angled facet on the laser diode are beyond the scope of this feasibility study.

Back reflections in the laser diodes have to be minimized to guarantee single mode emission and stable operation. The most serious problem comes from the light back reflected from the sensor FBG which can create an unwanted cavity between the laser rear mirror and the sensor FBG. Any instabilities in the laser diode emission, whether they are in light intensity or wavelength would create light level changes at the photodetector which would be interpreted as false acceleration signals. Typically these instabilities are small fluctuations in light intensity and show up as noise. For this reason the use of a stronger reflectivity Bragg grating provides better isolation than a weaker one but at the expense of lower output power from the source. The output power is not a concern with the new laser diode which generates as much as 8 mW of optical power in the singlemode optical fiber.

Another way to achieve finer tuning of the laser diode source is to use a Distributed Feedback (DFB) laser diode. DFBs are singlemode laser diodes developed for high speed fiber optics communications. The operating wavelength of these laser diodes is 1300 and 1550 nm, wavelengths where the optical fibers produce lower losses. Unfortunately DFBs are not available at 830 nm. Apart from their single mode operation they can be tuned continuously by varying their injection current. The DFBs are sensitive to back reflections also but fortunately very small optical isolators can be integrated with the laser diode. The only drawback is the higher cost. Originally the reasons for operating at 830 nm were the higher sensor sensitivity and lower costs. Now it turns out that the sensors offer more than adequate sensitivity and operation at 1550 nm would be possible.

5.3 Results

Results using the final prototype obtained at low acceleration levels using the column test apparatus are shown in figure 5.4. The sensor gives good results which agree well to results obtained with the Endevco reference sensor as shown in figure 2.18.

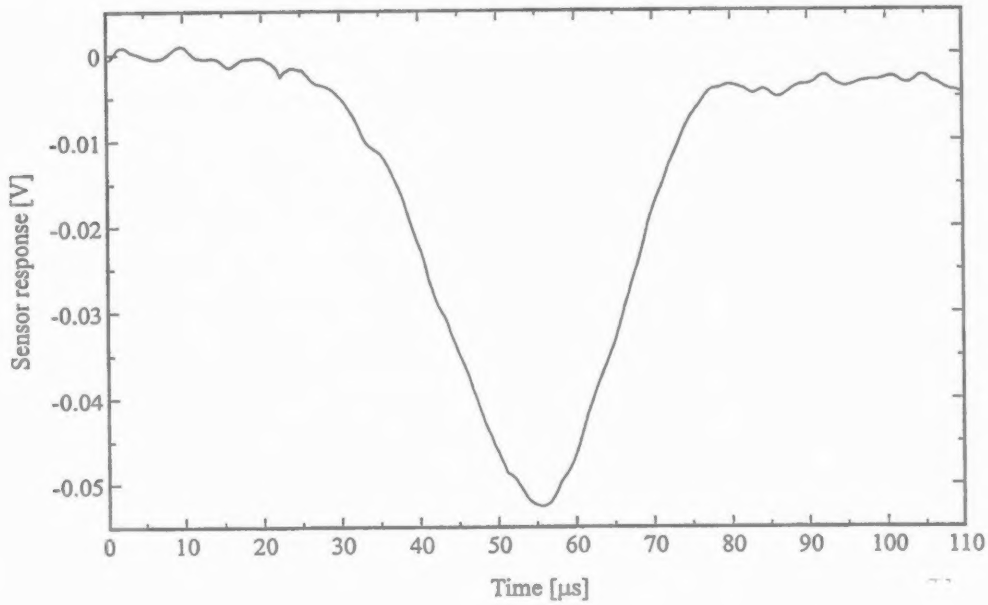

Figure 5.4: Ball-dropping low acceleration test measured using final prototype.

Conclusion

This feasibility study of a Fiber Bragg Grating based accelerometer demonstrates the potential of fiber Bragg gratings for high acceleration sensing experienced in impact dynamics applications. In this first study of fiber Bragg gratings as an acceleration sensor a large number of approaches is examined for the sensor head design and the detection of the acceleration signal.

In the first phase of the study, calculations made using finite elements help design a simple sensing element based on the measurement of the strain developed across a FBG. The strain experienced by the FBG comes simply by the elongation of a short 1-cm long section of bare fiber attached at one end only. Interestingly, such a sensor shows a quasi-linear response to acceleration and also a large damping of its mechanical resonance. This damping of the mechanical resonance is still unexplained but is very important in allowing flexibility in the design of the sensor.

In the second phase of the study several measurement techniques are analyzed to sense the strain across the FBG under acceleration. The first approach is to use a narrowband laser diode as an optical source. The bandwidth of the laser diode is orders of magnitude smaller than the bandwidth of a short 1-mm long sensing element located at the base of the free fiber close to its anchor position. The acceleration is measured by placing the laser diode emission wavelength on a quasi-linear region of the sensor spectrum; the acceleration across the FBG shifts the central wavelength of the grating producing a corresponding change in amplitude of the detected signal.

The second approach consists in using a wide bandwidth light emitting diode as a light source. In this case a longer FBG is used over the entire length of the free fiber. Under acceleration the grating experiences a linear variation of the strain over its length, producing a chirp in its optical spectrum. The integration of the chirp spectrum produces a measure of the acceleration.

In the third phase of the project a sensor is built using the laser diode measurement technique. The sensor is tested at low and high accelerations. Under proper operating conditions the sensor shows good sensitivity, a quasi-linear response, good dynamic range, small cross-axial sensitivity and low mechanical resonances. The problems with this technique is the biasing of the laser diode which is sensitive to the ambient conditions. The sensor mount which houses the FBG works well enough to observe the successive high acceleration pulses but problems associated with its mechanical resonances need further analysis that are beyond the scope of this feasibility study.

Phase 4 of the project looks at a third measurement technique of the strain across the FBG to reduce the sensitivity to the operating conditions. Again a wide bandwidth source, a super radiant diode, is used in place of the laser diode. Rather than using a long FBG as shown in phase 2, a pair of short gratings are used. The relative shift between a reference FBG and the sensing FBG produce the acceleration signal. Results at high accelerations show the potential of this technique but instabilities in the optical source cause difficulties.

In the last phase of the feasibility study, a final prototype is built. The prototype uses the laser diode measurement technique which gives the best results but suffers from sensitivity to operating conditions. The sensing head is attached by an optical fiber to the measurement unit which can be powered by a 5 Volts battery. The measurement unit which contains commercially available components is contained in a package measuring 6.5 x 5.5 x 5.1 cm. Further miniaturization would be possible by integrating the source and detector in a single unit.

Two problems remain at the end of this feasibility study. The first one is related to the housing unit of the fiber Bragg grating. Proper analysis of its construction and the selection of appropriate materials should solve this problem. The second problem is the optical source. The laser diode shows good performance but too much sensitivity to precise biasing. Recently, new laser diodes have been fabricated with an angled output facet coupled to lensed optical fibers. This new development offers the promise of solving the problems experienced in biasing the laser diode. Such an angled facet laser diode can be tuned continuously over a bandwidth of about 1-nm. Such a source has the potential of producing a truly temperature insensitive acceleration sensor.

Appendix A

Trigger setup and signals

The measurement of an acceleration signal is a one-shot (not repetitive) experiment and the duration is quite short. We have to know when to start the acquisition of the signal. So we have added an optical trigger to the accelerometer apparatus.

We have placed an LED and a photodiode on the large cylinder of the accelerometer and they are diametrally opposite. The LED shines on the photodiode but when the steel ball falls and passes in front of the LED, it prevents the light from reaching the photodiode. Then the signal becomes null for a short amount of time. We can use the negative or the positve transition of the signal as a trigger to start the acquisition.

The generated trigger signals are plotted in figure A.1 for each ball provided with the apparatus. We observe that the duration of the blocked signal caused by the 2 inches ball is two times longer than the one generated by the 1 inch ball.

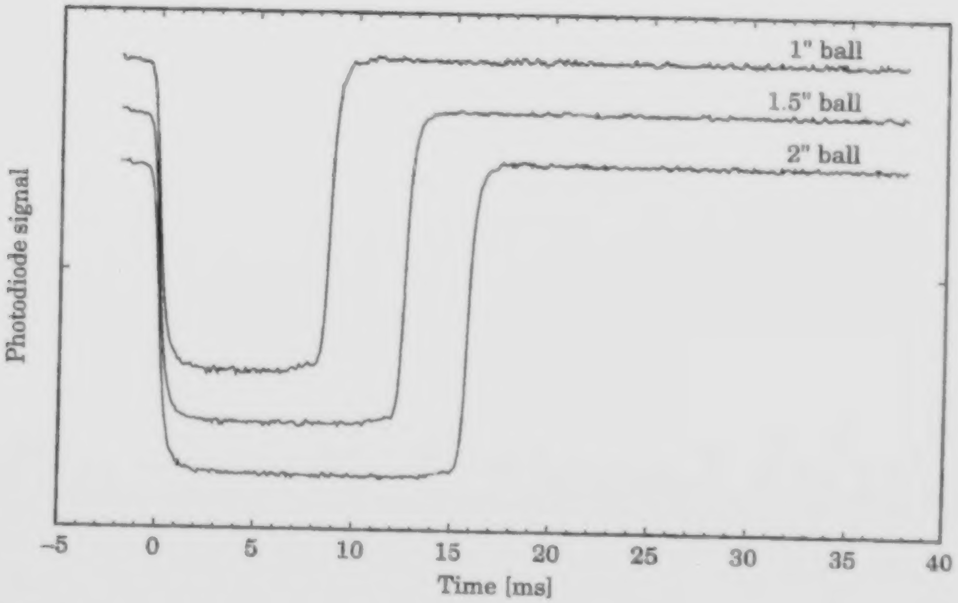

Figure A.1: The trigger signals for the 3 balls provided. The curves are y-shifted for clarity.

Appendix B

Sensor mount

The complete description of the sensor mount is presented in figure B.1. The material used is aluminum (Al 6061-T6). It is constructed of 2 half cylinders, 15 mm long and 5/8" in diameter. The 2 halves are secured together using 4 setscrews. The optical fiber lays inside two set of grooves. The first groove is 60 μm deep, 5 mm long and is designed to hold tightly a bare fiber of 125 μm diameter; the second groove is 500 μm deep, 1 cm long and protects the free fiber without holding it. The sensor mount can be secured on any surface using 2 setscrews through two 0.120" clearance holes located 3/8" apart along the length of the mount.

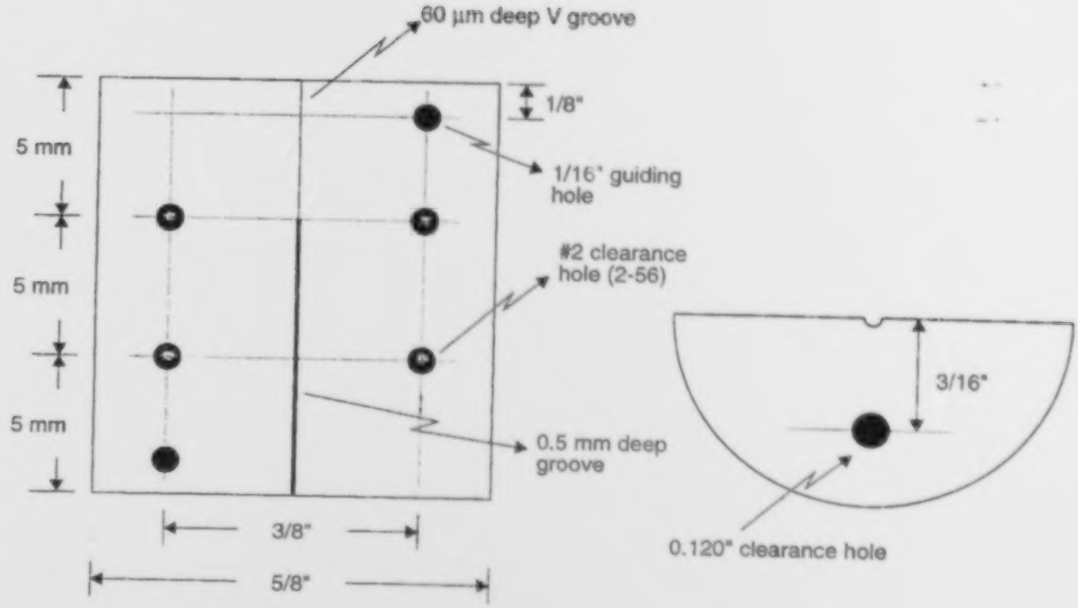
60 µm deep V groove
1/8"
5 mm
1/16" guiding hole
5 mm
#2 clearance hole (2-56)
3/16"
5 mm
0.5 mm deep groove
0.120" clearance hole
3/8"
5/8"

Guiding rod: L = 3/8", D = 1/16"

Material: Al 6061-T6

Figure B.1: Detailed description of the sensor mount.

Appendix C

Fiber preparation

In order to get a relatively precise length of free fiber in the sensor mount, a clean fiber cleave becomes important. Cleaving an optical fiber is a delicate operation which consists in striking the fiber with a diamond tip to introduce a little scratch on the surface of the fiber. To get the right length of fiber, the diamond tip is mounted on a X-Y-Z translating movement. Tension is then exercised along the longitudinal axis of the fiber to produce a clean cut across the face of the fiber section where the fiber was first stroked. The fiber is installed in the mount after the cleave has been practiced.

Also, a perfect cleave has a reflection coefficient of about 4%. To eliminate these unwanted reflections, the fiber end is polished at a angle of 8° using a polishing machine and a special fiber holder.

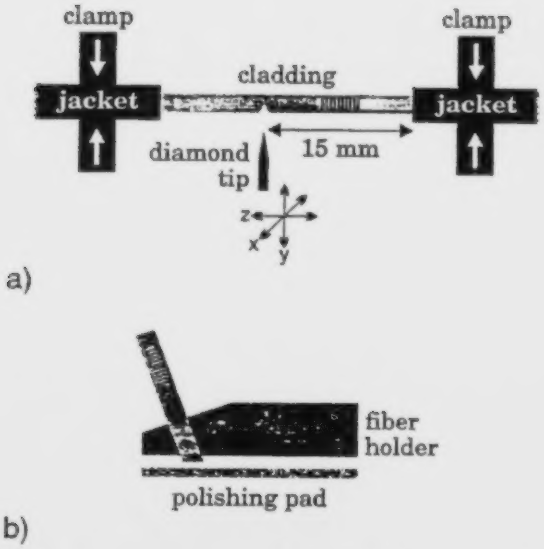
clamp
clamp
cladding
jacket
jacket
diamond
tip
15 mm
z
x
y
a)
fiber
holder
polishing pad
b)

Figure C.1: The sensor preparation involves a) a precise cleaving of the fiber and b) a fiber end angle polishing to reduce unwanted back reflections.

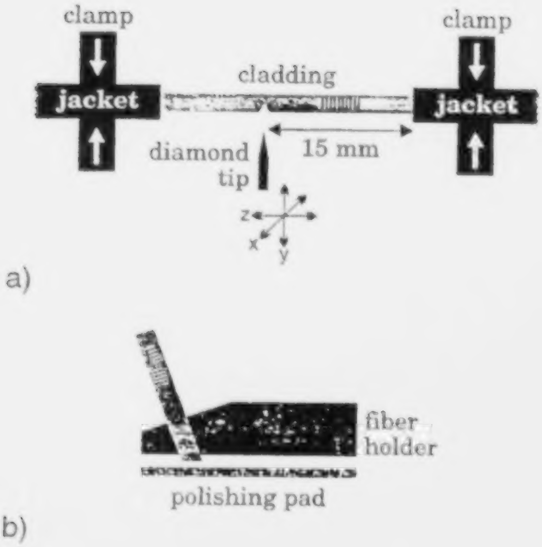
clamp
clamp
cladding
jacket
jacket
diamond tip
15 mm
z
x
y
a)
fiber holder
polishing pad
b)

Figure C.1: The sensor preparation involves a) a precise cleaving of the fiber and b) a fiber end angle polishing to reduce unwanted back reflections.

Appendix D

Cantilever: filtering

To solve the signal to noise ratio problem experienced with the cantilever sensor, we put a 100 kHz low-pass filter between the cantilever and the digitizing oscilloscope. The result is presented in figure D.1. The characteristic of the signal is greatly improved without affecting the performance.

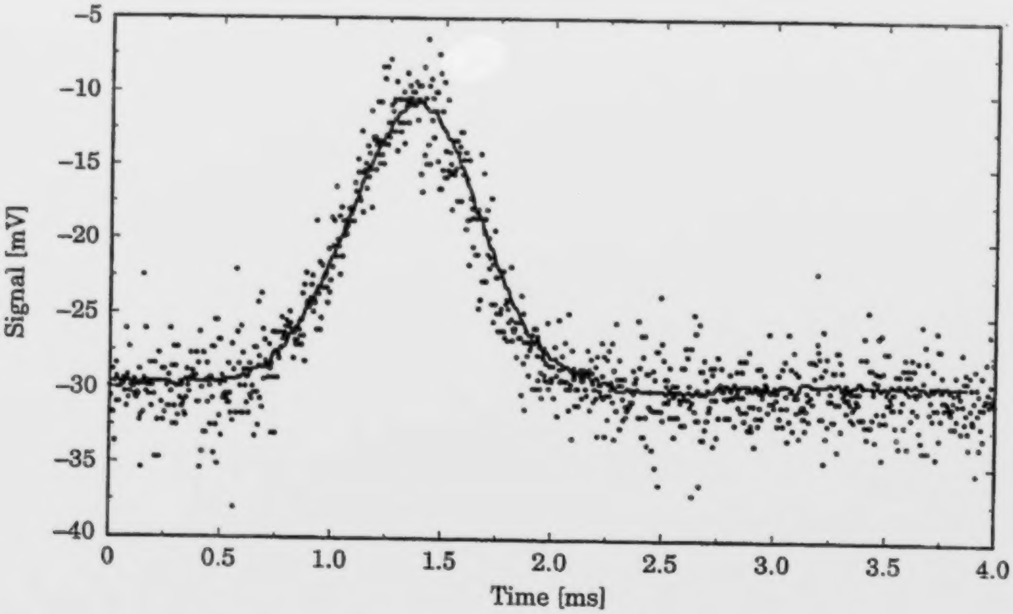

Figure D.1: Noise reduction by the introduction of a 100 kHz low-pass filter in the cantilever measurements.

Appendix E

Original recordings

The original recordings of the fiber-Bragg sensor are shown in the next two pages. The offset between each curve is caused by a small change in the laser frequency.

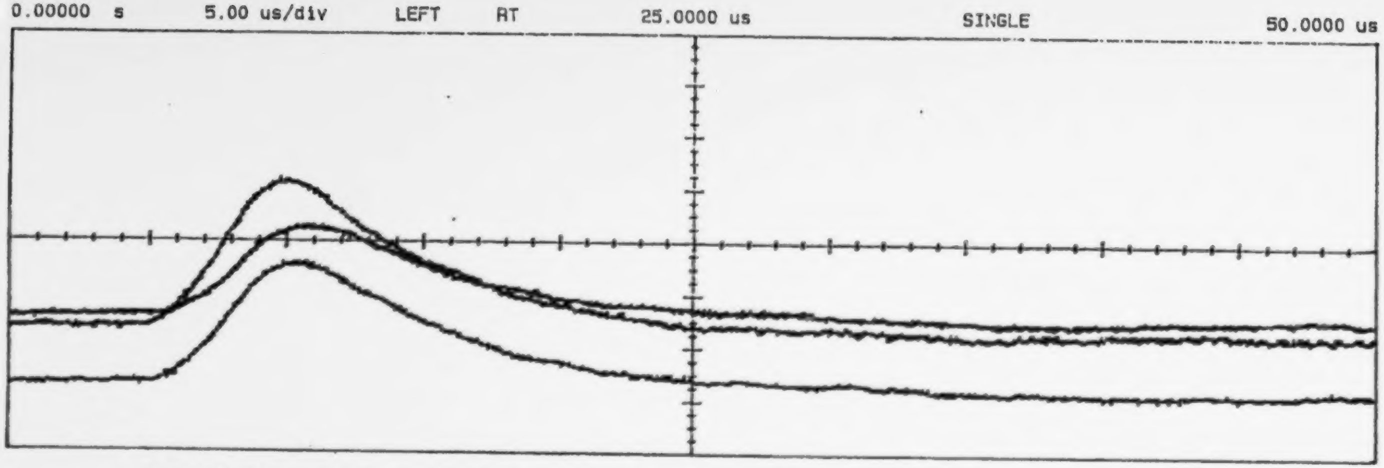

```
            Sensitivity   Offset        Probe         Coupling     Impedance
WMemory 1   100  mV/div   6.95000  V  50.0 us/div   22.0700 ms   RealTime
WMemory 2   100  mV/div   6.95000  V  50.0 us/div   24.4901 ms   RealTime
WMemory 3   100  mV/div   6.95000  V  50.0 us/div   28.1201 ms   RealTime

  Trigger Mode: Edge
On the Positive Edge of External
Trigger Level(s)
  External = 1.00000  V (noise reject OFF)
Holdoff = 40.000  ns
```

Memory nbr	Corresponding ball	Rise time (µs)	ΔV (mV)
WMemory 1	Large	51.2	278
WMemory 2	Medium	54.2	228
WMemory 3	Small	50.2	169

Laser: 46 mA, 19.6 oC
Bragg: 36.3 oC

Printed: 23 JAN 1995 at 09:36:18

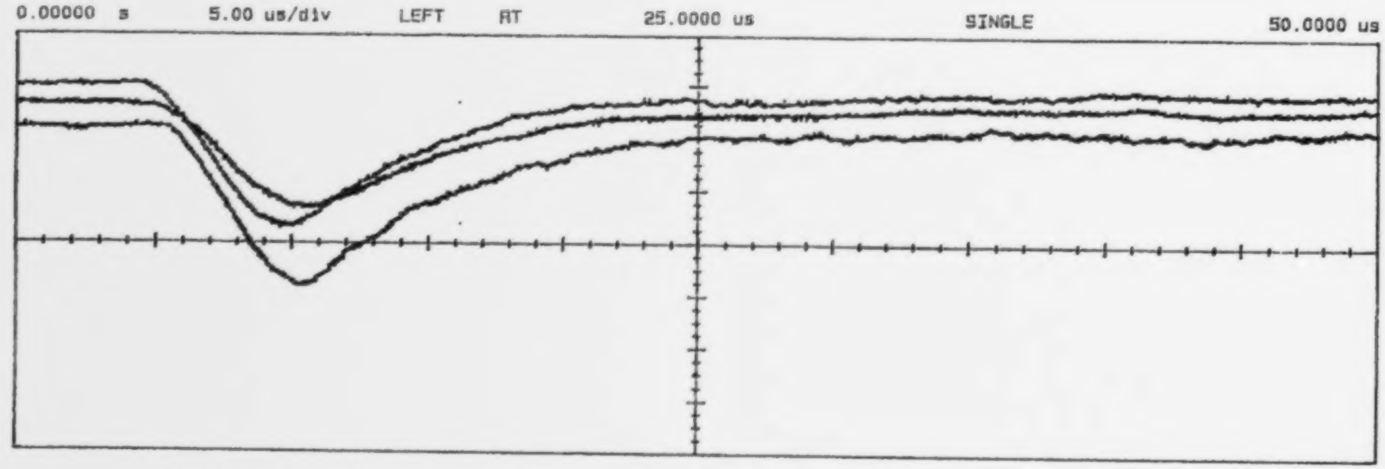

```
                Sensitivity    Offset         Probe        Coupling    Impedance
WMemory 1       100  mV/div   6.87500  V  50.0 us/div   22.1301 ms    RealTime
WMemory 2       100  mV/div   6.67500  V  50.0 us/div   24.5401 ms    RealTime
WMemory 3       100  mV/div   6.67500  V  50.0 us/div   28.1101 ms    RealTime

  Trigger Mode: Edge
On the Positive Edge of External
Trigger Level(s)
  External = 1.00000  V (noise reject OFF)
Holdoff = 40.000  ns
```

Memory nbr	Corresponding ball	Rise time (µs)	ΔV (mV)
WMemory 1	Large	52.0	303
WMemory 2	Medium	54.0	269
WMemory 3	Small	55.8	197

Laser: 46 mA, 18.1 °C
Bragg: 31.8 °C

Printed: 20 JAN 1995 at 17: 00: 10

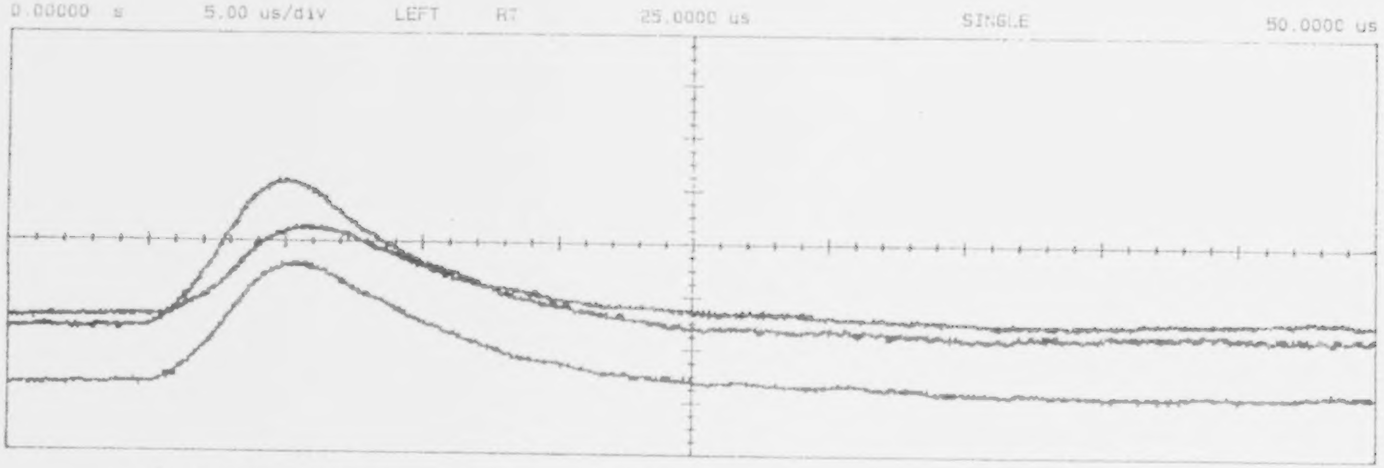

```
              Sensitivity     Offset          Probe        Coupling    Impedance
WMemory 1     100  mV/div   6.95000  V  50.0 us/div   22.0700 ms    RealTime
WMemory 2     100  mV/div   6.95000  V  50.0 us/div   24.4901 ms    RealTime
WMemory 3     100  mV/div   6.95000  V  50.0 us/div   28.1201 ms    RealTime

  Trigger Mode: Edge
On the Positive Edge of External
Trigger Level(s)
  External =  1.00000  V (noise reject OFF)
Holdoff = 40.000  ns
```

Memory nbr	Corresponding ball	Rise time (µs)	ΔV (mV)
WMemory 1	Large	51.2	278
WMemory 2	Medium	54.2	228
WMemory 3	Small	50.2	169

Laser: 46 mA, 19.6 °C
Bragg: 36.3 °C

Printed: 23 JAN 1995 at 09:36:18

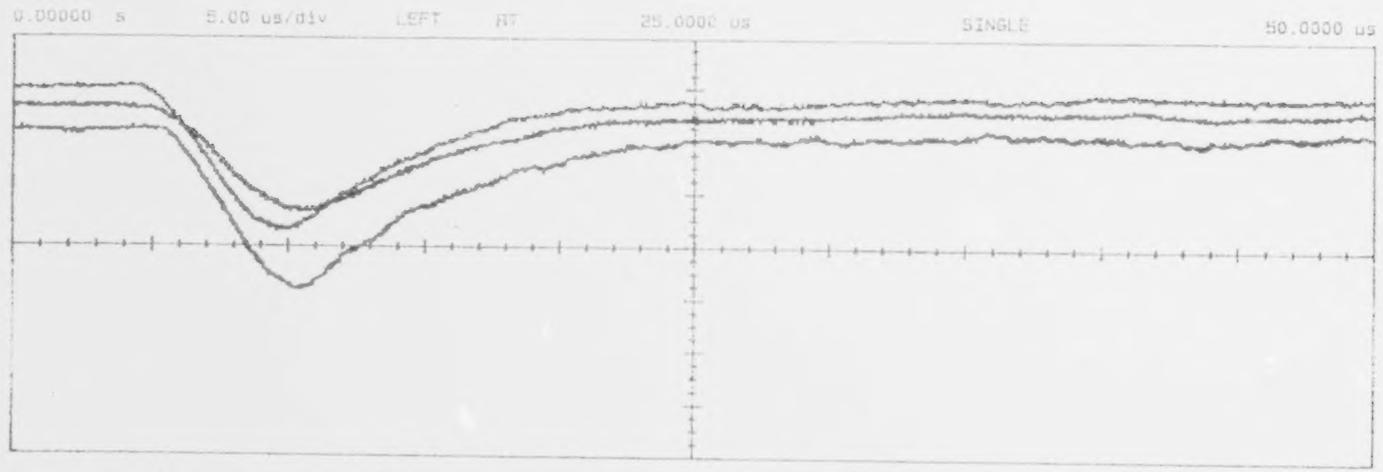

```
              Sensitivity     Offset          Probe        Coupling    Impedance
WMemory 1     100  mV/div    6.67500   V  50.0 us/div   22.1301 ms    RealTime
WMemory 2     100  mV/div    6.67500   V  50.0 us/div   24.5401 ms    RealTime
WMemory 3     100  mV/div    6.67500   V  50.0 us/div   28.1101 ms    RealTime

  Trigger Mode: Edge
On the Positive Edge of External
Trigger Level(s)
  External =  1.00000  V (noise reject OFF)
Holdoff = 40.000  ns
```

Memory nbr	Corresponding ball	Rise time (µs)	ΔV (mV)
WMemory 1	Large	52.0	303
WMemory 2	Medium	51.0	269
WMemory 3	Small	55.8	197

Laser: 46 mA, 18.1 °C
Bragg: 31.8 °C

Printed 20 JAN 1995 at 17:00:10

Appendix F

Visits summary

A summary for each of the last 3 visits at DREV are included in the following pages. Here's a brief description of the content of each column: the first two columns indicate the name of the files saved on two different digitizing oscilloscopes (CRC and DREV); the pressure in PSI; the Bragg grating number; the location of the laser wavelength relative to the Bragg response; the maximum voltage of the sensor signal to the first acceleration pulse; the maximum level of the first acceleration pulse; and some comments about the test.

Fuse tests at CRDV: 2nd visit

CRC file	CRDV file	Pressure (PSI)	Bragg	Laser (side)	Voltage (V)	Acc (G)	Comments
TEST1	0191	75	#23	on left	-0.035	39305	weak signal, laser not on Bragg wavel.
no file	0193	75	#23	on left	-0.128	43197	better
no file	0195	75	#23	on left	-0.425	43394	better
TEST4	0198	75	#23	on left	-0.575	42761	good signal
TEST5	0200	75	#23	on left	-0.340	42015	symmetrical
TEST6	0202	100	#23	on left	-0.460	52791	
TEST7	0204	250	#23	on left	-0.450	77700	
TEST8	0206	75	#23	on left	-0.050	44676	90 degrees, fiber broken, mount pull out
TEST9	0207	200	#17	on left	-0.135	72845	near top of Bragg response
TEST10	0209	200	#17	on left	-0.510	75803	located at low reflectivity
TEST11	0211	200	#17	on left	-0.120	75950	centered
TEST12	0213	200	#17	on left	-0.070	86983	laser at 825.25 nm, centered
TEST13	0215	200	#21	on left	-0.160	90101	Signal decreases with time
TEST14	0217	200	#21	on left	-0.200	78182	Loop with small radius
TEST15	0219	200	#31	on right	0.042	83626	Metal coated fiber, broken
no file	0221	200	#32	on right		79987	fiber broken
TEST17	0223	200	#20	on left	-0.380	84179	Fiber length = 6.5 mm
TEST18	0225	200	#20	on left	0.490	73802	Compression test
TEST19	0227	75	#20	on left	-0.550	53380	Centered, 825.3 nm
TEST20	0229	75	#20	on left	-0.475	51059	Laser OP = 825.28 nm
TEST21	0232	75	#20	on right	0.197	50908	Laser OP = 825.6
TEST22	0234	200	#20	on right	0.620	79590	Laser OP = 825.65
no file	0236	200	#20	on right	0.030	71591	
no file	0237	75	#20	on right	0.056	55353	
TEST23	0239	75	#17	on left	-0.120	48922	
TEST24	0242	75	#24	on left	-0.800	51576	Fiber length = 8 mm
TEST25	0244	75	#24	on left	-0.350	53663	Fiber length = 4 mm
TEST26	0246	75	#25	on left	-0.700	56935	Fiber length = 9 mm
TEST27	0248	75	#25	on left	-0.450	54839	Laser OP shifted to left
TEST28	0250	75	#25	on left	-0.120	46366	Far from top
TEST29	0252	75	#22	on left	-0.275	45398	
TEST30	0254	75	#19	on left	-0.580	57528	

Fuse tests at CRDV: 2nd visit

CRC file	CRDV file	Pressure (PSI)	Bragg	Laser (side)	Voltage (V)	Acc (G)	Comments
TEST1	0191	75	#23	on left	-0.035	39305	weak signal, laser not on Bragg wavel.
no file	0193	75	#23	on left	-0.128	43197	better
no file	0195	75	#23	on left	-0.425	43394	better
TEST4	0198	75	#23	on left	-0.575	42761	good signal
TEST5	0200	75	#23	on left	-0.340	42015	symmetrical
TEST6	0202	100	#23	on left	-0.460	52791	
TEST7	0204	250	#23	on left	-0.450	77700	
TEST8	0206	75	#23	on left	-0.050	44676	90 degrees, fiber broken, mount pull out
TEST9	0207	200	#17	on left	-0.135	72845	near top of Bragg response
TEST10	0209	200	#17	on left	-0.510	75803	located at low reflectivity
TEST11	0211	200	#17	on left	-0.120	75950	centered
TEST12	0213	200	#17	on left	-0.070	86983	laser at 825.25 nm, centered
TEST13	0215	200	#21	on left	-0.160	90101	Signal decreases with time
TEST14	0217	200	#21	on left	-0.200	78182	Loop with small radius
TEST15	0219	200	#31	on right	0.042	83626	Metal coated fiber, broken
no file	0221	200	#32	on right		79987	fiber broken
TEST17	0223	200	#20	on left	-0.380	84179	Fiber length = 6.5 mm
TEST18	0225	200	#20	on left	0.490	73802	Compression test
TEST19	0227	75	#20	on left	-0.550	53380	Centered, 825.3 nm
TEST20	0229	75	#20	on left	-0.475	51059	Laser OP = 825.28 nm
TEST21	0232	75	#20	on right	0.197	50908	Laser OP = 825.6
TEST22	0234	200	#20	on right	0.620	79590	Laser OP = 825.65
no file	0236	200	#20	on right	0.030	71591	
no file	0237	75	#20	on right	0.056	55353	
TEST23	0239	75	#17	on left	-0.120	48922	
TEST24	0242	75	#24	on left	-0.800	51576	Fiber length = 8 mm
TEST25	0244	75	#24	on left	-0.350	53663	Fiber length = 4 mm
TEST26	0246	75	#25	on left	-0.700	56935	Fiber length = 9 mm
TEST27	0248	75	#25	on left	-0.450	54839	Laser OP shifted to left
TEST28	0250	75	#25	on left	-0.120	46366	Far from top
TEST29	0252	75	#22	on left	-0.275	45398	
TEST30	0254	75	#19	on left	-0.580	57528	

Fuse tests at CRDV: 3rd visit

CRC file	CRDV file	Pressure (PSI)	Bragg	Laser (side)	Voltage (V)	Acc. (kG)	Comments
AC_T1	no file	75	#22	on right	0.794t		
AC_T2	no file	75	#22	on right	0.794t		Laser OP shifted to left
AC_T3	no file	75	#22	on right	0.630		
AC_T4	no file	75	#22	on right	0.602		
AC_T5	no file	200	#22	on right	1.233		
AC_T6	no file	200	#22	on right	1.049		
AC_T7	no file	75	#22	on right	1.269		Compression test (with spacers)
AC_T8	no file	200	#22	on right	0.805		f= 287 kHz, one screw broken
AC_T9	0287	200	#21	on right	1.525	93.055	Mount with 500 um hole, f= 333 kHz
AC_T10	0289	75	#21	on right	1.077	45.082	Linearity test, f= 330 kHz
AC_T11	0291	125	#21	on right	1.573	62.010	Linearity test
AC_T12	0293	175	#21	on right	1.858	79.827	Linearity test, f= 333 kHz
AC_T13	0295	300	#21	on right	2.323	101.726	Linearity test, f= 327 kHz
T14	0297	200	#21	on right	1.995	84.028	Fiber taped to the bar
AC_T15	0299	200	#21	on right	2.106	79.160	Stopper in, f= 335 kHz
AC_T16	0301	200	#21	on right	1.939	81.032	Fiber taped to the table
AC_T17	0303	200	#21	on right	2.005	92.816	Fiber loop larger, f= 340 kHz
AC_T18	0305	200	#21	on right	1.846	84.769	Absorber between fiber and bar (cotton)
DC_T19	0307	200	#21	on right	1.875	78.056	Straight fiber
DC_T20	0309	200	#21	on right	0.554	80.860	Laser OP shifted near top
AC_T21	0311	200	#21	on right	1.667	79.155	Loop with very small radius
DC_T22	0313	75	#38	on left	-2.482	54.660	Mount with ceramic ferrule, f= 36 kHz
AC_T23	0315	75	#38	on left	-1.734	79.146	Laser OP shifted to right, near top
AC_T24	0317	75	#38	on left	-1.947	36.180	
DC_T25	0319	200	#38	on left	-4.960	43.519	Laser OP shifted to left, loose screws
AC_T26	0321	200	#38	on left	-4.643	51.806	Laser OP shifted to left
AC_T27	0323	200	#38	on left	-4.093	67.524	Laser OP shifted to left
AC_T28	0325	200	#38	on left	-2.120	67.357	Laser OP shifted to left, best result
DC_T29	0329	200	#37	on left	-2.755	81.264	Mount with 150 um hole, f= 7, 42, 140 kHz
AC_T30	0331	200	#37	on left	-4.928	79.146	Laser OP shifted to right
DC_T31	0333	50	#37	on left	-2.800	36.180	Linearity test, Laser OP shifted to right
AC_T32	0335	75	#37	on left	-3.181	43.519	Linearity test
DC_T33	0337	100	#37	on left	-3.712	51.806	Linearity test
DC_T34	0339	125	#37	on left	-4.659	67.524	Linearity test
AC_T35	0341	150	#37	on left	-4.739	67.357	Linearity test
AC_T36	0343	175	#37	on left	-5.312	79.423	Linearity test
AC_T37	0345	200	#37	on left	-5.386	79.310	Linearity test
AC_T38	0347	200	#37	on left	-5.424	84.343	Linearity test
AC_T38	0349	200	#37	on left	-6.397	108.631	sampling 20 us/div
AC_T39	0351	300	#37	on left	-8.148	103.667	Linearity test
AC_T40	0353	500	#37	on left	-8.408	136.953	Linearity test

Fuse tests at CRDV: 4th visit

CRG file	CRDV file	Pressure (PSI)	Bragg	Laser (side)	Voltage (V)	Acc (kG)	Comments
no file	0441	75	#43	on right	9.880	64.767	G= 2, R= 10 k, strong signal
TEST_2	0443	75	#43	on right	1.253	49.208	G= 2, R= 1 k, weak signal, high DC level
TEST_3	0445	75	#43	on right	1.574	55.546	G= 2, good signal, f= 8, 208 kHz
TEST_4	0447	200	#43	on right	3.047	127.043	lot of noise, f= 200 kHz
TEST_5	0449	150	#43	on right	3.722	281 (??)	same as test 4, noise in strain signal
TEST_6	0451	150	#43	on right	1.805	78.020	G= 1, good signal
TEST_7	0453	75	#42	on right	1.637	64.497	90d, loose screw, noisy
TEST_8	0455	50	#42	on right	0.742	37.880	90d, f= 200 kHz, better but still noisy
TEST_9	0457	75	#42	on right	1.262	49.963	90d, noisy, longer sampling
TEST_10	0459	50	#41	on right	0.088	41.823	90d, 3.5-4 mm (shorter) free fiber
TEST_11	0461	50	#41	on right	0.102	84.888	90d, laser OP shifted to right, clean signal
TEST_12	0463	75	#41	on right	0.303	52.108	90d, mount slightly loose, DC changed
TEST_13	0467	75	#41	on right	0.234	150.511	90d, same as test 12, f= 550 kHz
TEST_14	0465	50	#39	on left	0.314	32.261	90d, mount slightly loose, f= 230 lHz
TEST_15	0469	50	#39	on left	0.191	41.855	90d, same as test 14
TEST_16	0471	50	#39	on left	0.061	90.544	90d, fiber cut in half (~3mm), flat signal
TEST_17	0473	50	#40	on right	1.244	52.101	90d, ceramic, glue is soft
no file	0476	50	#40	on right	0.006	46.339	90d, ceramic, broken fiber
TEST_19	0478	50	#15	on right	3.293	56.366	90d, ceramic, glue is hard
no file	0480	50	#15	on right	0.795	37.117	90d, ceramic taped to the bar
LIN_1	0482	50	#43	on right	1.475	34.046	Linearity test, signal clipped
LIN_2	0484	75	#43	on right	3.043	123.824	Linearity test, signal clipped
LIN_3	0486	200	#43	on right	2.339	89.336	Linearity test
LIN_4	0488	150	#43	on right	2.189	95.378	Linearity test
LIN_5	0490	150	#43	on right	1.370	125.396	Linearity test, no amp
LIN_6	0492	250	#43	on right	1.603	128.222	Linearity test, no amp
LIN_7	0494	200	#43	on right	1.306	106.533	Linearity test, no amp
LIN_8	0496	100	#43	on right	0.950	71.894	Linearity test, no amp
LIN_9	0498	75	#43	on right	0.651	50.612	Linearity test, no amp
LIN_10	0500	300	#43	on right	1.307	96.492	Linearity test, no amp
LIN_11	no file	175	#43	on right	1.160	n/a	Linearity test, no amp
LIN_12	0502	125	#43	on right	1.114	94.198	Linearity test, no amp
LIN_13	0504	150	#43	on right	1.122	84.696	Linearity test, no amp
LIN_14	0506	250	#43	on right	1.504	147.036	Linearity test, no amp
LIN_15	0508	175	#43	on right	1.118	88.854	Linearity test, no amp
LIN_16	0510	85	#43	on right	1.110	89.266	Linearity test, no amp
LIN_17	0512	50	#43	on right	0.602	43.083	Linearity test, no amp
LIN_18	0514	125	#43	on right	1.997	146.353	Linearity test, no amp, no mitigator
LIN_19	0516	200	#43	on right	1.902	174.310	Linearity test, no amp, no mitigator

Fuse tests at CRDV: 5th visit

CRC file	CRDV file	Pres PSI	Bragg Sens/Ref	Ampli gain	R kohm	Acc G	Comments
[illegible]	700	50	F2/F1	10	10	139.220	Epoxy 5min, bad strain signal, noisy between pulses
[illegible]	702	50	F2/F1	100	5	31.765	One stopper removed, very noisy [illegible]
[illegible]	704	50	F2/F1	100	10	27.479	ripples, noisy, dc level changed [illegible]
[illegible]	706	300	F2/F1	100	10	26.167	ripples in the pulse, strong oscillations, very noisy
[illegible]	708	100	F12/F11	100	10	58.419	ripples, dc offset changed [illegible]
6	710	300	F12/F11	100	10	[illegible]	mount base removed, ceramic in contact with bar, good signal
7	712	300	F12/F11	100	10	96.092	no base, strong and good signal, clean [illegible]
T8	714	40	F12/F11	100	10	27.378	weak signal, noisy, dc offset changed [illegible]

F1	716	300	F12/F11	100	10	108.873	1st signal very strong, rest is weak, fiber taped on bar
F2	718	300	F12/F11	100	10	120.998	with base, 2 pulses, very noisy, fiber taped on bar
F3	720	300	F10/F11	100	10	107.842	old mount, noisy, ripples, loose screws
F4	722	300	F10/F11	100	10	106.993	nice signal pulses but very very noisy between each
F5	724	300	F10/F11	100	10	111.439	same as F4 [illegible]
F6	726	300	F12/F11	100	10	115.222	weak signal, very noisy, no base [illegible]
F7	728	300	F12/F11	100	10	109.757	fiber not taped on bar, pulses are nice, periodicity is strange
F8	730	300	F12/F11	100	10	111.424	nice signal, +/- pulses, no base, fiber not taped
F9	732	300	F12/F11	100	10	111.961	nice signal, not symmetric, +/- pulses
F10	734	300	F12/F11	100	10	117.708	noisy, first 2 pulses are +/-, rest is ok and nice

Fuse tests at CRDV: 5th visit

CRC file	CRDV file	Pres PSI	Bragg Sens/Buff	Ampl (ohm)	R (kohm)	[illegible]	Comments
[illegible]	700	50	F2/F1	100	10	[illegible]	Epoxy [illegible] bad strain signal, noisy between pulses
[illegible]	702	50	F2/F1	100	[illegible]	[illegible]765	One stopper removed, very noisy [illegible]
[illegible]	704	50	F2/F1	100	10	[illegible]779	ripples, noisy, dc level changed [illegible]
[illegible]	706	300	F2/F1	100	10	[illegible]	ripples in the pulse, strong oscillations, very noisy [illegible]
[illegible]	708	100	F2/F1	100	10	[illegible]	ripples, no base changed [illegible]
[illegible]	710	300	F12/F1	100	10	[illegible]	mount base removed, [illegible] contact with bar, good signal
[illegible]	712	300	F12/F11	100	10	96.092	no base, strong and good signal, clean [illegible]
[illegible]	714	[illegible]	F12/F11	100	10	[illegible]	weak signal, noisy [illegible]
F1	716	300	F12/F11	100	10	108.873	1st signal very strong, rest is weak, fiber taped on bar
F2	718	300	F12/F11	100	10	120.998	with base, 2 pulses, very noisy, fiber taped on bar
F3	720	300	F10/F11	100	10	107.842	old mount, noisy, ripples, loose screws [illegible]
F4	722	300	F10/F11	100	10	106.993	nice signal pulses but very very noisy between each
F5	724	300	F10/F11	100	10	111.439	same as F4
F6	726	300	F12/F11	100	10	115.222	weak signal, very noisy, no base
F7	728	300	F12/F11	100	10	109.757	fiber not taped on bar, pulses are nice, periodicity is strange
F8	730	300	F12/F11	100	10	111.424	nice signal, +/- pulses, no base, fiber not taped
F9	732	300	F12/F11	100	10	111.961	nice signal, not symmetric, +/- pulses
F10	734	300	F12/F11	100	10	117.708	noisy, first 2 pulses are +/-, rest is ok and nice

Appendix G

Program

The listing of the program used to calculate the linearity region of each configuration ($S(\omega) \cdot R(\omega)$ and $S(\omega) \cdot (1 - R(\omega))$) is included in the next pages. The apodized and non-apodized cases are considered for a maximum grating reflectivity of 70%.

Bragg Calculations Program, Version 3.0

(ST1997)

Purpose: Linearity test for the correlation between two perfect Bragg gratings at different center wavelengths. Comparison between Apodized and Non-Apodized at a reflectivity of 70%, case R*R.

Units: $nm \equiv 10^{-9}$ $\mu m \equiv 10^{-6}$ $mm \equiv 10^{-3}$

Bragg parameters:

Average refraction index: $n := 1.45165$

Length of the reflector: $L_B := 2.0 \cdot mm$

Index variation: $\Delta n := 0.939 \cdot 10^{-3}$

Pitch: $\Lambda_0 := 0.534 \cdot \mu m$

Angle of incidence: $\theta := 0$

Order: $p := 1$

Bragg parameters vector: $Bp := Bparms\left(L_B, n, \Delta n, \Lambda_0, \theta, p\right)$ $factor := 3$

$qmax := 100 \cdot factor$ $q0 := 0 .. qmax$ $q1 := 0 .. 5$ $B1p_{q1, q0} := Bp_{q1}$ $\delta\lambda := \dfrac{0.006}{factor} \cdot nm$

$B1p_{3, q0} := \Lambda_0 + q0 \cdot (\delta\lambda)$

Calculation parameters:

Window span: $\lambda_{span} := 8 \cdot nm$

Window offset: $\lambda_{offset} := 1 \cdot nm$

Wavelength step number: $\lambda c_{nbr} := 500$

Number of integration steps: $cstep\_nbr := 41$

Wavelength index: $jc := 0 .. \lambda c_{nbr}$

Step index: $ic := 0 .. cstep\_nbr$

Z span: $z_{span} := L_B$

Z center: $z_{center} := 0.5 \cdot L_B$

Center wavelength: $\lambda_0 := BBreswavel\left(Bp, 200, 10^{-18}\right)$ $\lambda_0 = 1550.8637 \cdot nm$ $\lambda t_0 := \lambda_0$

Maximum coupling factor: $M\kappa L := BBkappal(Bp, \lambda t)$ $M\kappa L = 2.422$

Maximum reflectivity: $R_{max} := \tanh(|M\kappa L|)^2$ $R_{max} = 96.898 \cdot \%$

Bandwith at Half Maximum: $BB_{bw} := BBfwhm\left(Bp, \lambda_0\right)$ $BB_{bw} = 0.4141 \cdot nm$

Validation bandwith: $CB_{bw} := \dfrac{\Lambda_0}{p} \cdot \dfrac{\lambda_0}{L_B} \cdot cstep\_nbr$ $CB_{bw} = 16.977 \cdot nm$

$$\lambda c_{jc} := \left(\lambda_0 - \frac{\lambda_{span}}{2}\right) + \frac{\lambda_{span}}{\lambda c_{nbr}} \cdot jc + \lambda_{offset} \qquad \lambda 1_{q0} := \left(BBreswavel\left(B1p^{\langle q0 \rangle}, 200, 10^{-18}\right) - \lambda_0\right) \cdot 10^9$$

$$h_c := \frac{L_B}{cstep\_nbr} \qquad zc_{ic} := h_c \cdot ic \qquad zrc_{ic} := if\left[\left[\left(zc_{ic} \le z_{center} + \frac{z_{span}}{2}\right) \cdot \left(zc_{ic} \ge z_{center} - \frac{z_{span}}{2}\right)\right], zc_{ic}, -1\right]$$

No apodization: $\text{nonapo}_{ic} := 1$ Apodization function: $\text{apo}_{ic} := \cos\left[\frac{\pi\cdot\left(zc_{ic} - 0.5\cdot L_{B}\right)}{L_{B}}\right]^{2}$

Chirp definition:

Integration vector: $kc := 0 .. 2$ Chrip integration: $\text{ichirp}_{ic,\,kc} := \int_{0}^{zc_{ic} + kc\cdot h_{c}\cdot 0.5} 1\,dz'$

Calculations:

$CR^{\langle q0\rangle} := \text{CBreflectivity}\left(B1p^{\langle q0\rangle}, \text{cstep\_nbr}, \lambda c, \text{ichirp}, \text{apo}\right)$ $\text{AREA}_{q0} := \left[\sum_{q2=0}^{\lambda c_{nbr}} \left[\left(CR_{q2,\,q0}\right)\cdot\left(CR_{q2,\,0}\right)\right]\right]$

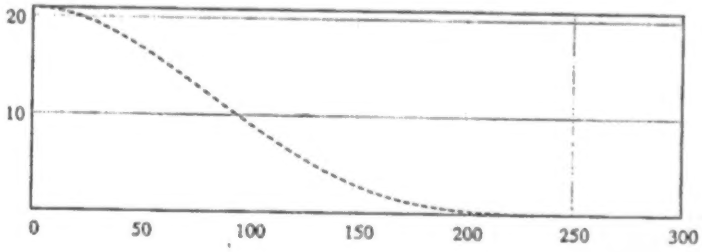

center := 25

Search of linear region: nogood ≡ 0 good ≡ 1

```
data(p, c, A, λ) :=
    maxwidth ← 0
    $v_0$ ← 0
    $v_1$ ← 0
    for j ∈ 0 .. c·factor − 1
        for k ∈ c·factor + 1 .. qmax
            $m \leftarrow \frac{A_j - A_k}{\lambda_j - \lambda_k}$
            result ← good
            $b \leftarrow A_j - m\cdot\lambda_j$
            for l ∈ j .. k
                result ← nogood if $\left|\left(m\cdot\lambda_l + b\right) - A_l\right| > p\cdot A_l$
            if (result = good)·((k − j) > maxwidth)
                maxwidth ← k − j
                $v_0$ ← j
                $v_1$ ← k
    v
```

$\text{data\%}^{\langle 0\rangle} := \text{data}(0.005, \text{center}, \text{AREA}, \lambda 1$

$\text{data\%}^{\langle 1\rangle} := \text{data}(0.01, \text{center}, \text{AREA}, \lambda 1)$

$\text{data\%}^{\langle 2\rangle} := \text{data}(0.025, \text{center}, \text{AREA}, \lambda 1$

$\text{data\%}^{\langle 3\rangle} := \text{data}(0.05, \text{center}, \text{AREA}, \lambda 1)$

$$\text{data\%} = \begin{bmatrix} 54 & 47 & 34 & 22 \\ 109 & 116 & 128 & 138 \end{bmatrix}$$

$pc := 0 .. 3$

$r0 := 0 .. 1$

$X_{0,\,pc} := \lambda 1_{\left(\text{data\%}_{0,\,pc}\right)}$ $X_{1,\,pc} := \lambda 1_{\left(\text{data\%}_{1,\,pc}\right)}$ $\text{LIN}_{0,\,pc} := \text{AREA}_{\left(\text{data\%}_{0,\,pc}\right)}$ $\text{LIN}_{1,\,pc} := \text{AREA}_{\left(\text{data\%}_{1,\,pc}\right)}$

$\Delta X_{pc} := X_{1,\,pc} - X_{0,\,pc}$ $\text{LR}_{pc} := \left|\frac{\text{LIN}_{1,\,pc} - \text{LIN}_{0,\,pc}}{\text{AREA}_{0}}\right|$ $\text{slope}_{pc} := \frac{\text{LIN}_{1,\,pc} - \text{LIN}_{0,\,pc}}{X_{1,\,pc} - X_{0,\,pc}}\cdot\frac{1}{\text{AREA}_{0}}$

Maximum reflectivity: 70%   Maximum area: $\mathrm{AREA}_0 = 20.899$

$$X^T = \begin{bmatrix} 0.3137 & 0.6331 \\ 0.273 & 0.6738 \\ 0.1975 & 0.7435 \\ 0.1278 & 0.8016 \end{bmatrix} \quad \mathrm{LIN}^T = \begin{bmatrix} 16.4347 & 7.7676 \\ 17.4119 & 6.752 \\ 18.9848 & 5.1513 \\ 20.0714 & 3.9775 \end{bmatrix} \quad \Delta X = \begin{bmatrix} 0.3195 \\ 0.4008 \\ 0.546 \\ 0.6738 \end{bmatrix} \quad \mathrm{LR} = \begin{bmatrix} 41.471 \\ 51.007 \\ 66.192 \\ 77.008 \end{bmatrix} \cdot\% \quad \mathrm{slope} = \begin{bmatrix} -1.298 \\ -1.273 \\ -1.212 \\ -1.143 \end{bmatrix}$$

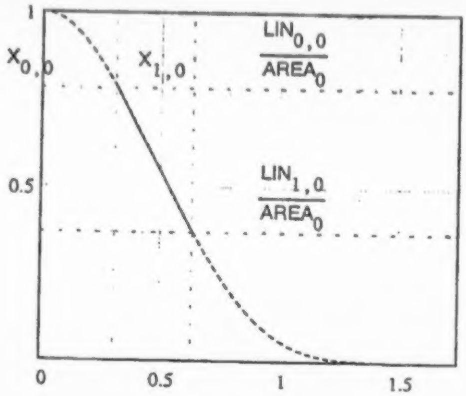

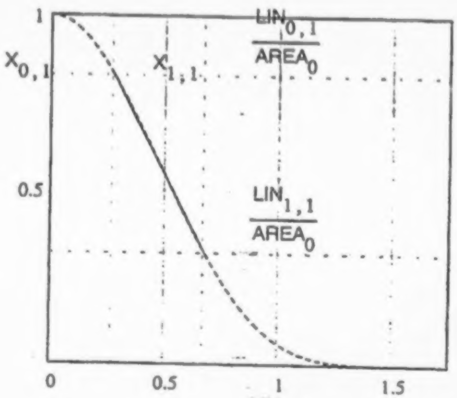

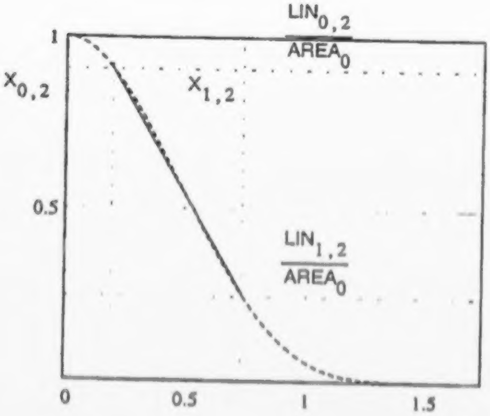

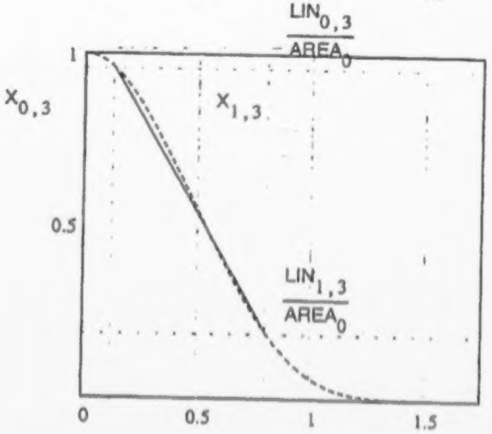

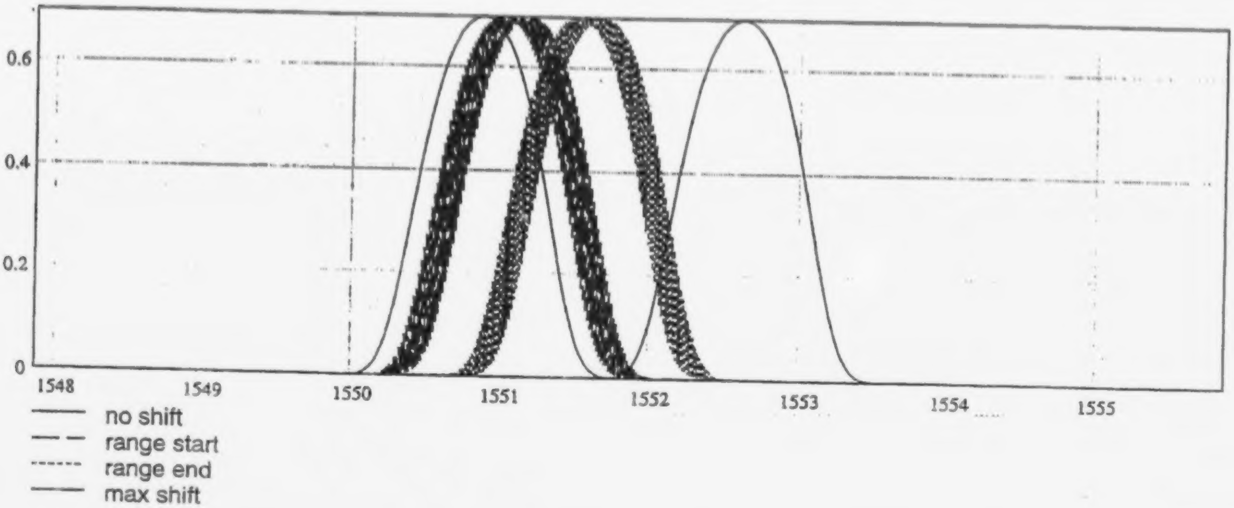

Non-apodized case

Bragg parameters:

Length of the reflector: $L_B := 1.0 \cdot mm$

Bragg parameters vector: $Bp := Bparms(L_B, n, \Delta n, \Lambda_0, \theta, p)$

$q1 := 0 .. 5$ $\quad B1p_{q1,q0} := Bp_{q1}$ $\quad B1p_{3,q0} := \Lambda_0 + q0 \cdot (\delta\lambda)$

Calculation parameters:

Wavelength step number: $\lambda b_{nbr} := 500$ Number of integration steps: $bstep\_nbr := 19$

Wavelength index: $jb := 0 .. \lambda b_{nbr}$ Step index: $ib := 0 .. bstep\_nbr$

Center wavelength: $\lambda_0 := BBreswavel(Bp, 200, 10^{-18})$ $\quad \lambda_0 = 1550.8637 \cdot nm$ $\quad \lambda t_0 := \lambda_0$

Maximum coupling factor: $M\kappa L := BBkappal(Bp, \lambda t)$ $\quad M\kappa L = 1.211$

Maximum reflectivity: $R_{max} := \tanh(|M\kappa L|)^2$ $\quad R_{max} = 70.05 \cdot \%$

Bandwith at Half Maximum: $BB_{bw} := BBfwhm(Bp, \lambda_0)$ $\quad BB_{bw} = 0.8282 \cdot nm$

$$\lambda b_{jb} := \left(\lambda_0 - \frac{\lambda_{span}}{2}\right) + \frac{\lambda_{span}}{\lambda b_{nbr}} \cdot jb + \lambda_{offset} \qquad \lambda 1_{q0} := \left(BBreswavel\left(B1p^{<q0>}, 200, 10^{-18}\right) - \lambda_0\right) \cdot 10^9$$

Calculations:

$$BR1^{<q0>} := BBreflectivity\left(B1p^{<q0>}, \lambda b\right) \qquad NAREA_{q0} := \left[\sum_{q2=0}^{\lambda b_{nbr}} \left[(BR1_{q2,q0}) \cdot (BR1_{q2,0})\right]\right]$$

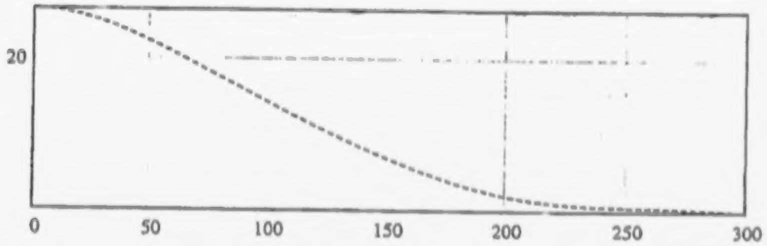

Search of linear region:

$data\%^{<0>} := data(0.005, center, NAREA, \lambda 1)$ $\quad data\%^{<1>} := data(0.01, center, NAREA, \lambda 1)$

$data\%^{<2>} := data(0.025, center, NAREA, \lambda 1)$ $\quad data\%^{<3>} := data(0.05, center, NAREA, \lambda 1)$

$$data\% = \begin{bmatrix} 49 & 41 & 27 & 14 \\ 122 & 133 & 153 & 171 \end{bmatrix}$$

$$NX_{0,pc} := \lambda 1_{(data\%_{0,pc})} \quad NX_{1,pc} := \lambda 1_{(data\%_{1,pc})} \quad NLIN_{0,pc} := NAREA_{(data\%_{0,pc})} \quad NLIN_{1,pc} := NAREA_{(data\%_{1,pc})}$$

$$\Delta X_{pc} := NX_{1,pc} - NX_{0,pc} \qquad LR_{pc} := \left|\frac{NLIN_{1,pc} - NLIN_{0,pc}}{NAREA_0}\right| \qquad slope_{pc} := \frac{NLIN_{1,pc} - NLIN_{0,pc}}{NX_{1,pc} - NX_{0,pc}} \cdot \frac{1}{NAREA_0}$$

Maximum reflectivity: 70% Maximum area: $NAREA_0 = 25.803$

$$NX^T = \begin{bmatrix} 0.2846 & 0.7086 \\ 0.2381 & 0.7725 \\ 0.1568 & 0.8887 \\ 0.0813 & 0.9932 \end{bmatrix} \quad NLIN^T = \begin{bmatrix} 22.2108 & 11.6926 \\ 23.1962 & 10.2369 \\ 24.6148 & 7.8095 \\ 25.4738 & 5.9389 \end{bmatrix} \quad \Delta X = \begin{bmatrix} 0.424 \\ 0.5344 \\ 0.7319 \\ 0.9119 \end{bmatrix} \quad LR = \begin{bmatrix} 40.764 \\ 50.225 \\ 65.13 \\ 75.709 \end{bmatrix} \cdot \% \quad slope = \begin{bmatrix} -0.961 \\ -0.94 \\ -0.89 \\ -0.83 \end{bmatrix}$$

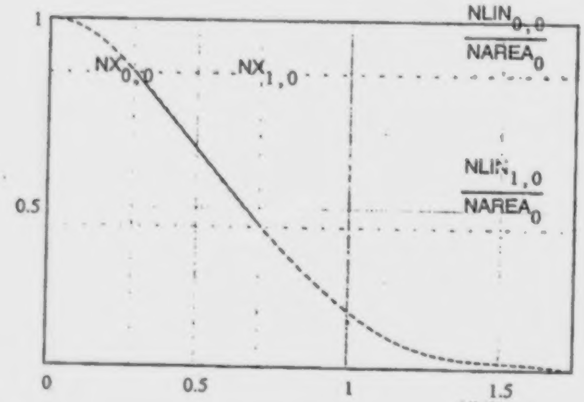

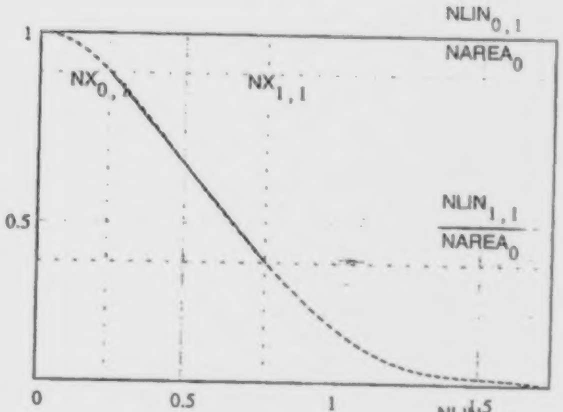

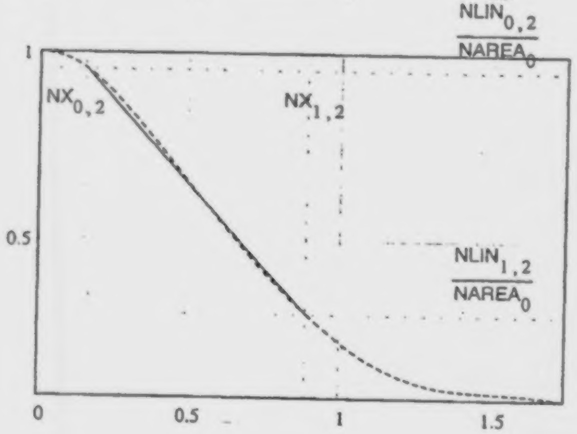

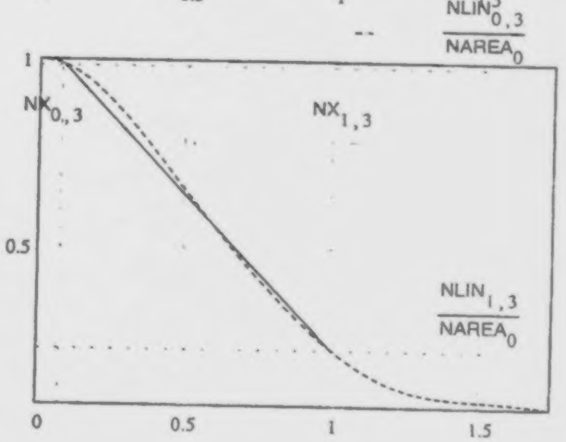

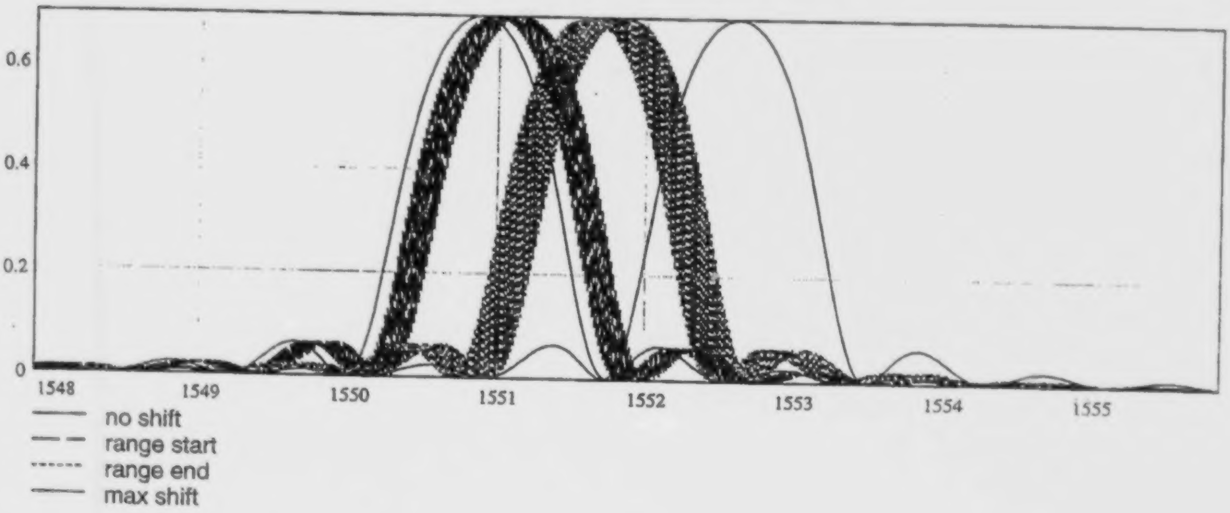

Comparison between Apodized and Non-Apodized cases at R=70%

Error percentage: $i := 2$ Value: i=0 1%, i=1 2%, i=2 5%, i=3 10%

Normalization value: $Ymax := NAREA_0$

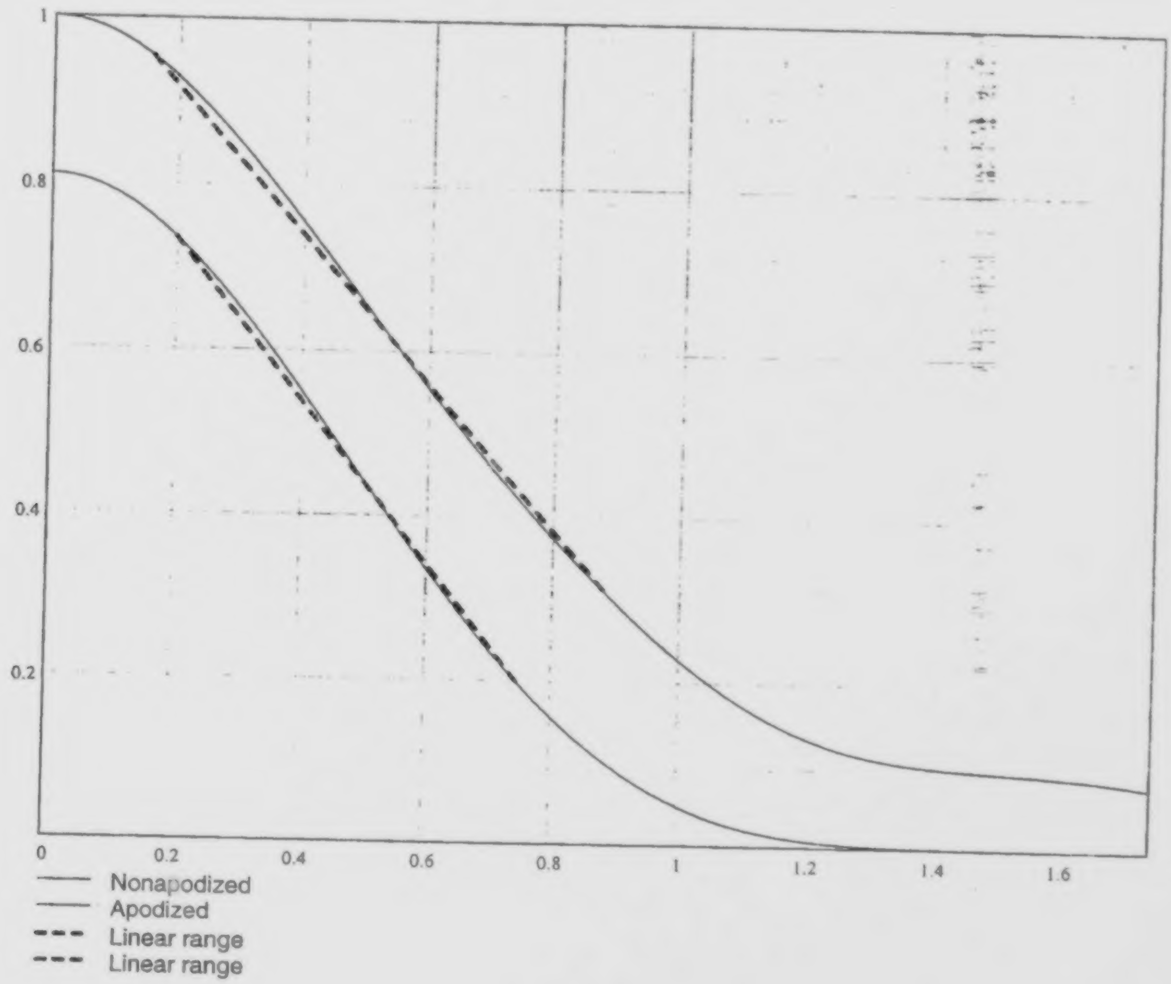

Files

$APOMATRIX_{q0,0} := \lambda 1_{q0}$ $NAPOMATRIX_{q0,0} := \lambda 1_{q0}$

$APOMATRIX_{q0,1} := \frac{AREA_{q0}}{Ymax}$ $NAPOMATRIX_{q0,1} := \frac{NAREA_{q0}}{Ymax}$

WRITEPRN("rrapo.prn") := APOMATRIWRITEPRN("rrnapo.prn") := NAPOMATRIX

Bragg Calculations Program, Version 3.0

(ST1997)

Purpose: Linearity test for the correlation between two perfect Bragg gratings at different center wavelengths.
Comparison between Apodized and Non-Apodized at a reflectivity of 70%, case R*(1-R).

Units: $nm \equiv 10^{-9}$ $\mu m \equiv 10^{-6}$ $mm \equiv 10^{-3}$

Bragg parameters:

Average refraction index: $n := 1.45165$

Length of the reflector: $L_B := 2.0 \cdot mm$

Index variation: $\Delta n := 0.939 \cdot 10^{-3}$

Pitch: $\Lambda_0 := 0.534 \cdot \mu m$

Angle of incidence: $\theta := 0$

Order: $p := 1$

Bragg parameters vector: $Bp := Bparms(L_B, n, \Delta n, \Lambda_0, \theta, p)$

$factor := 3$

$qmax := 100 \cdot factor$ $q0 := 0 .. qmax$ $q1 := 0 .. 5$ $B1p_{q1,q0} := Bp_{q1}$ $\delta\lambda := \frac{0.006}{factor} \cdot nm$

$B1p_{3,q0} := \Lambda_0 + q0 \cdot (\delta\lambda)$

Calculation parameters:

Window span: $\lambda_{span} := 8 \cdot nm$

Window offset: $\lambda_{offset} := 1 \cdot nm$

Wavelength step number: $\lambda c_{nbr} := 500$

Number of integration steps: $cstep\_nbr := 41$

Wavelength index: $jc := 0 .. \lambda c_{nbr}$

Step index: $ic := 0 .. cstep\_nbr$

Z span: $z_{span} := L_B$

Z center: $z_{center} := 0.5 \cdot L_B$

Center wavelength: $\lambda_0 := BBreswavel(Bp, 200, 10^{-18})$ $\lambda_0 = 1550.8637 \cdot nm$ $\lambda t_0 := \lambda_0$

Maximum coupling factor: $M\kappa L := BBkappal(Bp, \lambda t)$ $M\kappa L = 2.422$

Maximum reflectivity: $R_{max} := \tanh(|M\kappa L|)^2$ $R_{max} = 96.898 \cdot \%$

Bandwith at Half Maximum: $BB_{bw} := BBfwhm(Bp, \lambda_0)$ $BB_{bw} = 0.4141 \cdot nm$

Validation bandwith: $CB_{bw} := \frac{\Lambda_0}{p} \cdot \frac{\lambda_0}{L_B} \cdot cstep\_nbr$ $CB_{bw} = 16.977 \cdot nm$

$$\lambda c_{jc} := \left(\lambda_0 - \frac{\lambda_{span}}{2}\right) + \frac{\lambda_{span}}{\lambda c_{nbr}} \cdot jc + \lambda_{offset} \qquad \lambda 1_{q0} := \left(BBreswavel\left(B1p^{\langle q0 \rangle}, 200, 10^{-18}\right) - \lambda_0\right) \cdot 10^9$$

$$h_c := \frac{L_B}{cstep\_nbr} \qquad zc_{ic} := h_c \cdot ic \qquad zrc_{ic} := if\left[\left[\left(zc_{ic} \le z_{center} + \frac{z_{span}}{2}\right) \cdot \left(zc_{ic} \ge z_{center} - \frac{z_{span}}{2}\right)\right], zc_{ic}, -1\right]$$

Non-apodized case

Bragg parameters:

Length of the reflector: $L_B := 1.0 \cdot mm$

Bragg parameters vector: $Bp := Bparms\left(L_B, n, \Delta n, \Lambda_0, \theta, p\right)$

$q1 := 0..5$ $\quad B1p_{q1,q0} := Bp_{q1}$ $\quad B1p_{3,q0} := \Lambda_0 + q0 \cdot (\delta\lambda)$

Calculation parameters:

Wavelength step number: $\lambda b_{nbr} := 500$ $\quad$ Number of integration steps: $bstep\_nbr := 19$

Wavelength index: $jb := 0..\lambda b_{nbr}$ $\quad$ Step index: $ib := 0..bstep\_nbr$

Center wavelength: $\lambda_0 := BBreswavel\left(Bp, 200, 10^{-18}\right)$ $\quad \lambda_0 = 1550.8637 \cdot nm$ $\quad \lambda t_0 := \lambda_0$

Maximum coupling factor: $M\kappa L := BBkappal(Bp, \lambda t)$ $\quad M\kappa L = 1.211$

Maximum reflectivity: $R_{max} := \tanh(|M\kappa L|)^2$ $\quad R_{max} = 70.05 \cdot \%$

Bandwith at Half Maximum: $BB_{bw} := BBfwhm\left(Bp, \lambda_0\right)$ $\quad BB_{bw} = 0.8282 \cdot nm$

$$\lambda b_{jb} := \left(\lambda_0 - \frac{\lambda_{span}}{2}\right) + \frac{\lambda_{span}}{\lambda b_{nbr}} \cdot jb + \lambda_{offset} \qquad \lambda 1_{q0} := \left(BBreswavel\left(B1p^{<q0>}, 200, 10^{-18}\right) - \lambda_0\right) \cdot 10^9$$

Calculations:

$$BR1^{<q0>} := BBreflectivity\left(B1p^{<q0>}, \lambda b\right) \qquad NAREA_{q0} := \left[\sum_{q2=0}^{\lambda b_{nbr}} \left[\left(BR1_{q2,q0}\right) \cdot \left(1 - BR1_{q2,0}\right)\right]\right]$$

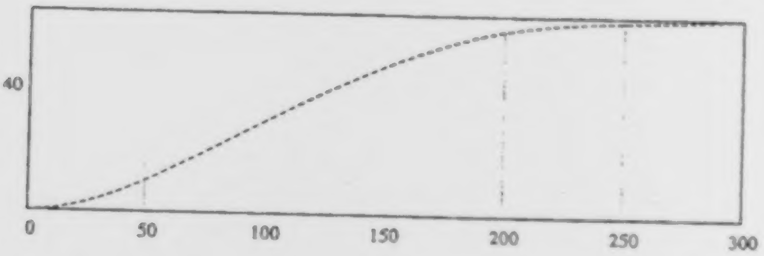

Search of linear region:

$data\%^{<0>} := data(0.005, center, NAREA, \lambda 1)$ $\quad data\%^{<1>} := data(0.01, center, NAREA, \lambda 1)$

$data\%^{<2>} := data(0.025, center, NAREA, \lambda 1)$ $\quad data\%^{<3>} := data(0.05, center, NAREA, \lambda 1)$

$$data\% = \begin{bmatrix} 44 & 35 & 20 & 4 \\ 142 & 159 & 187 & 217 \end{bmatrix}$$

$NAREA_{qmax} - NAREA_0$

$NX_{0,pc} := \lambda 1_{\left(data\%_{0,pc}\right)}$ $\quad NX_{1,pc} := \lambda 1_{\left(data\%_{1,pc}\right)}$ $\quad NLIN_{0,pc} := NAREA_{\left(data\%_{0,pc}\right)}$ $\quad NLIN_{1,pc} := NAREA_{\left(data\%_{1,pc}\right)}$

$$\Delta X_{pc} := NX_{1,pc} - NX_{0,pc} \qquad LR_{pc} := \left|\frac{NLIN_{1,pc} - NLIN_{0,pc}}{25.8}\right| \qquad slope_{pc} := \frac{NLIN_{1,pc} - NLIN_{0,pc}}{NX_{1,pc} - NX_{0,pc}} \cdot \frac{1}{NAREA_0}$$

Maximum reflectivity: 70%   Maximum area: $NAREA_{qmax} = 48.899$ $NAREA_0 = 24.988$

$$NX^T = \begin{bmatrix} 0.2556 & 0.8248 \\ 0.2033 & 0.9235 \\ 0.1162 & 1.0862 \\ 0.0232 & 1.2604 \end{bmatrix} \quad NLIN^T = \begin{bmatrix} 28.0148 & 41.7911 \\ 26.9993 & 43.7793 \\ 25.7062 & 46.3254 \\ 25.0293 & 47.83 \end{bmatrix} \quad \Delta X = \begin{bmatrix} 0.5692 \\ 0.7203 \\ 0.97 \\ 1.2372 \end{bmatrix} \quad LR = \begin{bmatrix} 53.397 \\ 65.038 \\ 79.919 \\ 88.375 \end{bmatrix} \cdot \% \quad slope = \begin{bmatrix} 0.969 \\ 0.932 \\ 0.851 \\ 0.738 \end{bmatrix}$$

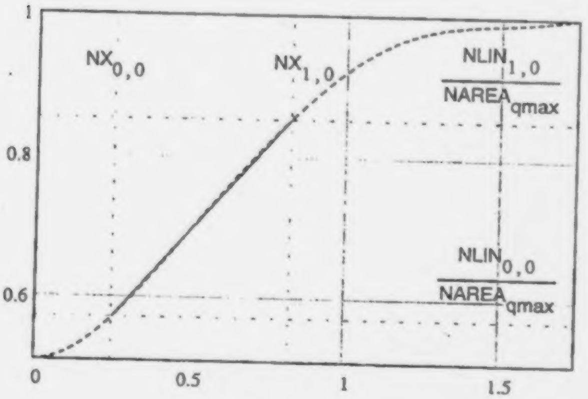

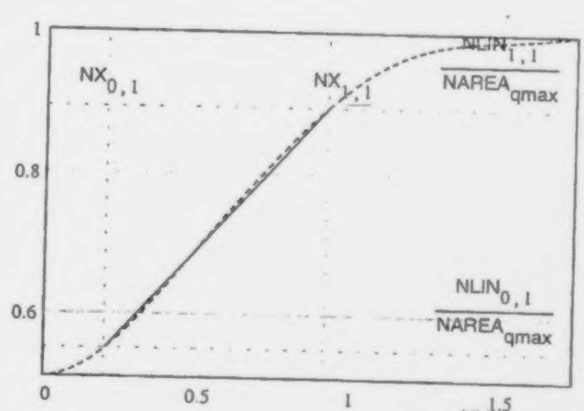

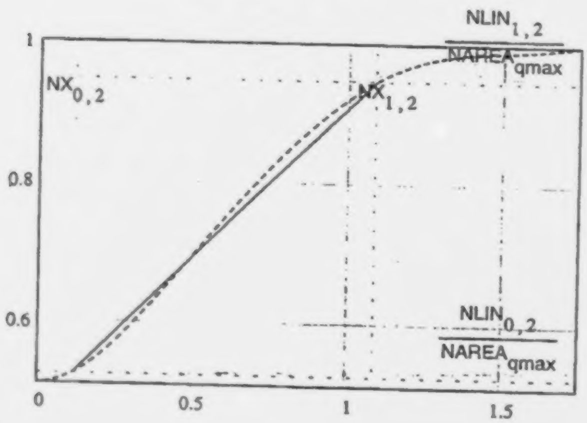

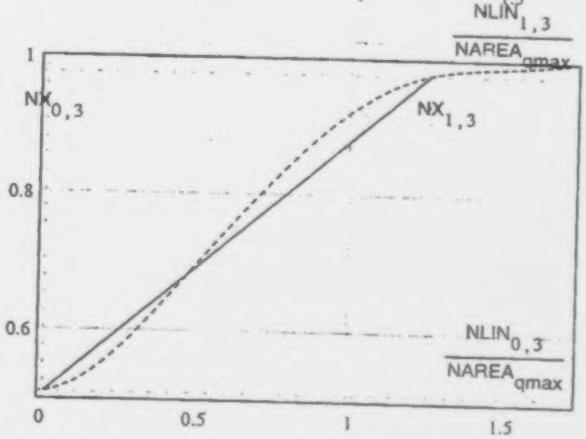

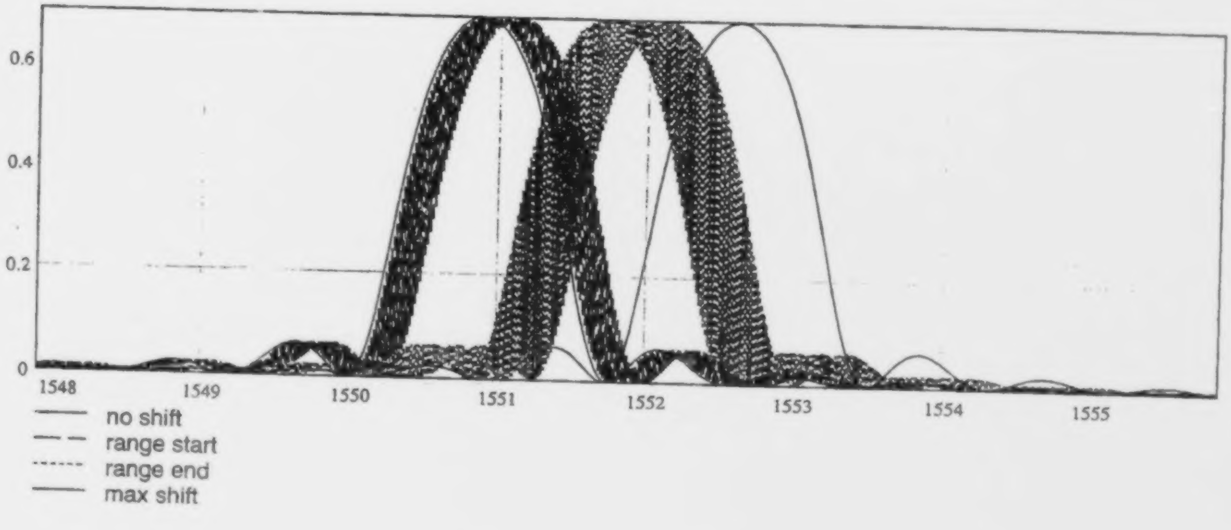

Comparison between Apodized and Non-Apodized cases at R=70%

Error percentage: $i := 2$ Value: i=0 1%, i=1 2%, i=2 5%, i=3 10%

Normalization value: $Ymax := 50$

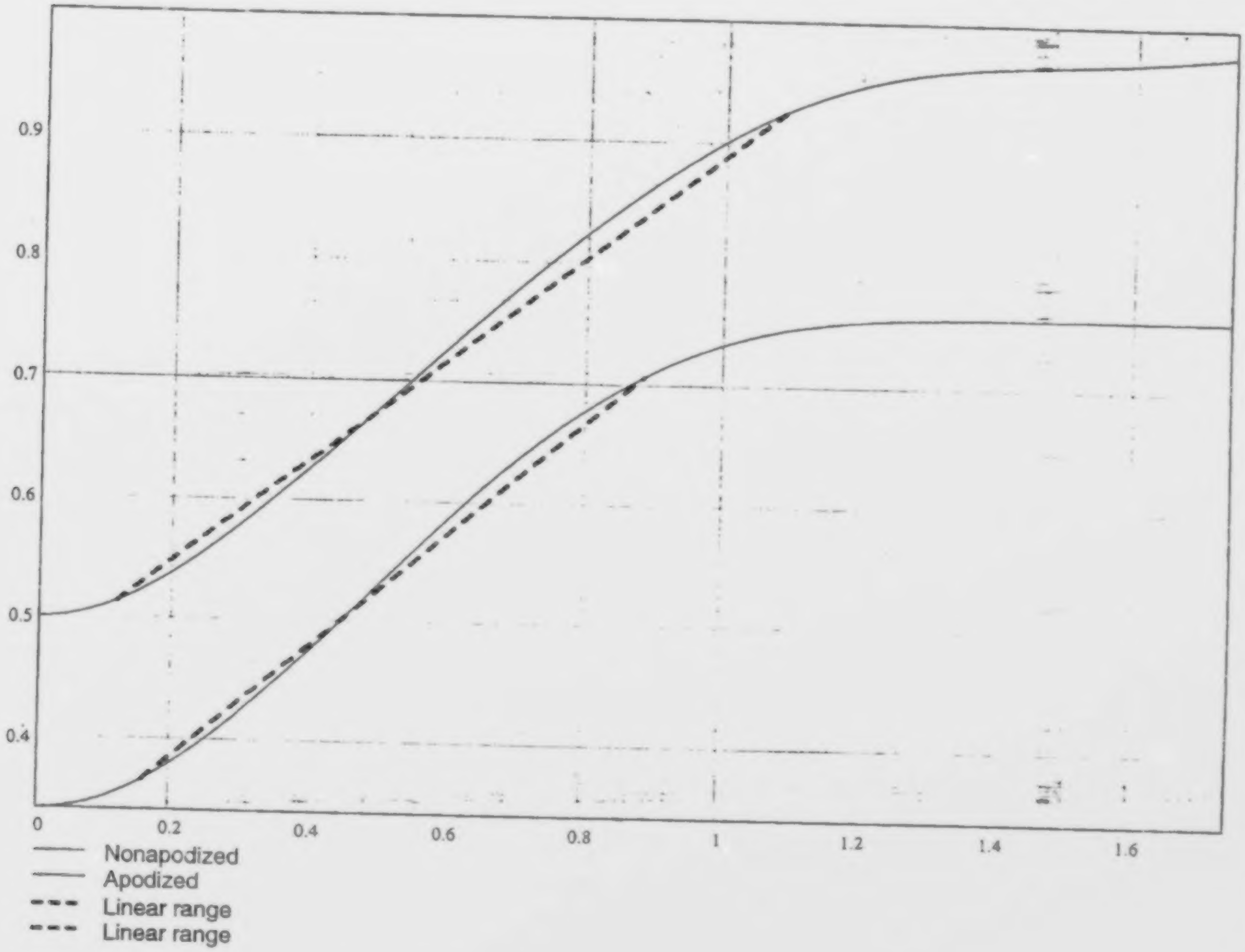

Files

$APOMATRIX_{q0,0} := \lambda 1_{q0}$ $NAPOMATRIX_{q0,0} := \lambda 1_{q0}$

$APOMATRIX_{q0,1} := \frac{AREA_{q0}}{Ymax}$ $NAPOMATRIX_{q0,1} := \frac{NAREA_{q0}}{Ymax}$

WRITEPRN("r1rapo.prn") := APOMATR WRITEPRN("r1rnapo.prn") := NAPOMATRIX

Appendix H

Specifications

The specifications of the electrical and optical components are included in the following pages.

FINAL DC LI TEST at 25°C

3925
COMM RES CTR

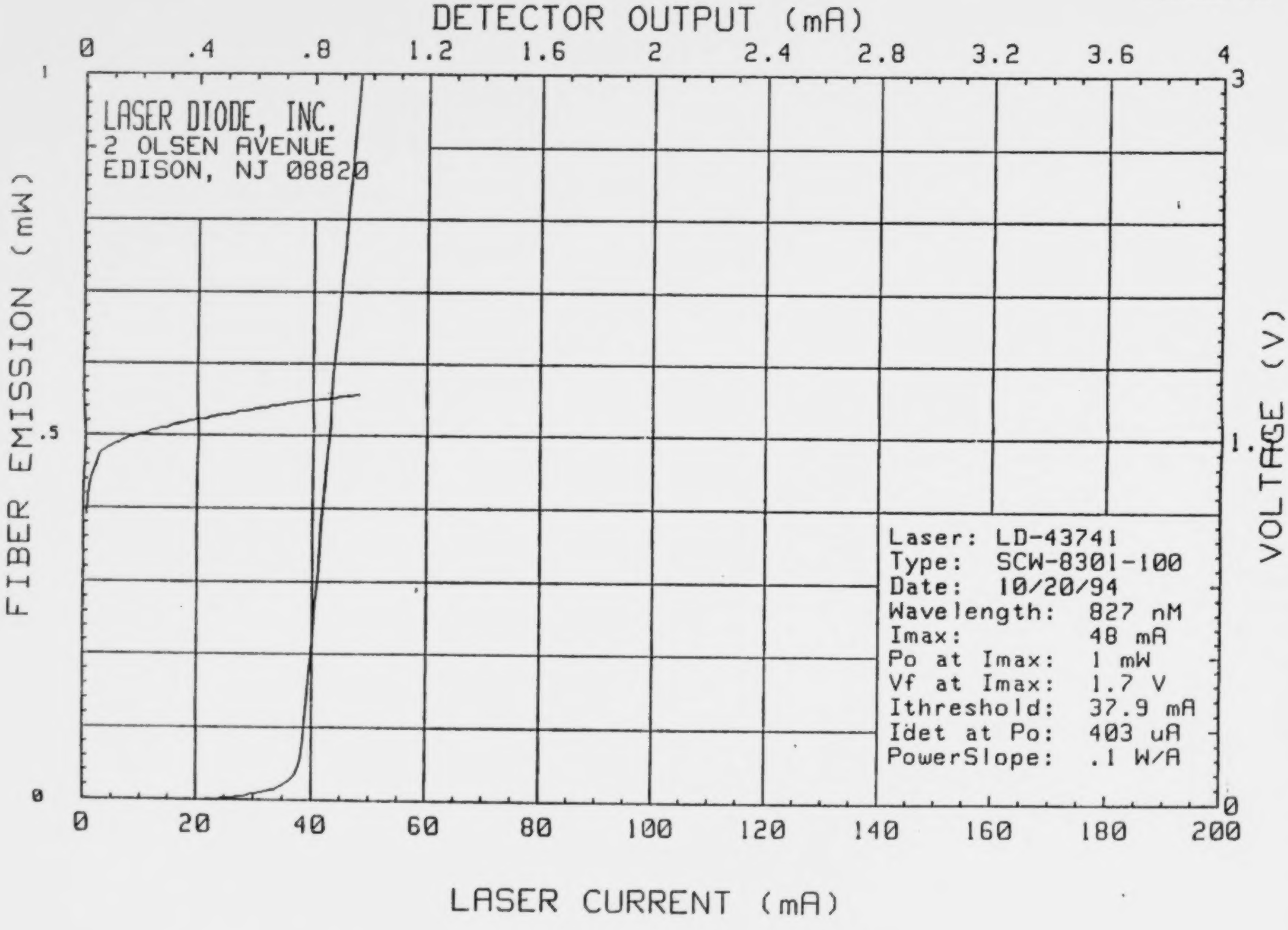

Laser: LD-43741
Type: SCW-8301-100
Date: 10/20/94
Wavelength: 827 nM
Imax: 48 mA
Po at Imax: 1 mW
Vf at Imax: 1.7 V
Ithreshold: 37.9 mA
Idet at Po: 403 uA
PowerSlope: .1 W/A

PIN DIAGRAM FOR DEVICE WITH COOLER AND FLOATING THERMISTOR

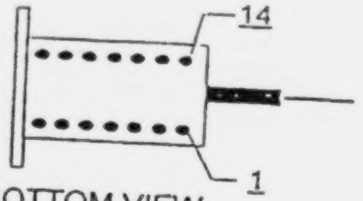

BOTTOM VIEW

PIN #	FUNCTION
1	COOLER ANODE(+)
2	NC
3	NC
4	NC
5	DEVICE ANODE, CASE
6	NC
7	DETECTOR CATHODE(-) (LASER PACKAGES ON
8	DETECTOR ANODE(+) (LASER PACKAGES ONLY
9	DEVICE CATHODE(-)
10	CASE
11	THERMISTOR
12	THERMISTOR
13	NC
14	COOLER CATHODE(-)

WARNING

Manufactured with CFC-113, a substance which harms public health and environment by destroying ozone in the upper atmosphere.

CAUTION ! HANDLE THE ENCLOSED DEVICE WITH EXTREME CARE. GLASS FIBER IS SUBJECT TO BREAKAGE IF MISHANDLED, AND PERMANENT DAMAGE TO THE DEVICE MAY RESULT. DO NOT HOLD THIS DEVICE BY THE FIBER OR THE COLOR CODED SLEEVE. DO NOT ATTEMPT TO COIL THE FIBER INTO A LOOP OF LESS THAN 7CM IN DIAMETER.

WARNING ! THIS DEVICE CONTAINS VARIOUS COMPONENTS WHICH COULD BE DAMAGED BY STATIC CHARGE. OBSERVE EVERY PRECAUTION TO AVOID ELECTRICAL DISCHARGE TO THE PINS OF THE DEVICE.

WARNING ! EXCESSIVE HEATING OF THE DEVICE WILL RESULT IN PERMANENT DAMAGE TO THE INTERNAL ELECTRICAL COMPONENTS. SOLDERING OF THE PINS SHOULD BE PERFORMED IN A CAREFUL MANNER.

WARNING ! THIS DEVICE CONTAINS A THERMOELECTRIC COOLER. FAILURE TO POWER THE THERMOELECTRIC COOLER WHEN OPERATING THIS DEVICE WILL RESULT IN PERMANENT DAMAGE TO THE DEVICE. THIS DEVICE MUST ALWAYS BE ATTACHED TO A HEAT SINK DURING OPERATION.

ANY OF THE ABOVE ACTIONS MAY VOID THE WARRANTY

RCA

SILICON AVALANCHE PHOTODIODE

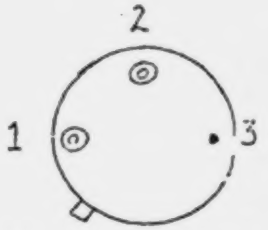

PIN 1 - NEGATIVE
PIN 2 - POSITIVE
PIN 3 - CASE

C30817
C30884
C30895

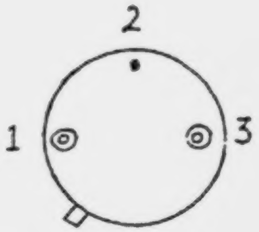

PIN 1 - NEGATIVE
PIN 2 - CASE
PIN 3 - POSITIVE

C30872, C30903E
C30904E, C30905E
C30906E, C30907E
C30908E

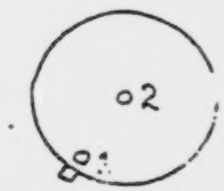

PIN 1 - NEGATIVE
PIN 2 - POSITIVE

C30902E

TYPE: C30908E

SERIAL NO: 0992

* TEST DATA AT 22°C

OPERATING VOLTAGE 207 VOLTS
BREAKDOWN VOLTAGE 213 VOLTS
DARK CURRENT 11 NANO AMPS
RESPONSIVITY 77 AMPS/WATT AT 830 NM
NOISE CURRENT $< 2 \times 10^{-13}$ AMPS/$HZ^{\frac{1}{2}}$
RISETIME < .5 NANOSECONDS

* FOR TYPES C30903E THROUGH C30908E THE OPTICAL MEASUREMENTS ARE REFERRED TO RADIATION FALLING ON THE INPUT OF THE LIGHT PIPE.

DATE: 3rd Mar '78

Optics For Research
FiberBench Test Data Sheet

015

Customer: Communications Research Center

Reference: PO# 519HA-67CRC-4-1867

Date Assembled: 10/04/94

Reference: SO# 10985

FiberBench Part Number: IO-ITS-FFB-820-X
Serial Number: 088

Experimental Test Data:
- Test Wavelength: 830nm
- Insertion Loss (dB) (Fiber to Fiber): 1.52
- Isolation (dB): 35.0
- Polarization Dependent Loss (dB): <+/- .05
- Return Loss (dB)-
  - Input Fiber: 60dB
  - Output Fiber: 60dB

Optical Specifications:
- Faraday Rotator: TGG
- Retarder Element: Crystal Quartz (Zero-Order)
- Polarization Splitters: Calcite Walk-Off blocks

Fiber Specifications:
- Type: SM Step Index
- Manufacturer: Corning
- Part Number: Flexcore 850
- Length (m): 1.0 (On each End)
- Fiber Buffer/Cable Diameter: 3000um Yellow PVC
- Connectors Supplied (Attaches to PAF): Diamond FC/APC-A
- Optional Connectors (Distal Ends): None

Assembled and Tested By: RM

Special Notes:

1) When inserting the FC/APC-A connectors, you must match up the connector labeled #1 with the FiberPort labeled #1 and so on. When this assembly was aligned, the fibers were matched to the FiberPort assemblies for optimal transmission and minimal insertion loss. If you do not use the fiber pigtails in this way, higher insertion losses will result.

2) The very tip of each FC/APC-A connector supplied has a multi-layer AR coating deposited directly onto it for use at 820nm. This coating can be fragile, so please be

careful when inserting the connectors into the Fiberports. They are shipped with protective boots and should require no additional cleaning.

3) The above system has been aligned and tested at 830nm. We do recognize that you may wish to use the device at other wavelengths (ie @ 820.0nm) This isolator assembly should function very well at 830nm as the performance indicates above and also at 820.0nm.

It may be necessary to tune the isolator for maximum isolation by rotating the finely knurled retarder ring on the assembly. This is most easily done by launching light in the reverse direction through the isolator assembly and fine tweeking the retarder wheel for minimum transmission.

Once this is complete, turn the isolator around again and use it in the forward direction in its normal mode of operation.

4) The enclosed FiberBench system has been thoroughly checked out just prior to shipment. If you have any discrepancies with the above performance data, you must contact OFR immediately at:

Optics For Research
PO Box 82
315 Bloomfield Ave.
Caldwell, NJ 07006-0082

Ph: (201) 228-4480
Fx: -0915

Any discrepancies or concerns must be reported within 30 days of receipt in order to be fully covered under our warrantee program.

LT015PD

Features

- High output (maximum optical power output: 40 mW)
- Wavelength: 830nm
- Single transverse mode

Applications

- Optical disk memories
- Medical apparatus
- Optical floppy disks
- Optical memory cards
- Information processing equipment

SHARP
LT015PD

Absolute Maximum Ratings

(Tc=25°C)

Parameter		Symbol	Ratings	Units
Optical power output		Po	40	mW
Reverse voltage	Laser	V_R	2	V
	PIN		30	
Operating temperature *1		Topr	−10~+50	°C
Storage temperature *1		Tstg	−40~+35	°C
Soldering temperature *2		Tsol	260 (less than 5 seconds)	°C

*1 Case temperature *2 At point 1.5 mm from lead base

Electro-optical Characteristics *1

(Tc=25°C)

Parameter			Symbol	Condition	MIN	TYP	MAX	Units
Threshold current			Ith	—	—	60	80	mA
Operating current			Iop	Po=30mW	—	95	130	mA
Operating voltage			Vop	Po=30mW	—	1.75	2.2	V
Wavelength *2			λp	Po=30mW	815	830	845	nm
Monitor current			Im	Po=30mW V_R=15V	30	100	380	μA
Radiation characteristics	Angle *3	Parallel to junction	θ∥	Po=30mW	8	9.5	14	deg
		Perpendicular to junction	θ⊥	Po=30mW	20	27	38	deg
	Ripple			Po=30mW	—	—	±20	%
Emission point accuracy	Angle		Δφ∥	Po=30mW	—	—	±2	deg
			Δφ⊥	Po=30mW	—	—	±3	deg
	Position		Δx, Δy, Δz	—	—	—	±80	μm
Differential efficiency			η	$\frac{20\text{mW}}{I(30\text{mW})-I(10\text{mW})}$	0.5	0.8	1.1	mW/mA

*1 Initial value
*2 Single transverse mode
*3 Angle at 50% peak intensity (full width at half-maximum)

Electrical Characteristics of Photodiode

(Tc=25°C)

Parameter	Symbol	Condition	MIN	TYP	MAX	Units
Sensitivity	S	V_R=15V	—	3.3	—	[illegible]
Dark current	I_D	V_R=15V		—	150	[illegible]
Terminal capacitance	Ct	V_R=15V		18	30	[illegible]

LT015 Series Characteristics Diagrams

Fig. 90-1 Forward Current vs. Forward Voltage

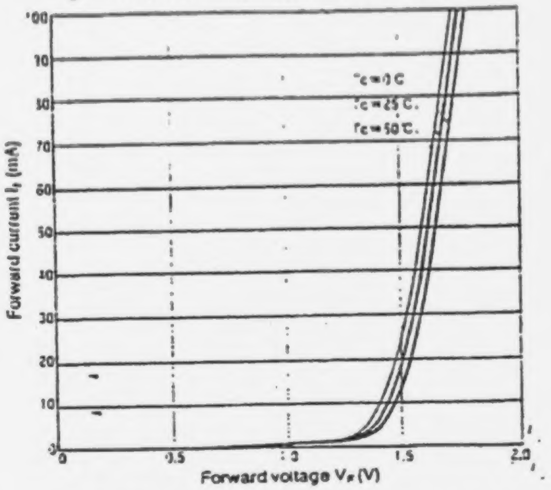

Fig. 90-2 Optical Power Output vs. Forward Current and Monitor Current

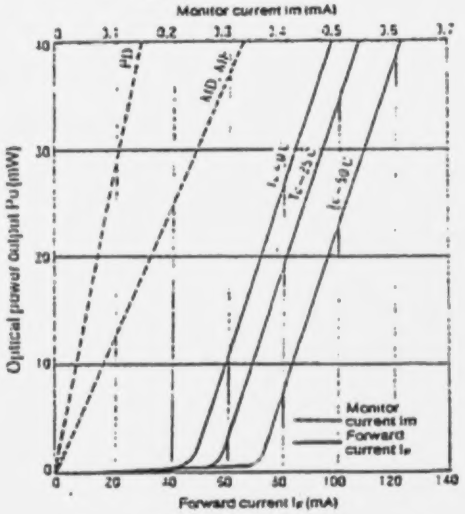

Fig. 90-3 Threshold Current vs. Temperature

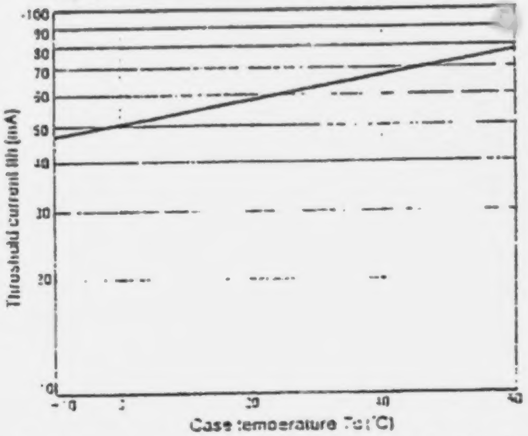

Fig. 90-4 Wavelength vs. Temperature

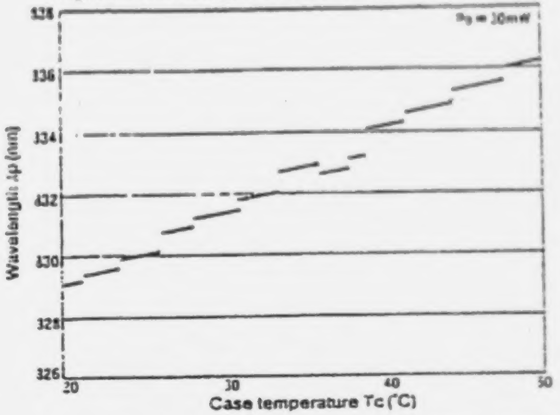

Fig. 90-5 Optical Power Output Dependence of Wavelength

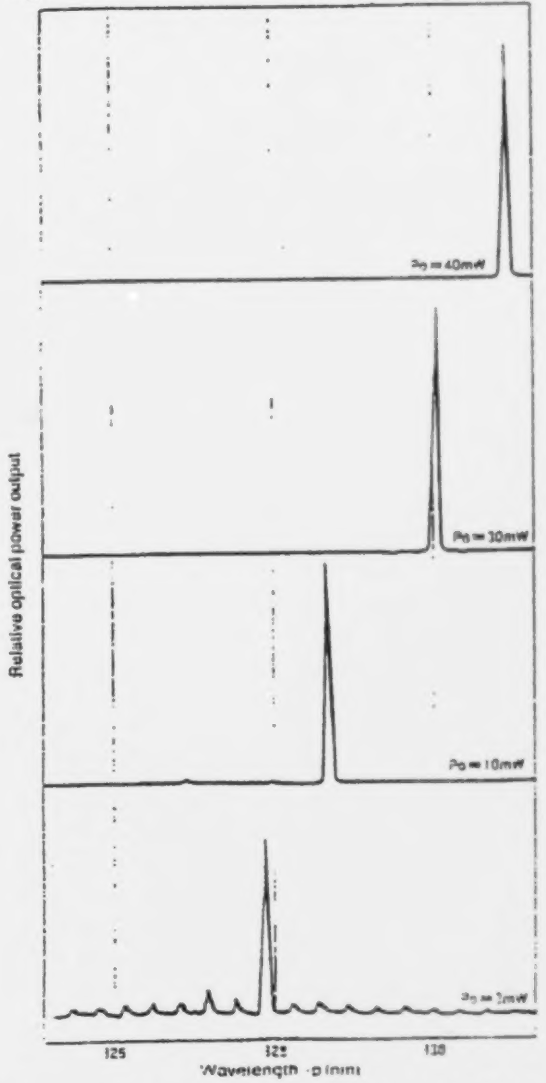

Note: All data on this page [illegible]

LD.PINOUTS

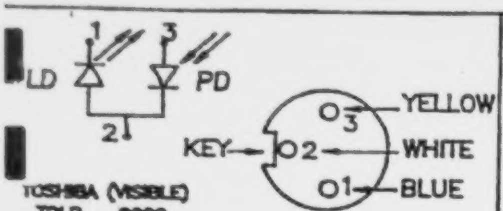
1
3
LD
PD
2
YELLOW
3
KEY
2
WHITE
1
BLUE

TOSHIBA (VISIBLE)
TOLD 9200
TOLD 9201
TOLD 9211
TOLD 9215
TOLD 9220

SPECTRA DIODE LABS (INFRARED)
SDL 5400
SDL 5401
SDL 5410
SDL 5411

PHILIPS (VISIBLE)
CQL 80

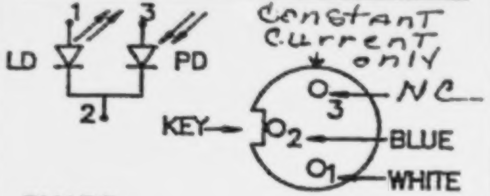
1
3
LD
PD
2
constant current only
3
NC
KEY
2
BLUE
1
WHITE

SHARP
LT020MC (INFRARED)

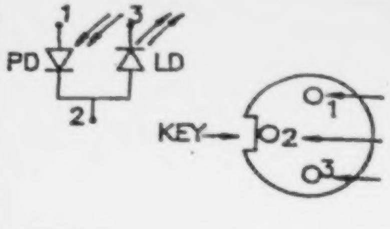
1
3
PD
LD
2
1
KEY
2
3

HITACHI
HL6711G (VISIBLE)

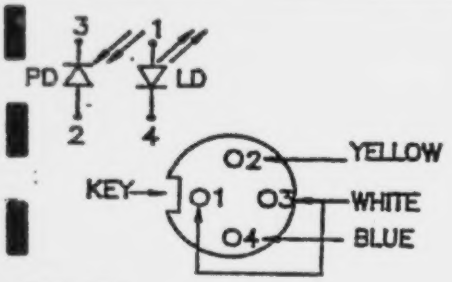
3
1
PD
LD
2
4
2
YELLOW
KEY
1
3
WHITE
4
BLUE

PHILIPS
CQL60 (INFRARED)

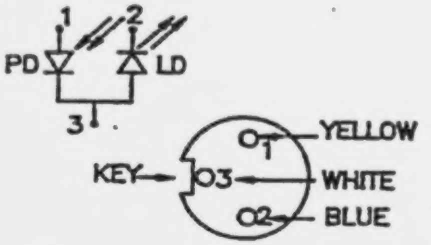
1
2
PD
LD
3
1
YELLOW
KEY
3
WHITE
2
BLUE

NEC
NDL 3200 (VISIBLE)

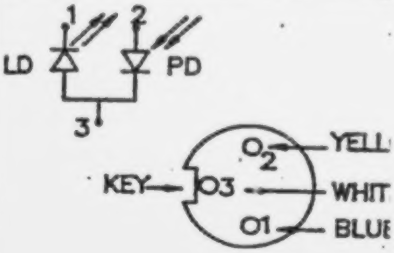
1
2
LD
PD
3
2
YELL
KEY
3
WHIT
1
BLUE

SONY
SLD 151 (VISIBLE)

Power Technology Inc.

Power Technology
Incorporated
Address Correspondence To Box [illegible] Little Rock, Arkansas 7
Plant Location 7925 Mabelvale Cutoff Mabelvale Arkansas
501-568-1993 FAX: 501-568-1994

TE: THERE IS NO STANDARD FOR PINOUT. NUMBERS MAY COUNT CLOCKWISE OR COUNTERCLOCKWISE.
RMATION TAKEN FROM MANUFACTURERS DATA SHEETS. BOTTOM VIEW OF LASERS

REVISIONS				
REV.	DATE	DRAWN	APPVD	DESCRIPTION

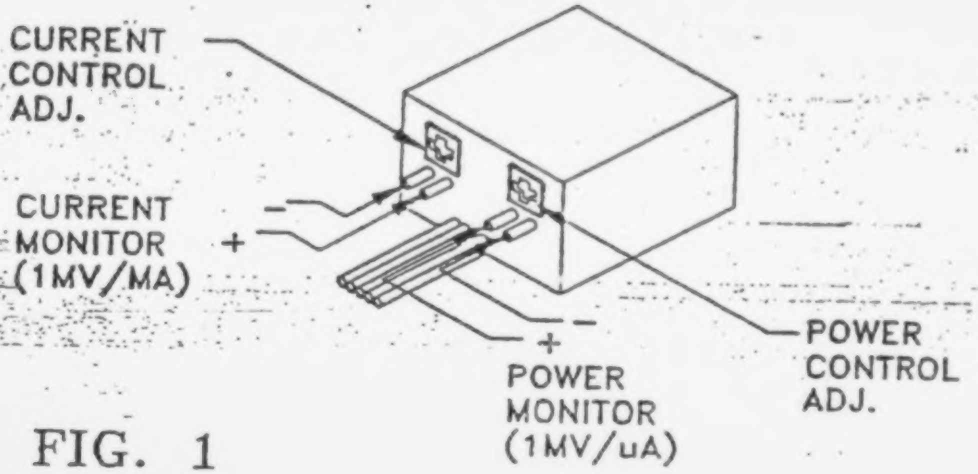
CURRENT CONTROL ADJ.
CURRENT MONITOR (1MV/MA)
−
+
−
+
POWER MONITOR (1MV/uA)
POWER CONTROL ADJ.

FIG. 1

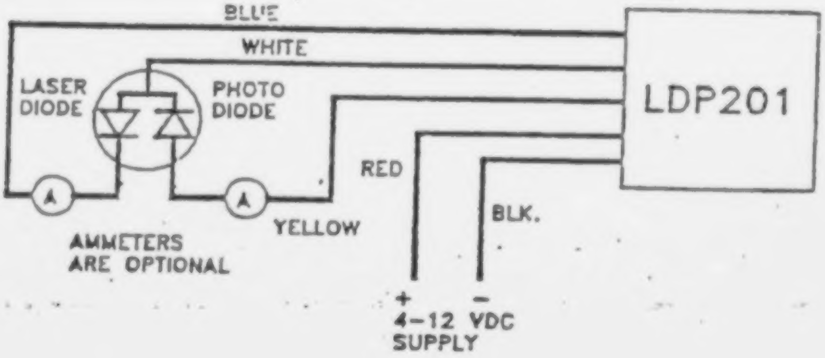
BLUE
WHITE
LASER DIODE
PHOTO DIODE
LDP201
RED
A
A
YELLOW
BLK.
AMMETERS ARE OPTIONAL
+
−
4-12 VDC SUPPLY

FIG. 2

MATERIAL

FINISH

Power Technology Inc.

Power Technology Incorporated
Address correspondence to: Box 9769 Little Rock, Arkar
Plant Location: 7925 Mabelvale Cutoff Mabelvale Arkan
501-568-1995 TWX910-722-7313

DO NOT SCALE THIS DWG
UNLESS OTHERWISE SPECIFIED
TOLERANCES SHALL BE AS FOLLOWS

DECIMAL
.XX
.XXX

FRACTIONAL

ANGULAR

DRAWN KC
DATE 2-23-90
CHECKED
ENGR
APPROVED

TITLE
INFORMATION DWG
LDP201

SCALE
SIZE

Part #: 500-02 Laser Diode Driver Cable

PIN#	DESCRIPTION	WIRE COLOR
1,2	INTERLOCK	FACTORY SHORTED
3	CHASSIS GND	SHIELD OR DRAIN WIRE
4,5	LASER CATHODE	BLACK
6	PD CATHODE	WHITE
7	PD ANODE	GREEN
8,9	LASER ANODE	RED

WARNING: This cable will not work with old Model 502 and Model 520 drivers. CONSULT FACTORY.

SERIES SMV

NEW SURFACE MOUNT DESI

Hi Voltage Hi Reliability Ultra-Miniature Isolated DC-DC Converters

.440" ht. up to 500V DC output

OPTIONS AVAILABLE
- Expanded operating temp (−55°C to +85°C)
- Stabilization Bake (125°C ambient)
- Temperature Cycle (−55°C to +125°C)
- Hi Temp, full power burn in (100% power, 125°C case temp)

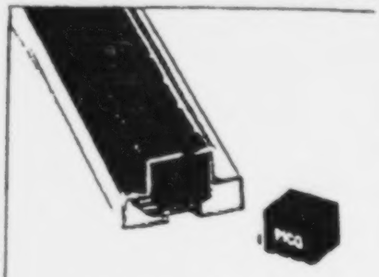

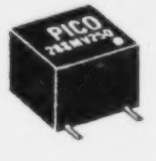

SURFACE MOUNT

**PICO surface mount units utilize m
rials and methods to withstand extr
temperature (220°C) of vapor phase,
and other reflow procedures without
radation of electrical or mechanical c
acteristics.**

TYPICAL CHARACTERISTICS:

Test conditions: 25°C ambient and input voltage at nominal value unless otherwise specified.

LINE REGULATION: OUTPUT IS DIRECTLY PROPORTIONAL TO THE INPUT

Input voltage range: ± 10% all models

Output voltage tolerance at full load-nom. Input: ± 3%
Please keep loaded to minimum of 10% at all times.
Note: For tighter output voltage tolerances, please consult factory.

Converter frequency: 20 – 40 KHz

Output temperature coefficient: 0.02%/°C for all models

Operating temperature: −25°C to + 70°C ambient. No heat sink.

Storage temperature: −55°C to + 125°C

Isolation: 100 megohms min. @ 1000V DC

SERIES SMV—SINGLE OUTPUT

PICO PART NUMBER	INPUT VOLTAGE (V DC)	OUTPUT VOLTAGE (V DC)	MAX LOAD CURRENT (mA)	MAX. OUTPUT POWER (watts)	EFF. @ FULL LOAD TYPICAL (%)	INPUT CURRENT FULL LOAD TYPICAL (mA)	OUTPUT VOLTAGE RIPPLE @ FULL LOAD (Vp-p max)	FULL** LOAD OUTPUT VOLTAGE TOLERANCE (%)
5SMV100	5	100	12.50	1.25	78	321	0.90	±3
5SMV150	5	150	8.30	1.25	76	329	0.90	±3
5SMV200	5	200	6.25	1.25	75	333	0.90	±3
5SMV250	5	250	5.00	1.25	75	333	0.90	±3
5SMV300	5	300	4.16	1.25	70	357	[illegible]	±3
5SMV350	5	350	3.57	1.25	70	357	1.20	±3
5SMV400	5	400	3.12	1.25	70	357	1.20	±3
5SMV450	5	450	2.77	1.25	70	357	1.50	±3
5SMV500	5	500	2.50	1.25	70	357	1.50	±3
12SMV100	12	100	12.50	1.25	80	130	0.90	±3
12SMV150	12	150	8.30	1.25	79	132	0.90	±3
12SMV200	12	200	6.25	1.25	78	134	0.90	±3
12SMV250	12	250	5.00	1.25	75	139	0.90	±3
12SMV300	12	300	4.16	1.25	75	139	1.20	±3
12SMV350	12	350	3.57	1.25	73	139	1.20	±3
12SMV400	12	400	3.12	1.25	75	139	[illegible]	±3
12SMV450	12	450	2.77	1.25	73	139	1.50	±3
12SMV500	12	500	2.50	1.25	75	139	1.50	±3
24SMV100	24	100	12.50	1.25	76	99	0.90	±3
24SMV150	24	150	8.30	1.25	73	71	0.90	±3
24SMV200	24	200	6.25	1.25	73	71	0.90	±3
24SMV250	24	250	5.00	1.25	70	74	0.90	±3
24SMV300	24	300	4.16	1.25	73	71	1.20	±3
24SMV350	24	350	3.57	1.25	73	71	1.20	±3
24SMV400	24	400	3.12	1.25	73	71	1.20	±3
24SMV450	24	450	2.77	1.25	73	71	1.50	±3
24SMV500	24	500	2.50	1.25	73	71	1.50	±3
28SMV100	28	100	12.50	1.25	75	60	0.90	±3
28SMV150	28	150	8.30	1.25	76	59	0.90	±3
28SMV200	28	200	6.25	1.25	75	60	0.90	±3
28SMV250	28	250	5.00	1.25	70	64	0.90	±3
28SMV300	28	300	4.16	1.25	73	61	1.20	±3
28SMV350	28	350	3.57	1.25	73	61	1.20	±3
28SMV400	28	400	3.12	1.25	73	61	1.20	±3
28SMV450	28	450	2.77	1.25	73	61	1.50	±3
28SMV500	28	500	2.50	1.25	73	61	1.50	±3

*Measured using 0.1µf, 1000 volt DC capacitor which is required across the output and maintain at least 10% of load at all times t
prevent voltage surge.

**For tighter tolerances consult factory

Ordering Instructions: No minimum. Net 30 days F.O.B. Mt. Vernon, New

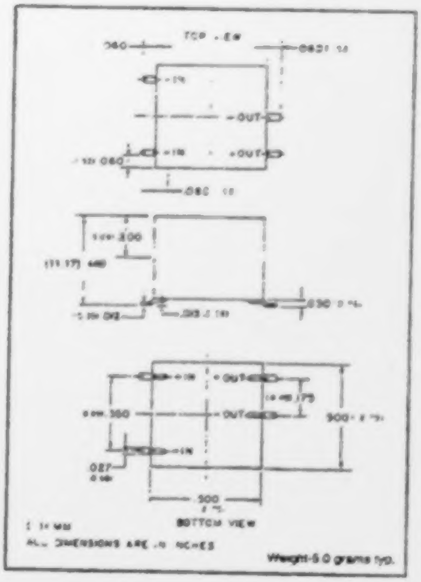

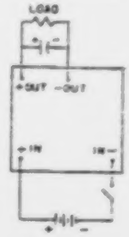

bottom view

FEATURES:

- New surface mount construction
- 1.25 watt output at 70° ambient
- Ultra-miniature size .440" height, 5.0 grams weight, 0.1 cubic inches volume
- 4 input voltage ranges 5, 12, 24 and 28 VDC
- 100 megohm @ 1000 VDC input/output isolation
- MIL-STD 883 options available
- No heat sink or electrical derating required

This series of unregulated high voltage DC-DC converters are produced in an ultra-miniature encapsulated package, now compatible with your surface mount assembly. 36 different models are available. These single output isolated units will operate over the temperature range of −25° to +70°C with no heat sink or electrical derating. For military applications an operating temperature range −55°C to +85°C is available. An optional environmental screening package per MIL-STD-883 is also available.

PICO 5SMV500

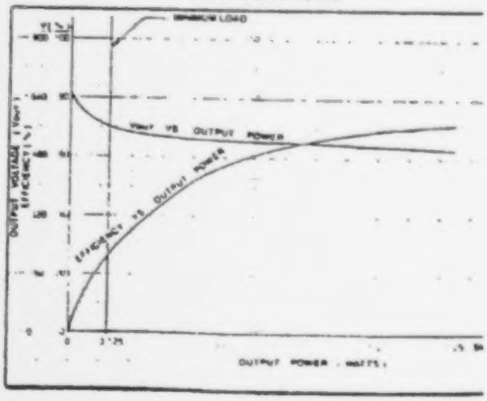

PICO
Electronics, Inc.

453 North Mac Questen Pkwy.
Mt. Vernon, New York 10552

EG&G OPTOELECTRONICS
Canada

DEVELOPMENTAL TYPE - PRELIMINARY DATA SHEET

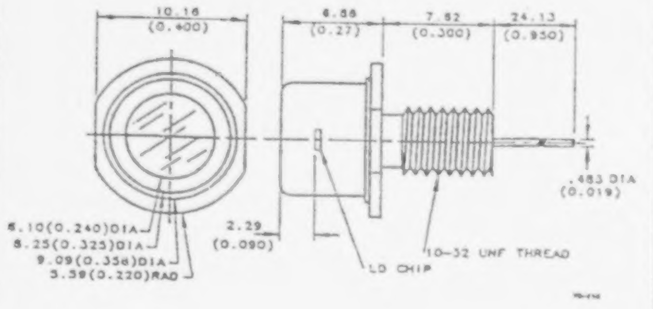
10.16
(0.400)
6.86
(0.27)
7.62
(0.300)
24.13
(0.950)
.483 DIA
(0.019)
6.10(0.240)DIA
8.25(0.325)DIA
9.09(0.358)DIA
5.59(0.220)RAD
2.29
(0.090)
LD CHIP
10-32 UNF THREAD

10-32 Coax Option C86064E

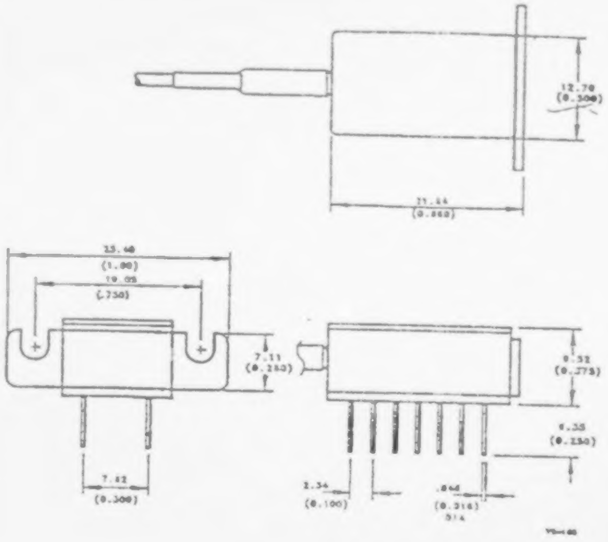
12.70
(0.500)
21.84
(0.860)
25.40
(1.00)
19.05
(.750)
7.11
(0.280)
9.52
(0.375)
6.35
(0.250)
7.62
(0.300)
2.54
(0.100)
.046
(0.018)
DIA

14 pin DIL Option C86063E-1

850 nm - Indium Gallium Arsenide Superluminescent Diode

Characteristics at 25°C							
	C86064E			C86063E-15			
PARAMETERS	MIN	TYP	MAX	MIN	TYP	MAX	UNITS
Output power (P_o)	5	7	-	0.5	0.7	-	mW
Forward current (i_f)	-	60	75	-	60	75	mA
Forward Voltage (Vf)	-	2.2	3.0	-	2.2	3.0	V
Center Wavelength (λm)	840	850	860	840	850	860	nm
Spectral width FWHM (Δλ)	20	30	-	20	30	-	nm
Spectral modulation depth p-p	-	-	5	-	-	5	%
RF monitor current (Im)	-	-	-	-	250	-	µA
RF monitor bias voltage (Vb)	-	-	-	-	-5	-15	V
Fiber optic core/clad. diam.	-	-	-	-	5/125	-	µm
Source size (h x w)	-	1 x 3	-	-	-	-	µm
Thermistor resistance @ 25°C (Rth)	-	-	-	-	10K	-	Ω
Thermistor β	-	-	-	-	3900	-	

EG&G OPTOELECTRONICS
Canada

DEVELOPMENTAL TYPE - PRELIMINARY DATA SHEET

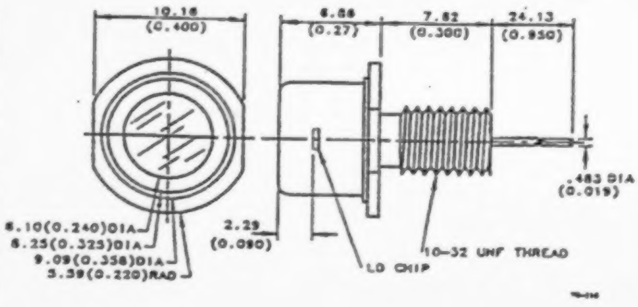
10.16
(0.400)
6.86
(0.27)
7.62
(0.300)
24.13
(0.950)
.483 DIA
(0.019)
6.10(0.240)DIA
8.25(0.325)DIA
9.09(0.358)DIA
5.59(0.220)RAD
2.29
(0.090)
LD CHIP
10-32 UNF THREAD

10-32 Coax Option C86064E

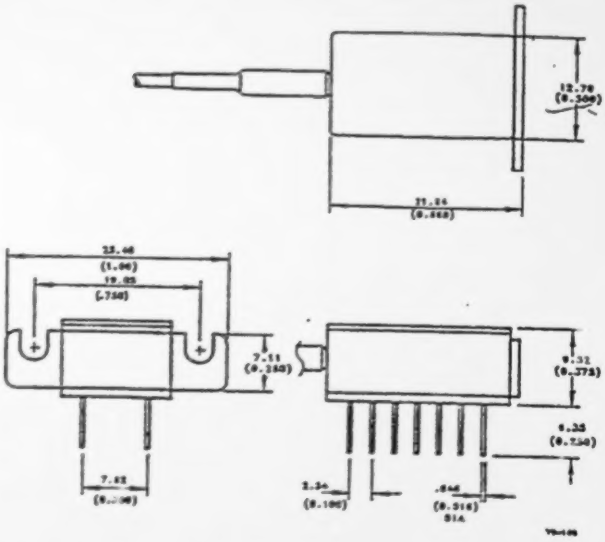
12.70
(0.500)
25.40
(1.00)
19.05
(.750)
7.11
(0.280)
9.52
(0.375)
6.35
(0.250)
7.62
2.54
(0.100)
DIA

14 pin DIL Option C86063E-1

850 nm - Indium Gallium Arsenide Superluminescent Diode

Characteristics at 25°C							
	C86064E			C86063E-15			
PARAMETERS	MIN	TYP	MAX	MIN	TYP	MAX	UNITS
Output power (P_o)	5	7	-	0.5	0.7	-	mW
Forward current (i_f)	-	60	75	-	60	75	mA
Forward Voltage (Vf)	-	2.2	3.0	-	2.2	3.0	V
Center Wavelength (λm)	840	850	860	840	850	860	nm
Spectral width FWHM (Δλ)	20	30	-	20	30	-	nm
Spectral modulation depth p-p	-	-	5	-	-	5	%
RF monitor current (Im)	-	-	-	-	250	-	µA
RF monitor bias voltage (Vb)	-	-	-	-	-5	-15	V
Fiber optic core/clad. diam.	-	-	-	-	5/125	-	µm
Source size (h x w)	-	1 x 3	-	-	-	-	µm
Thermistor resistance @ 25°C (Rth)	-	-	-	-	10K	-	Ω
Thermistor β	-	-	-	-	3900	-	

ATTN: GINO CUGLIETTA, CRC
613-993-7139

PIN-OUT for The C86063E-15

PBF.

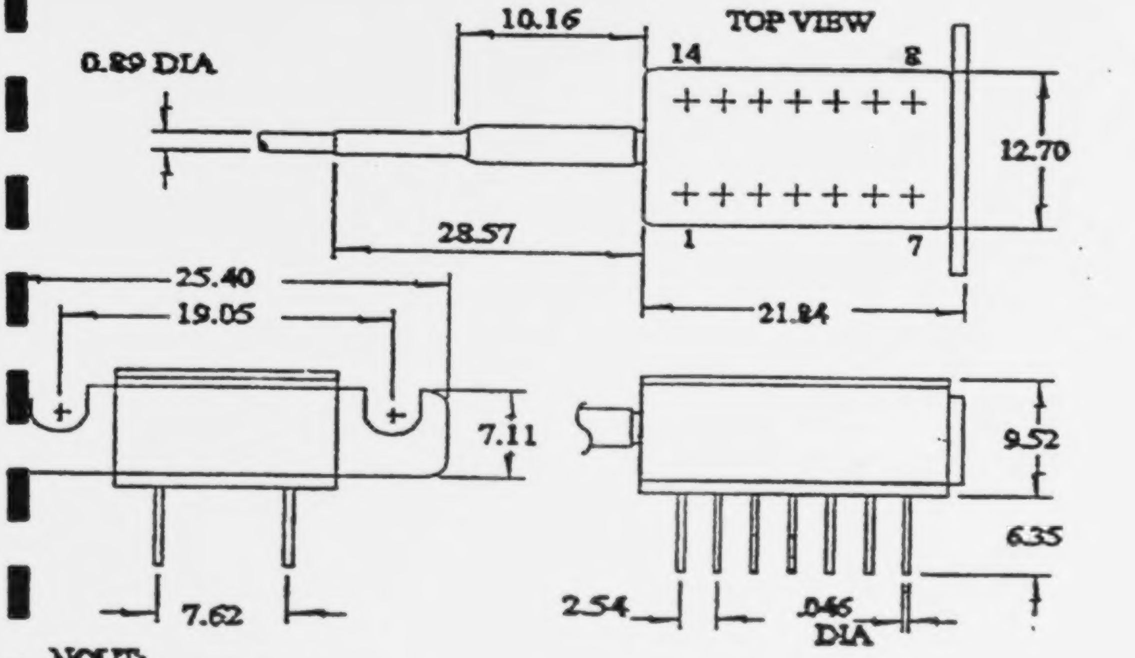
10.16
TOP VIEW
0.89 DIA
14
8
1
7
12.70
28.57
25.40
19.05
21.84
7.11
9.52
6.35
7.62
2.54
.046
DIA

NOUT:
PIN 1: TE COOLER (+)
PIN 2,3,4,6,13: NC
PIN 5: CASE, LASER (+)
PIN 7: MONITOR PD (-)
PIN 8: MONITOR PD (+)
PIN 9: LASER (-)
PIN 10: CASE, LASER (+)
PIN 11,12: THERMISTOR
PIN 14: TE COOLER (-)

VE-16SR1

C86063E-15 14 PIN "Longhorn" Package

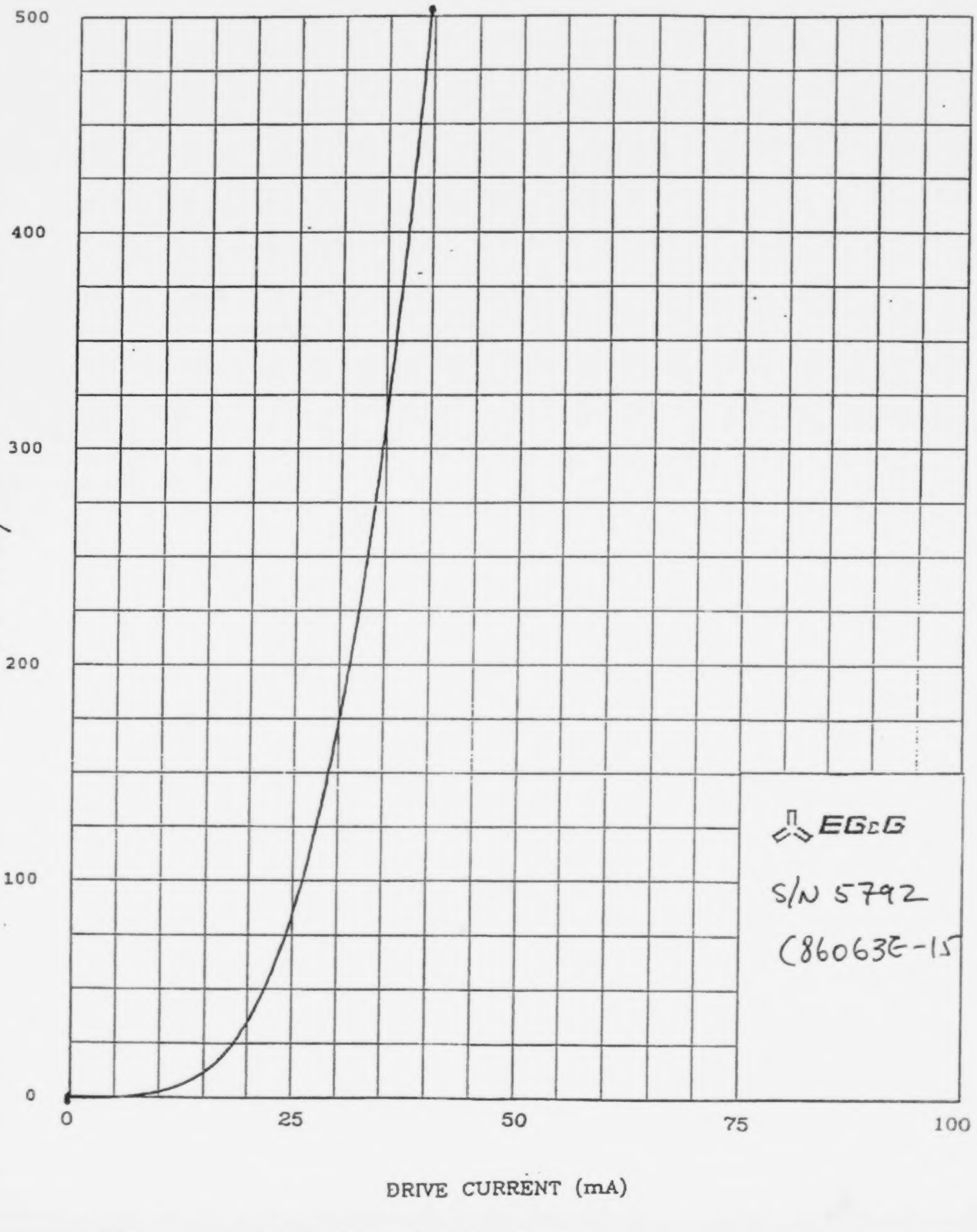
500
400
300
200
100
0
μW
0
25
50
75
100
DRIVE CURRENT (mA)
EG&G
S/N 5792
C86063E-15

10.8 %

C86063E-15 (off spec)

S/N 5792

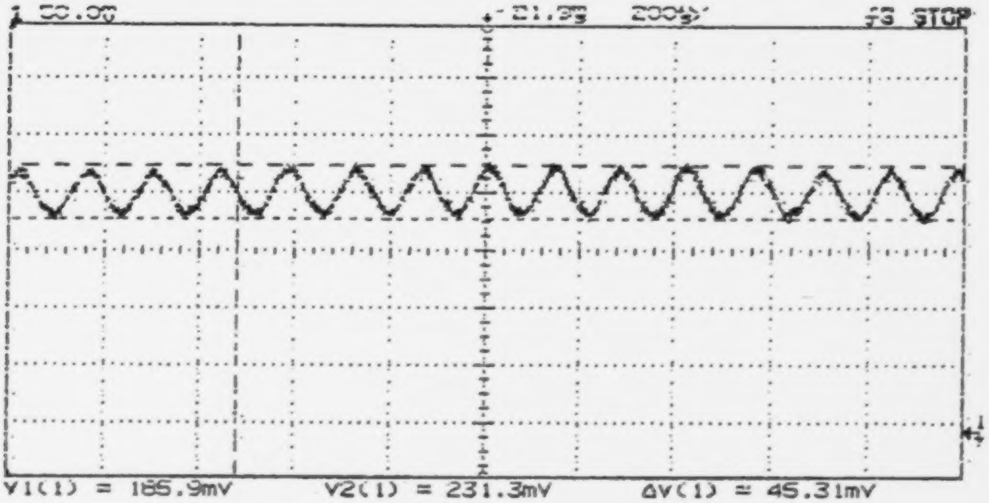

```
V1(1) = 185.9mV        V2(1) = 231.3mV        ΔV(1) = 45.31mV
```

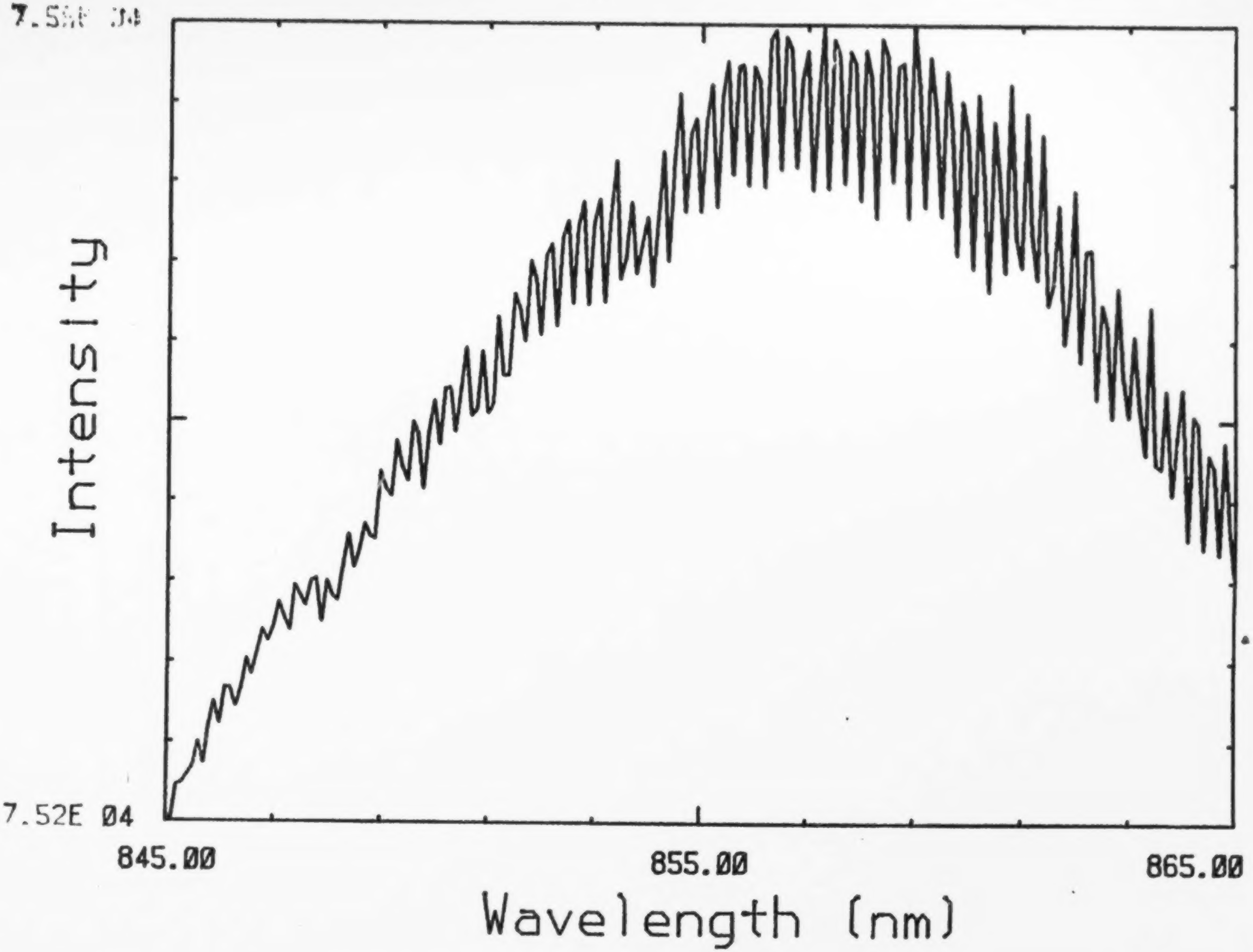
7.58E 04
7.52E 04
Intensity
845.00
855.00
865.00
Wavelength (nm)

RCA

SILICON AVALANCHE PHOTODIODE

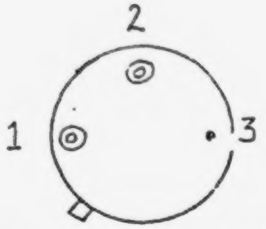

PIN 1 - NEGATIVE
PIN 2 - POSITIVE
PIN 3 - CASE

C30817
C30884
C30895

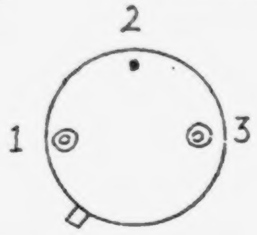

PIN 1 - NEGATIVE
PIN 2 - CASE
PIN 3 - POSITIVE

C30872, C30903E
C30904E, C30905E
C30906E, C30907E
C30908E

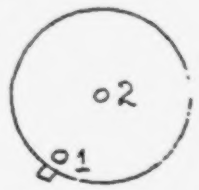

PIN 1 - NEGATIVE
PIN 2 - POSITIVE

C30902E

TYPE: C30908E

SERIAL NO: 0983

* TEST DATA AT 22°C

OPERATING VOLTAGE 196 VOLTS
BREAKDOWN VOLTAGE 202 VOLTS
DARK CURRENT 10 NANO AMPS
RESPONSIVITY 77 AMPS/WATT AT 830 N
NOISE CURRENT $< 2 \times 10^{-13}$ AMPS/HZ$^{\frac{1}{2}}$
RISETIME < .5 NANOSECONDS

* FOR TYPES C30903E THROUGH C30908E THE OPTICAL MEASUREMENTS ARE REFERRED TO RADIATION FALLING ON THE INPUT OF THE LIGHT PIPE.

B Griffin
DATE: 2nd Nov 78

RCA

SILICON AVALANCHE PHOTODIODE

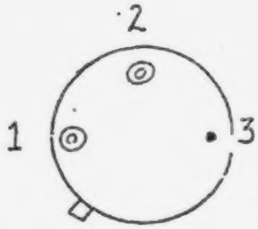

PIN 1 - NEGATIVE
PIN 2 - POSITIVE
PIN 3 - CASE

C30817
C30884
C30895

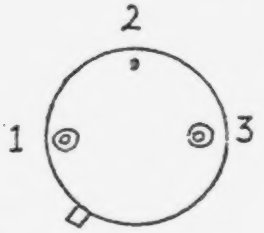

PIN 1 - NEGATIVE
PIN 2 - CASE
PIN 3 - POSITIVE

C30872, C30903E
C30904E, C30905E
C30906E, C30907E
C30908E

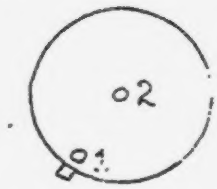

PIN 1 - NEGATIVE
PIN 2 - POSITIVE

C30902E

TYPE: C30908E

SERIAL NO: 0992

* TEST DATA AT 22°C

OPERATING VOLTAGE 207 VOLTS
BREAKDOWN VOLTAGE 213 VOLTS
DARK CURRENT 11 NANO AMPS
RESPONSIVITY 77 AMPS/WATT AT 830 N
NOISE CURRENT $< 2 \times 10^{-13}$ $\text{AMPS/HZ}^{\frac{1}{2}}$
RISETIME < .5 NANOSECONDS

* FOR TYPES C30903E THROUGH C30908E THE OPTICAL MEASUREMENTS ARE REFERRED TO RADIATION FALLING ON THE INPUT OF THE LIGHT PIPE.

DATE: 3rd Nov '78

FIBRE OPTICS DATA PACKAGES

MODULES TYPE C30908E

MEASUREMENT TEMPERATURE = 23°C

UNIT #46

Voltage V	Responsivity A/W	Dark Current nA	NEP $W/\sqrt{Hz}$ at 0.9μ
139	6	10.6	1.6×10^{-14}
178	12	11.7	8.0×10^{-15}
207	30	12.6	3.3×10^{-15}
220	60	12.9	2.1×10^{-15}
224.4	90	13.0	1.9×10^{-15}
227.0	120	13.1	2.1×10^{-15}
236	∞	-	-
UNIT #48			
130	6	10.6	1.4×10^{-14}
165	12	11.6	7×10^{-15}
191	30	12.3	3.3×10^{-15}
202.5	60	12.6	2.5×10^{-15}
206.7	90	12.7	2.5×10^{-15}
209	120	12.8	2.7×10^{-15}
217	∞	-	-

RCA Electro Optics
and Devices

Photodio
Objective D

C3097

Photodiode

Indium Gallium Arsenide Photodiode for Detection of 900 to 1650 nm Radiation

- **High Quantum Efficiency –**
  60% typical at 1300 and 1550 nm
- **Spectral Response Range –**
  900 to 1650 nanometers
- **Extremely Fast Time Response –**
  Rise time typically less than 1.0 ns
  Fall time typically less than 1.0 ns
- **Modified TO-18 Package –**
  With removal cap for fiber coupling

Description

RCA developmental type C30979E is a high speed Indium Gallium Arsenide/Indium Phosphide photodiode. This structure provides high responsivity between 900 and 1650 nanometers and is optimized for detection of 1300 nm and 1550 nm sources. It is particularly useful for fiber optic communications systems at these wavelengths.

The C30979E is supplied with a removable cap permitting optimum coupling of the fiber to the photosensitive surface of the detector. The device is intended for use in advanced prototype fiber optic systems.

Mechanical Characteristics

Photosensitive Surface:	
Shape	Circular
Useful area	0.008 mm^2
Useful diameter	100 μm

Electrical Characteristics at $T_A = 22°$ C

At the DC reverse operating voltage $V_R = 5$ volts.

	Min.	Typ.	Max.	Units
Recommended Operating Voltage	1	5	10	V
Breakdown Voltage, V_{BR}	30	60	–	V
Responsivity:				
At 1300 nm	0.37	0.63	–	A/W
At 1550 nm	0.44	0.75	–	A/W
Quantum Efficiency:				
At 1300 nm	35	60	–	%
At 1550 nm	35	60	–	%
Total Dark Current, I_d	–	40	80	nA
Noise Current, i_n:				
$f = 10$ kHz, $\Delta f = 1.0$ Hz	–	0.3	1.0	pA/Hz$^{1/2}$
Capacitance, C_d	–	1	2	pF
Rise Time, t_r:				
10% to 90% points	–	–	1	ns
Fall Time:				
90% to 10% points	–	–	1	ns

For further information or application assistance on this device, contact your RCA Sales Representative or Photodetector Marketing, RCA, Ste. Anne de Bel
Quebec, Canada H9X 3L3 (514) 457-9000.

This information applies to a contemplated laboratory design and is subject to change. No obligations are assumed as to future manufacture unless otherwise arranged

Information furnished by RCA is believed to be accurate and reliable. However, no responsibility is assumed by RCA for its use; nor for any infringements of patents or other rights of third parties

Registered ® Tradema
Marca(s) Registrac

RCA Electro Optics

Silicon Avalanche Photodiodes
C30902E, C30902S, C30921E, C30921S

DATA SHEET

High Speed Solid State Detectors for Fiber Optic and Very Low Light-Level Applications

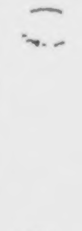
L-571

C30902E
C30902S

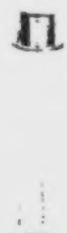
L-933

C30921E
C30921S

RCA Type C30902E avalanche photodiode utilizes a silicon detector chip fabricated with a double-diffused "reach-through" structure. This structure provides high responsivity between 400 and 1000 nanometers as well as extremely fast rise-and falltimes at all wavelengths. Because the fall-time characteristics have no "tail", the responsivity of the device is independent of modulation frequency up to about 800 MHz. The detector chip is hermetically-sealed behind a flat glass window in a modified TO-18 package. The useful diameter of the photosensitive surface is 0.5 mm.

RCA Type C30921E utilizes the same silicon detector chip as the C30902E, but in a package containing a lightpipe which allows efficient coupling of light to the detector from either a focussed spot or an optical fiber up to 0.25 mm in diameter. The internal end of the lightpipe is close enough to the detector surface to allow all of the illumination exiting the lightpipe to fall within the active-area of the detector. The hermetically-sealed TO-18 package allows fibers to be epoxied to the end of the lightpipe to minimize signal losses without fear of endangering detector stability.

The C30902E and C30921E are designed for a wide variety of uses including optical communications at data rates to 1 GBit/second, laser rangefinding, and any other applications requiring high speed and/or high responsivity.

The C30902S and C30921S are selected C30902E and C30921E photodiodes having extremely low noise and low bulk dark-current. They are intended for ultra-low light level applications (optical power less than 1 pW) and can be used in either their normal linear mode ($V_R<V_{BR}$) at gains up to 250 or greater, or as photon counters in the "Geiger" mode ($V_R>V_{BR}$) where a single photoelectron may trigger an avalanche pulse of about 10^8 carriers. In this mode, no amplifiers are necessary and single-photon detection probabilities of up to approximately 50% are possible.

Photon-counting is also advantageous where gating and coincidence techniques are employed for signal retrieval.

- High Quantum Efficiency
  77% Typical at 830 nm
- C30902S and C30921S in Geiger Mode:
  - Single-Photon Detection Probability to 50%
  - Low Dark-Count Rate at 5% Detection Probability – Typically
    15,000/second at +22° C
    350/second at -25° C
  - Count Rates to 2×10^6/second
- Hermetically Sealed Package
- Low Noise at Room Temperature
  - C30902E, C30921E –
    2.3×10^{-13} A/Hz$^{1/2}$
  - C30902S, C30921S –
    1.1×10^{-13} A/Hz$^{1/2}$
- High Responsivity –
  Internal Avalanche Gains in Excess of 150
- Spectral Response Range – (10% Points)
  400 to 1000 nm
- Time Response – Typically 0.5 ns
- Wide Operating Temperature Range –
  -40° C to +70° C

Optical Characteristics

C30902E, C30902S (Figure 13)

Photosensitive Surface:		
Shape	Circular	
Useful area	0.2	mm^2
Useful diameter	0.5	mm
Field of View:		
Approximate full angle for totally illuminated photosensitive surface	100	deg

C30921E, C30921S (Figure 14)

Numerical Aperture of Light Pipe	0.55	
Refractive Index (n) of Core	1.61	
Light Pipe Core Diameter	0.25	mm

Maximum Ratings, Absolute-Maximum Values

Reverse Current at 22° C:		
Average value, continuous operation	200	µA
Peak value (For 1 second duration, non-repetitive	1	mA
Forward Current, I_F at 22°C:		
Average value, continuous operation	5	mA
Peak value (For 1 second duration, non-repetitive)	50	mA
Maximum Total Power Dissipation at 22° C	60	mW
Ambient Temperature —		
Storage, T_{stg}	-60 to + 100	°C
Operating, T_A	-40 to +70	°C
Soldering:		
For 5 seconds	200	°C

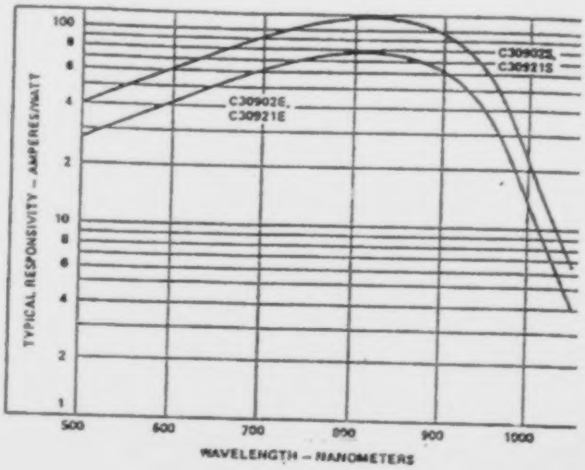

Fig. 1 Typical Spectral Responsivity at 22° C

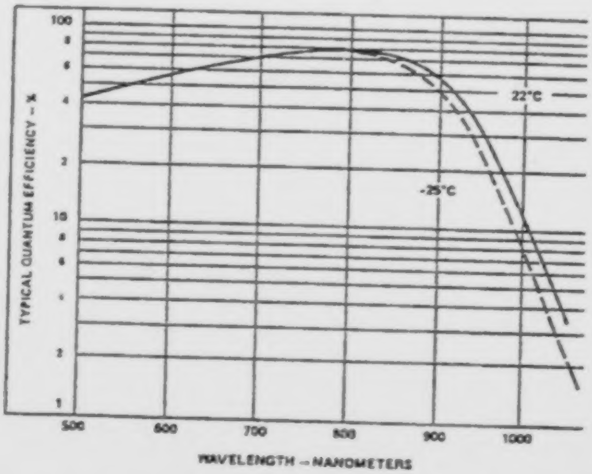

Fig. 2 Typical Quantum Efficiency vs Wavelength

Electrical Characteristics[1] at $T_A = 22°\,C$

	C30902E, C30921E			C30902S, C30921S			
	Min.	Typ.	Max.	Min.	Typ.	Max.	Units
Breakdown voltage, V_{BR}	–	225	–	–	225	–	V
Temperature Coefficient of V_R for Constant Gain	0.5	0.7	0.8	0.5	0.7	0.8	V/°C
Gain	–	150	–	–	250	–	.
Responsivity:							
At 900 nm	55	63	–	92	108	–	A/W
At 830 nm	70	77	–	117	128	–	A/W
Quantum Efficiency:							
At 900 nm	–	60	–	–	60	–	%
At 830 nm	–	77	–	–	77	–	%
Dark Current, I_d	–	1.5×10^{-8} (Figure 6)	3×10^{-8}	–	1×10^{-8} (Figure 6)	3×10^{-8}	A
Noise Current, i_n:[2] $f = 10$ kHz, $\Delta f = 1.0$ Hz	–	2.3×10^{-13} (Figure 3)	5×10^{-13}	–	1.1×10^{-13} (Figure 3)	2×10^{-13}	$A/Hz^{1/2}$
Capacitance, C_d	–	1.6	2	–	1.6	2	pF
Rise Time, t_r: $R_L = 50\ \Omega$, $\lambda = 830$ nm, 10% to 90% points	–	0.5	0.75	–	0.5	0.75	ns
Fall Time: $R_L = 50\ \Omega$, $\lambda = 830$ nm, 90% to 10% points	–	0.5	0.75	–	0.5	0.75	ns
Geiger Mode (See Appendix)							
Dark Count Rate at 5% Photon Detection Probability[3] (830 nm):							
22° C	–	–	–	–	15,000	30,000	cps
-25° C	–	–	–	–	350	700	cps
Voltage Above V_{BR} for 5% Photon Detection Probability[3] (830 nm) (see Figure 8)	–	–	–	–	2	–	V
Dead-Time Per Event (See Appendix)	–	–	–	–	300	–	ns
After-Pulse Ratio at 5% Photon Detection Probability (830 nm) 22° C[4]	–	–	–	–	2	15	%

1 At the DC reverse operating voltage V_R supplied with the device and a light spot diameter of 0.25 mm (C30902E, S) or 0.10 mm (C30921E, S). Note that a specific value of V_R is supplied with each device. When the photodiode is operated at this voltage, the device will meet the electrical characteristic limits shown above. The voltage value will be within the range of 180 to 250 volts.

2 The theoretical expression for shot noise current in an avalanche photodiode is $i_n = (2q\,(I_{ds} + (I_{db}M^2 + P_oRM)\,F)\,B_w)^{1/2}$ where q is the electronic charge, I_{ds} is the dark surface current, I_{db} is the dark bulk current, F is the excess noise factor, M is the gain, P_o is the optical power on the device, and B_w is the noise bandwidth. For these devices $F = 0.98\,(2-1/M) + 0.02\,M$. (Reference: PP Webb, RJ McIntyre, JJ Conradi, "RCA Review", Vol. 35, p. 234, (1974).

3 The C30902S and C30921S can be operated at a substantially higher Dectection Probabilities. See Appendix.

4 After-Pulse occurring 1 microsecond to 60 seconds after main pulse.

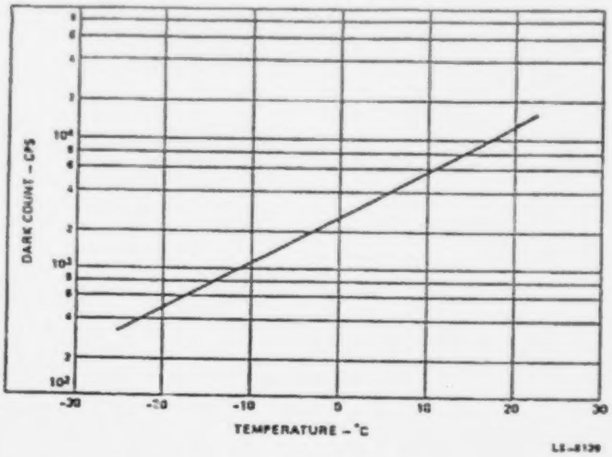

Fig. 11 Typical Dark Count vs Temperature at 5% Photon (830 nm) Detection Efficiency

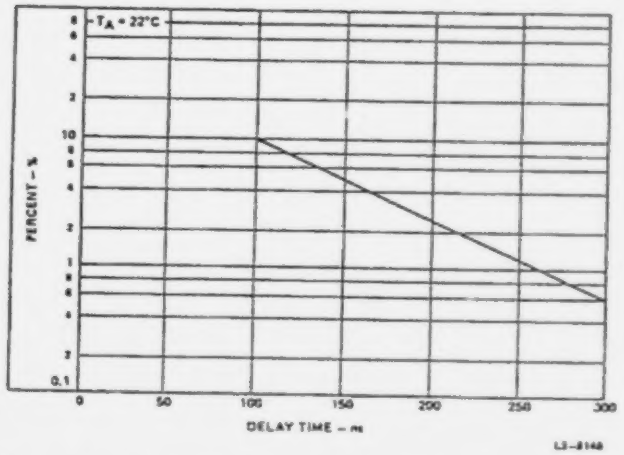

Fig. 12 Chance of an After-Pulse Within the Next 100 ns vs Delay-Time in an Actively Quenched Circuit.
(Typical for C30902S, C30921S at V_{BR} + 25)

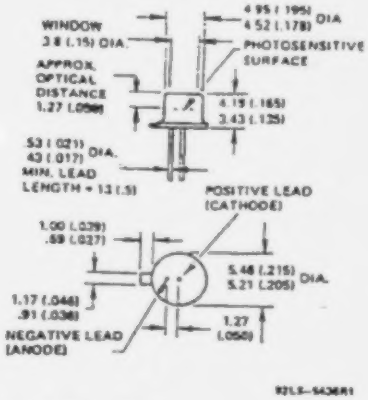
WINDOW
3.8 (.15) DIA.
4.95 (.195)
4.52 (.178) DIA
PHOTOSENSITIVE SURFACE
APPROX. OPTICAL DISTANCE 1.27 (.050)
4.19 (.165)
3.43 (.135)
.53 (.021)
.43 (.017) DIA.
MIN. LEAD LENGTH = 13 (.5)
POSITIVE LEAD (CATHODE)
1.00 (.039)
.69 (.027)
5.46 (.215)
5.21 (.205) DIA.
1.17 (.046)
.91 (.036)
NEGATIVE LEAD (ANODE)
1.27 (.050)
92LS–5436R1

Modified TO-18 Package

Dimensions in millimeters. Dimensions in parentheses are in inches.

Note: Optical distance is defined as the distance from the surface of the silicon chip to the front surface of the window.

Fig. 13 Dimensional Outline - C30902E. C30902S

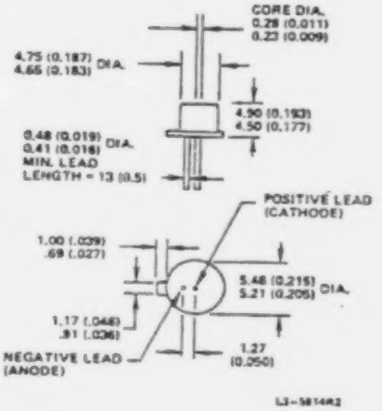
CORE DIA.
0.28 (0.011)
0.23 (0.009)
4.75 (0.187)
4.65 (0.183) DIA.
4.90 (0.193)
4.50 (0.177)
0.48 (0.019)
0.41 (0.016) DIA.
MIN. LEAD LENGTH = 13 (0.5)
POSITIVE LEAD (CATHODE)
1.00 (.039)
.69 (.027)
5.46 (0.215)
5.21 (0.205) DIA.
1.17 (.046)
.91 (.036)
NEGATIVE LEAD (ANODE)
1.27 (0.050)
L3–5814R2

TO-18 Package

Dimensions in millimeters. Dimensions in parentheses are in inches.

Fig. 14 Dimensional Outline - C30921E. C30921S

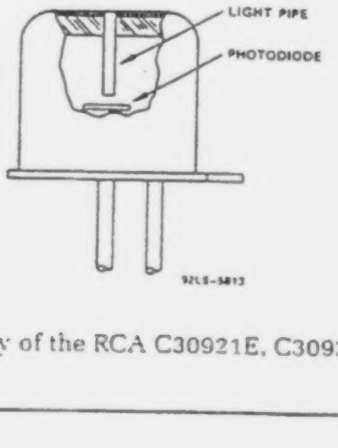
LIGHT PIPE
PHOTODIODE
92LS–5813

Fig. 15 Cutaway of the RCA C30921E. C30921S

EG&G OPTOELECTRONICS

22001 Dumberry Road
Vaudreuil, Quebec
J7V 8P7

Solid State Detectc
Developmental Ty

C30971E, C30971

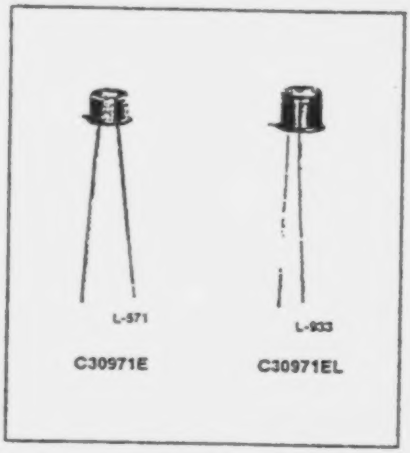

Photodiodes

Silicon Photodetectors for High-Speed, Wide Bandwidth Applications

- Spectral Response Range - (10% Points) - 400 to 1000
- Extremely Fast Time Response -
  Rise time typically 0.5 ns
  Fall time typically 0.5 ns
- Wide Operating Temperature Range - -46° C to +71° C
- Hermetically-Sealed Packages
- Special Package Suitable for Coupling to Fiber Optics

Description

RCA Developmental Types C30971E and C30971EL are high-speed silicon p-i-n photodiodes made with a very thin depletion region. This structure provides a high responsivity between 400 and 1000 nanometers as well as extremely fast rise and fall times at all wavelengths. Because the fall time characteristic has no "tail", the responsivity of the device is independent of modulation frequency up to about 800 MHz.

The C30971E is hermetically sealed behind a flat glass window in a modified TO-18 package. The C30971EL contains a light pipe which is an integral part of the package.

These devices are useful in a wide variety of applications including laser range finding, optical communications, and any application requiring high speed and/or high sensitivity.

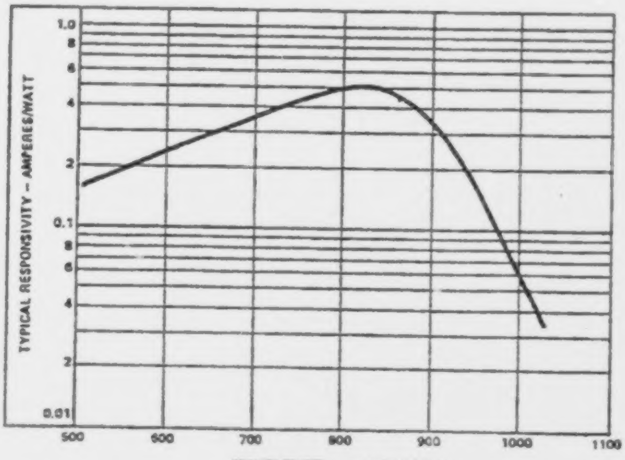

Figure 1 - Typical Spectral Responsivity

Characteristics

Maximum Ratings, Absolute-Maximum Values

Reverse Bias Dark Current	100	µA
Photocurrent Density, J_P, at 22° C:		
Average value, continuous operation	5	mA/mm²
Peak value (For 1 second duration, non-repetitive)	20	mA/mm²
Forward Current, I_F, at 22° C:		
Average value, continuous operation	5	mA
Peak value (For 1 second duration, non-repetitive)	50	mA
Maximum Total Power Dissipation at 22° C	0.1	W
Ambient Temperature:		
Storage, T_{stg}	-60 to +100	°C
Operating, T_A	-46 to +71	°C
Soldering:		
For 5 seconds	200	°C

C30971E

Photosensitive Surface:		
Shape	Circular	
Useful area	0.2	mm²
Useful diameter	0.5	mm
Field of View:[1]		
Full angle (α) for totally illuminated photosensitive surface	100	deg
Full angle (α') for partially illuminated photosensitive surface	114	deg

C30971EL

Numerical Aperture of Light Pipe	0.55	
Refractive Index (η) of Core	1.62	
Light Pipe Core Diameter	0.25	mm

For further information or application assistance on these devices, contact your RCA Sales Representative or Photodetector Marketing, RCA, Ste. Anne de Bellevue, Quebec, Canada H9X 3L3 (514) 457-9000.

Developmental-type devices or materials are intended for engineering evaluation. The type designation and data are subject to change, unless otherwise arranged. No obligation

Information furnished by RCA is believed to be accurate and reliable. However, no responsibility is assumed by RCA for its use

Trademark(s) ® Registere

Electrical Characteristics at $T_A = 22° C$[2]

	Min.	Typ.	Max.	Units
Breakdown Voltage, V_{BR}	200	-	-	V
Operating Voltage, V_{OP}	-	100	-	V
Responsivity:				
C30971E -				
At 900 nm	0.40	0.45	-	A/W
At 830 nm	0.45	0.50	-	A/W
C30971EL -				
At 900 nm	0.25	0.35	-	A/W
At 830 nm	0.30	0.40	-	A/W
Dark Current, I_d	-	1×10^{-8}	3×10^{-8}	A
Noise Current, i_n: $f = 10$ kHz, $\Delta f = 1.0$ Hz	-	6×10^{-14}	1.5×10^{-13}	$A/Hz^{1/2}$
Capacitance, C_d	-	1.6	2	pF
Rise Time, t_r: $R_L = 50\ \Omega$, $\lambda = 900$ nm, 10% to 90% points	-	0.5	0.75	ns
Fall Time: $R_L = 50\ \Omega$, $\lambda = 900$ nm, 90% to 10% points	-	0.5	0.75	ns

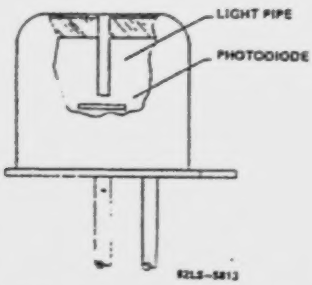
LIGHT PIPE
PHOTODIODE
92LS-5813

Figure 2 - Cutaway of the RCA C30971EL

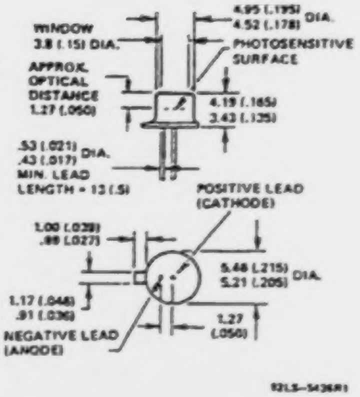
WINDOW
3.8 (.15) DIA.
4.95 (.195)
4.52 (.178) DIA.
PHOTOSENSITIVE SURFACE
APPROX. OPTICAL DISTANCE 1.27 (.050)
4.19 (.165)
3.43 (.135)
.53 (.021)
.43 (.017) DIA.
MIN. LEAD LENGTH = 13 (.5)
POSITIVE LEAD (CATHODE)
1.00 (.039)
.69 (.027)
5.46 (.215)
5.21 (.205) DIA.
1.17 (.046)
.91 (.036)
NEGATIVE LEAD (ANODE)
1.27 (.050)
92LS-5436R1

Modified TO-18 Package

Dimensions in millimeters. Dimensions in parentheses are in inches.

Note: Optical distance is defined as the distance from the surface of the silicon chip to the front surface of the window.

Figure 3 - Dimensional Outline - C30971E

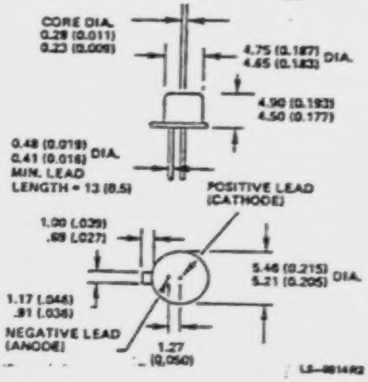
CORE DIA.
0.28 (0.011)
0.23 (0.009)
4.75 (0.187)
4.65 (0.183) DIA.
4.90 (0.193)
4.50 (0.177)
0.48 (0.019)
0.41 (0.016) DIA.
MIN. LEAD LENGTH = 13 (0.5)
POSITIVE LEAD (CATHODE)
1.00 (.039)
.69 (.027)
5.46 (0.215)
5.21 (0.205) DIA.
1.17 (.046)
.91 (.036)
NEGATIVE LEAD (ANODE)
1.27 (0.050)

TO-18 Package

Dimensions in millimeters. Dimensions in parentheses are in inches.

Figure 4 - Dimensional Outline - C30971EL

Warning - Personal Safety Hazards
Electrical Shock - Operating voltages applied to this device present a shock hazard.

---

[1] The values specified for field of view are approximate and are critically dependent on the dimensional tolerances of the package component parts.

[2] The C30971EL characteristics are referred to the input surface of the light pipe.

EG&G
OPTOELECTRONICS

Silicon Photodiodes
C30656 Series

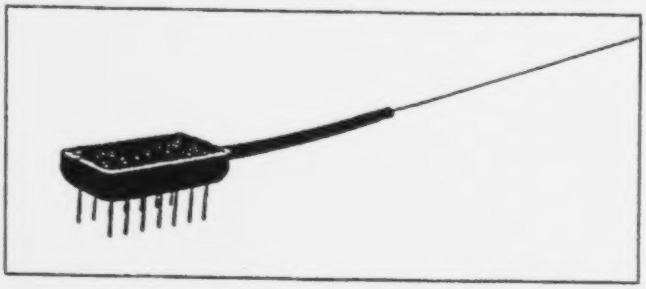

Transimpedance Preamplifier Modules With Soldered Fiber Optic Pigtails for Detection of 400 to 1000 nm Radiation

- **System Bandwidth (3 dB Point)**
  10 MHz (C30656-010) to
  350 MHz (C30656-350)
- **Responsivity at $T_A = 22^\circ C$**
  165KV/W (C30656-010) to
  5KV/W (C30656-350)
- **Spectral Response Range**
  400 to 1000 nm
- **Sensitivity at 10^{-9} B.E.R.**
  -49 dBm (C30656-010) to
  -31 dBm (C30656-350)
- **System Noise Equivalent Power (NEP) at $T_A = 22^\circ C$**
  $6 \times 10^{-13} W/Hz^{1/2}$ (C30656-010) to
  $7 \times 10^{-12} W/Hz^{1/2}$ (C30656-350)
- **Hermetically-Sealed 14-Pin Dual In-Line Packages**

The C30656 Series are Silicon (p-i-n) photodiodes with hybrid preamplifiers supplied in hermetically-sealed 14-pin dual in-line packages. They are available with soldered fiber optic pigtails which provide optimum optical coupling to the photodiode and constant responsivity through the full temperature range.

The p-i-n photodiode (C30971) used in these devices is a high-speed silicon p-i-n photodiode made with a very thin depletion region. This structure provides a high responsivity between 400 and 1000 nanometers as well as extremely fast rise and fall times at all wavelengths. The preamplifier is a transimpedance type employing a low noise GaAs FET front-end and a cascode feedback circuit. An emitter follower-stage is added to the output to provide improved output coupling efficiency and isolation.

Modules are available having bandwidths ranging from 10 MHz to 350 MHz; they are designated C30656-XXXQC-YY. The suffix -YY denotes the fiber type (see Table 1). When ordering, the customer should specify the required bandwidth and preferred fiber. For example, C30997-090QC-02 is a device with a bandwidth of 90 MHz and a 50 µm core fiber with a 900 µm outer diameter (refer to Table 1 for fiber nomenclature).

To obtain wideband characteristics, the output of these devices should be AC (Capacitively) coupled to terminations equal to or greater than 500 ohms.

Absolute-Maximum Ratings, Limiting Values[1]

Photodiode Bias Voltage, V_R:	
At $T_A = 22^\circ C$	-200 V
Preamplifier Voltage:	
Positive, $+V_{CC}$	+6.3 V
Negative, $-V_{CC}$	-6.3 V
Incident Radiant Flux, Φ_M ($T_A = 22^\circ C$)	
Average Value	1 mW
Peak value (1 second duration, non-repetitive)	4 mW
Ambient Temperature:	
Storage, T_{stg}	-50 to +100 °C
Operating, T_A	-40 to + 70 °C

---

[1] These are limiting values of operating and environmental conditions. Exceeding these values can cause damage to the device.

C30656-010QC-02

Electrical Characteristics

At an ambient temperature (T_A) of 22°C, negative photodiode bias of -100 VDC, preamplifier operating voltages of +5.0 VDC and -5.2 VDC, and the signal output AC (capacitively) coupled into a 500 ohm termination.

Performance of 10, 30 and 90 MHz devices are tabulated. These devices are also available at other bandwidths on request; refer to Figures 2 through 5 for performance of specific types at 22°C and 820 nm.

	C30656-010QC-YY			C30656-030QC-YY			C30656-090QC-YY			
	MIN	TYP	MAX	MIN	TYP	MAX	MIN	TYP	MAX	UNITS
Responsivity:										
At 820 nm	130	165	-	70	90	-	15	18	-	KV/W
At 900 nm	105	130	-	60	75	-	10	14	-	KV/W
Noise Equivalent Power (NEP): 100kHz<f<f_o										
At 820 nm	-	0.6	1.1	-	0.8	1.7	-	2.2	4.0	pW/Hz$^{1/2}$
At 900 nm	-	0.7	1.4	-	1.1	2.0	-	2.9	6.0	pW/Hz$^{1/2}$
Output Spectral Noise Voltage Density: 100kHz<f<fo	-	100	150	-	80	120	-	40	60	nV/Hz$^{1/2}$
Output Impedance	-	20	40	-	20	40	-	20	40	Ω
Bandwidth, f_o (3 dB point)	7	10	-	24	30	-	70	90	-	MHz
Rise Time, t_r: 10% to 90% points	-	35	50	-	12	15	-	4	5	ns
Fall Time, t_f: 90% to 10% points	-	35	50	-	12	15	-	4	5	ns
Dynamic Range	21	24	-	21	24	-	21	24	-	dB
Output Offset Voltage	-0.7	-1.5	-3.0	-0.7	-1.5	-3.0	-0.7	-1.5	-3.0	V
Supply Current:										
+5.0V	-	25	35	-	25	35	-	25	35	mA
-5.2V	-	7	15	-	7	15	-	8	15	mA
Projected Sensitivity at 10^{-9} B.E.R. NRZ, avg. power, Data Rate = 1.4 x Bandwidth at 820 nm	-47	-49	-	-44	-46	-	-37	-39	-	dBm

Electrical Characteristics Continued

At an ambient temperature (T_A) of 22°C, negative photodiode bias of ~ -100 VDC, preamplifier operating voltages of +5.0 VDC and -5.2 VDC, and the signal output AC (capacitively) coupled into a 500 ohm termination.

Performance of 250 and 350 MHz devices are tabulated. These devices are also available at other bandwidths on request; refe to Figures 2 through 5 for performance of specific types at 22°C and 820 nm.

	C30656-250QC-YY			C30656-350QC-YY			
	MIN	TYP	MAX	MIN	TYP	MAX	UNITS
Responsivity:							
At 820 nm	4.0	5.0	-	2.0	2.8	-	KV/W
At 900 nm	3.2	4.0	-	1.5	2.2	-	KV/W
Noise Equivalent Power (NEP): 100 kHz<f<f_o							
At 820 nm	-	6.0	11.0	-	7.1	15.0	pW/$Hz^{1/2}$
At 900 nm	-	7.5	14.0	-	9.0	20.0	pW/$Hz^{1/2}$
Output Spectral Noise Voltage Density: 100 kHz<f<fo	-	30	45	-	20	30	nV/$Hz^{1/2}$
Output Impedance	-	20	40	-	20	40	Ω
Bandwidth, f_o (3 dB point)	200	250	-	280	350	-	MHz
Rise Time, t_r: 10% to 90%	-	1.5	2	-	1.0	1.3	ns
Fall Time, t_f: 90% to 10%	-	1.5	2	-	1.0	1.3	ns
Dynamic Range	21	24	-	21	24	-	dB
Output Offset Voltage	-0.7	-1.5	-3.0	-0.7	-1.5	-3.0	V
Supply Current:							
+5.0V	-	25	35	-	25	35	mA
-5.2V	-	8	15	-	8	15	mA
Projected Sensitivity at 10^{-9} B.E.R. NRZ, avg. power, Data Rate = 1.4 x Bandwidth at 820 nm	-31	-33	-	-29	-31	-	dBm

Table 1. **Standard Fiber pigtail options. Standard length is one meter.**

-YY	FIBER TYPE	DIAMETERS µm			NUMERICAL APERTURE
		CORE	CLADDING	OUTER	
-01	MULTIMODE	50	125	500	0.2
-02	MULTIMODE	50	125	900	0.2
-03*	MULTIMODE	85	125	900	0.26
-04*	MULTIMODE	62.5	125	900	0.29
-05*	MULTIMODE	100	140	900	0.29
-06*	MULTIMODE	200	240	900	0.24
-07*	SINGLEMODE	9	125	900	0.1

*These pigtail options are available on a special order basis.

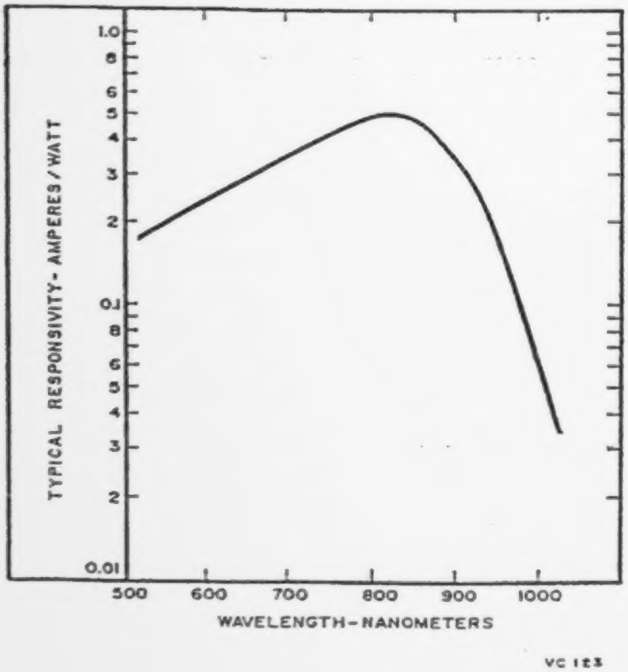

Figure 1 Typical Spectral Responsivity

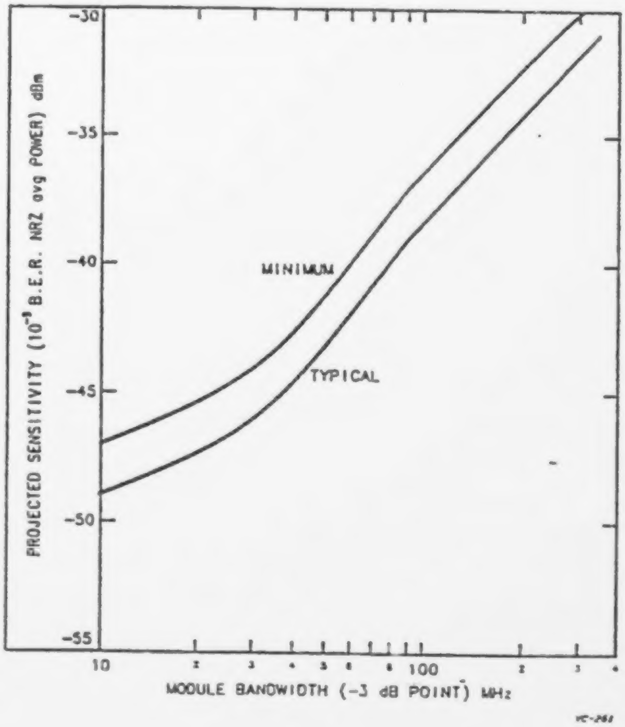

Figure 2 Bandwidth vs Projected Sensitivity

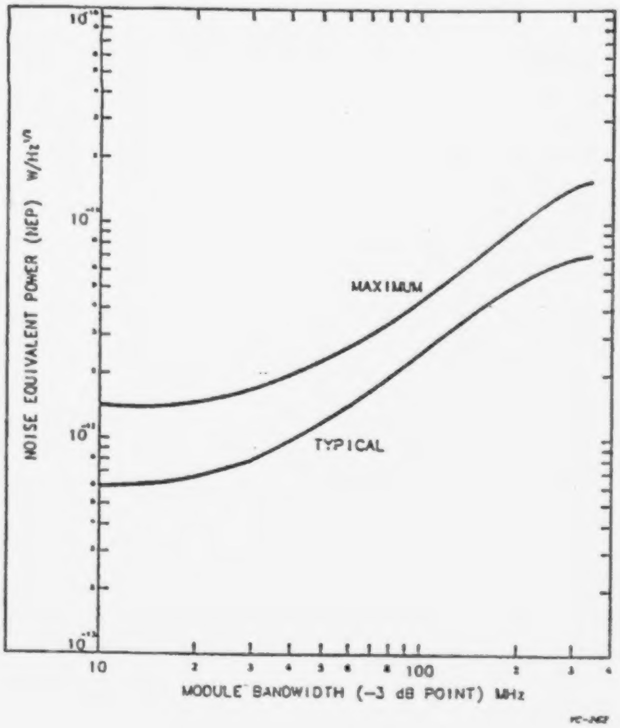

Figure 3 Bandwidth vs NEP

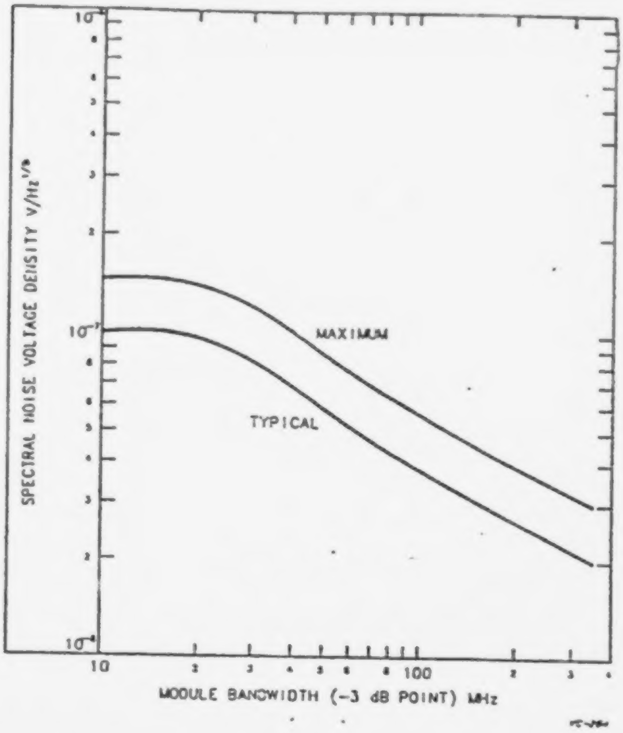

Figure 5 Bandwidth vs Noise Density

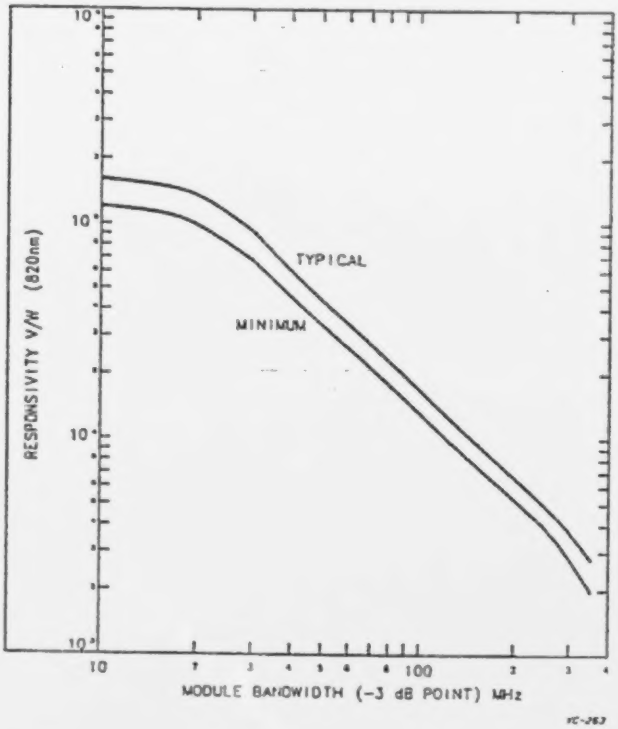

Figure 4 Bandwidth vs Responsivity

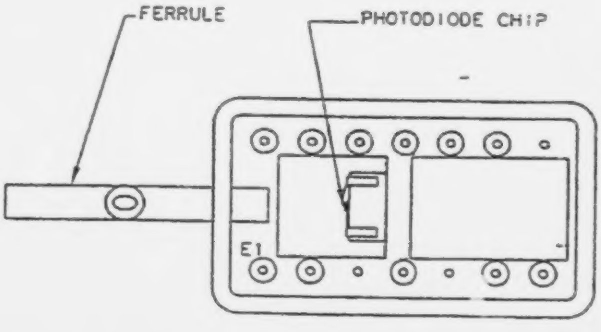
FERRULE
PHOTODIODE CHIP
E1
YS-191

Figure 6 Package With Cover Removed

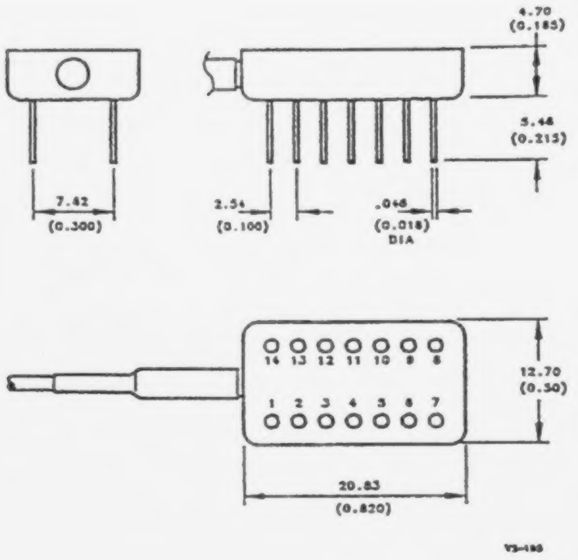

Figure 7 Dimensional Outline - C30656-XXXQC-YY

1: Negative Bias for Photodiode

2, 6, 11, 12, 13, 14: No Connection, Do Not Use

3, 5, 8: Ground (Case and Power Supply)

4: $-V_{cc}$ Negative Bias for Amplifier

7: Signal Output

10: $+V_{cc}$ Positive Bias for Amplifier

Dimensions in millimeters. Dimensions in parenthesis are in inches.

For further information please contact your local EG&G Optoelectronics representative or EG&G Canada Ltd., Optoelectronics Division, 22001 Dumberry Road, Vaudreuil, Quebec J7V 8P7 Canada

Tel: (514) 424-3300 Fax: (514) 424-3411

Consistent with EG&G Canada Ltd.'s policy of continually updating and improving its products, the type designation and data are subject to change, unless otherwise arranged. No obligations are assumed for notice of change of future manufacture of these devices or materials.

Trademark(s)® Registered Marca(s) Registrada(s). Information furnished by EG&G Canada Ltd., Optoelectronics Division is believed to be accurate and reliable. However, no responsibility is assumed by EG&G Canada Ltd., Optoelectronics Division for its use; nor for any infringements of patents or other rights of third parties which may result from its use. No license is granted by implication or otherwise under any patent or patent rights of EG&G Canada Ltd. or its affiliates.

EG&G OPTOELECTRONICS CANADA

TRANSIMPEDANCE PREAMPLIFIER MODULES C30656-010QC-02

ELECTRICAL CHARACTERISTICS	C30656-010			SERIAL A1289
	Min.	Typ.	Max.	Measured
Responsivity at 820 nm	130	165	-	163 KV/W
Noise Equivalent Power (NEP)	-	0.6	1.1	0.45 pW/√H
Output Spectral Noise Voltage Density	-	100	150	73 nV/√H
Bandwidth	7	10	-	8.9 MHz
Sensitivity @ 10^{-9} B.E.R.	-47	-49	-	-50.5 dBm
Output Offset Voltage	-0.7	-1.5	-3.0	-1.16 Volts
Supply current				
+5.0 Volts	-	25	35	25.0 mA
-5.2 Volts	-	7	15	6.7 mA

Tested at an Ambient Temperature of 22°C, and the Signal Output AC (capacitively) Coupled into a 500 Ω Termination.

Electrical Test Performed by: 8 November 1

Pin Connections

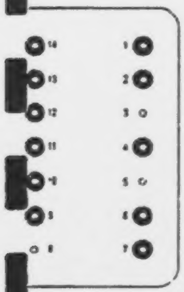

Bottom View

1: Negative Bias for Photodiode (-100 Volts)
2,6,9,11,12,13,14: No Connection, Do Not Use
3,5,8: Ground(Case and Power Supply)
4: -Vcc Negative Bias for Amplifier
7: Signal Output
10: +Vcc Positive Bias for Amplifier

EG&G
OPTOELECTRONICS
Canada

September 26, 1994

TOTAL 2 PAGES

TO: Sylvain Theriault
Industry Canada
Tel: 613-990-9721
Fax: 613-993-7139

FAXED

From: Bernicy Fong
Tel: 514-424-3349
Fax: 514-424-3411

SUBJECT: QUOTATION

Following your request for pricing dated Sept. 22, EG&G Optoelectronics Canada is pleased to submit the following:

DEVICE TYPE	QUANTITY	UNIT PRICE, $Cdn	EST. DELIVERY
C86130E-15	1-9 PCS	$5681.00	6-8 WKS ARO
C86063E-15	"	$3836.00	"
C86064E	"	$688.00	"
C30971EQC-02	1-24 PCS	$139.00	4-6 WKS ARO
C30670EQC-02	"	$221.00	"
C30656-XXXQC*	2-24 PCS**	$750.00	8-10 WKS ARO
C30656-YYYQC*	"	$1288.00	"
C30902EQC-C2	1-24 PCS	$216.00	4-6 WKS ARO
C30902SQC-02	"	$488.00	"
C30657-XXXQC*	2-24 PCS**	$965.00	8-10 WKS ARO
C30657-YYYQC*	"	$1288.00	"

C30657-010QC-02

* XXXQC = bandwidth of ≤ 250 MHz.
YYYQC = bandwidth of > 250 Mhz.

** The minimum order quantity for these parts is 2 pieces.

22001 Dumberry • Vaudreuil • (Québec) J7V 8P7 • (514) 424-3300 Fax: (514) 424-3411

Fuse sensors

Sensors: 1.0
Length: ~~0.5~~ mm 15, 17, 19, 20, 21, 22, 23, 24 ~826.1nm
R: ~ 70% (8X) 16, 18 ~826.4nm

Laser stabilizers:
Length: 10 mm
R: ~ 75% (2X) 25, 26
R: ~ 55% (2X) 27, 28
R: ~ 35% (2X) 29, 30